ACS APPLIED NANO MATERIALS

www.acsanm.org Review

Plasmonic Nanostars: Systematic Review of their Synthesis and Applications

Nhat M. Ngo, Hung-Vu Tran, and T. Randall Lee*

Cite This: *ACS Appl. Nano Mater.* 2022, 5, 14051−14091 Read Online

ACCESS | Metrics & More | Article Recommendations

ABSTRACT: The emergence of plasmonic nanostars with their attractive properties and unique versatility has enabled a wide range of advanced technologies critical to human health, safety, energy, and environmental remediation with vast potential for further exploration. In addition to their superior surface-to-volume ratios compared to those of other plasmonic nanostructures, plasmonic nanostars arguably possess the largest numbers of hotspots with intensely amplified electric fields when they are subjected to suitable electromagnetic waves to trigger localized surface plasmon resonance (LSPR). These outstanding characteristics make plasmonic nanostars ideal for many applications that benefit from the plasmonic enhancement effect of LSPR and/or the large surface area. Over the past decade, an increasing number of research endeavors has been reported on the synthesis and application of plasmonic nanostars to advance the state-of-the-art for various existing technologies. These contributions are pertinent to real-time image-guided multifunctional anticancer theranostics, the ultrasensitive on-site detection of the devastating virus SARS-CoV-2, multimodal multiplexed brain imaging, greatly enhanced catalysts for energy and environmental processes, or more efficient and stable solar cells. In addition to the enhancement of important but familiar technologies, plasmonic nanostars have also been employed to push the technological frontiers in multiple fields to enable applications such as maskless write-on lithography, nanosized field electron emitters, coherent random lasers, neural activity modulation, and optically controlled electrical currents. Despite great performance in various fields since their introduction, the nascency of this unique class of plasmonic nanostructures and the rise of unique types of plasmonic nanostars, in addition to the dominance of gold nanostars in recent years, indicate that there are still many opportunities for study, exploration, and development. This Review outlines a comprehensive picture of the current state of plasmonic nanostar research with a focus on their technological and scientific applications. We hope this Review will enlighten future collective endeavors to develop more effective plasmonic nanostars and incorporate them into mainstream technologies so that these stars can truly shine.

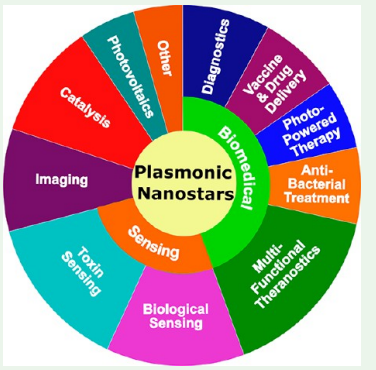

KEYWORDS: *plasmonic, nanostars, gold, silver, nanoparticles, SERS, biomedical, photovoltaics, catalysis, LSPR, energy*

Downloaded via UNIV OF HOUSTON MAIN on October 28, 2022 at 16:43:03 (UTC).
See https://pubs.acs.org/sharingguidelines for options on how to legitimately share published articles.

1. INTRODUCTION

The interaction of light and matter plays crucial roles in human life and activities, ranging from our cherished eyesight to the ubiquitous utilization of lasers in modern life to the sophisticated spectrometers utilized for space exploration. The accelerating development of nanotechnology in recent decades has brought attention to many exotic and useful properties of materials that are not observed in their bulk counterparts.[1] Among various classes of nanomaterials, plasmonic nanostructures, usually involving noble metals, have demonstrated better performances with superior chemical and physical properties compared to their bulk counterparts.[2] In addition to the characteristically high surface-to-volume ratio inherent to all nanosized materials, plasmonic nanostructures also exhibit many properties unique to only this class of nanostructures.[3] Specifically, when plasmonic nanostructures have dimensions comparable to or smaller than the wavelength of incident light of the electromagnetic field with which they are interacting, they exhibit a unique phenomenon called localized surface plasmon resonance (LSPR).[3] LSPR occurs when conduction-band electrons in metallic nanostructures oscillate together with an irradiating incident electromagnetic field, as illustrated in Figure 1a. Consequently, when the frequency of the incident field matches the resonance frequency of the metal nanostructures, peak absorption appears at that resonant frequency (Figure 1b).

In addition to the elemental compositions and the dielectric environments surrounding them, the LSPR frequencies of plasmonic nanostructures vary with their size and shape (Figure 1b). Thus, many plasmonic nanostructures with different

Received: June 9, 2022
Accepted: August 16, 2022
Published: September 23, 2022

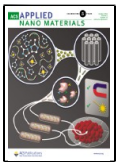

© 2022 The Authors. Published by American Chemical Society

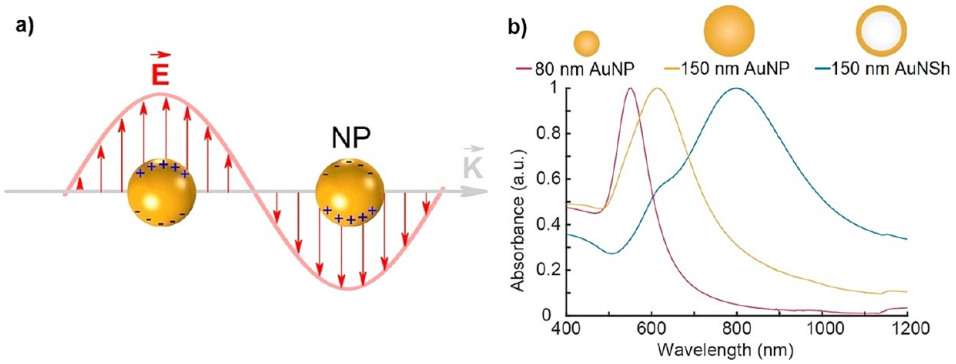

Figure 1. (a) Schematic illustration of the interaction between conduction-band electrons in a metallic nanostructure and the incident electromagnetic field *E*. (b) Sketch of the plasmonic nanoparticles and their absorption spectra in water. NP: nanoparticle, AuNP: gold nanoparticle, AuNSh: gold nanoshell. Adapted with permission from refs 2 and 4. Copyright 2019 American Chemical Society and 2016 Spring Nature.

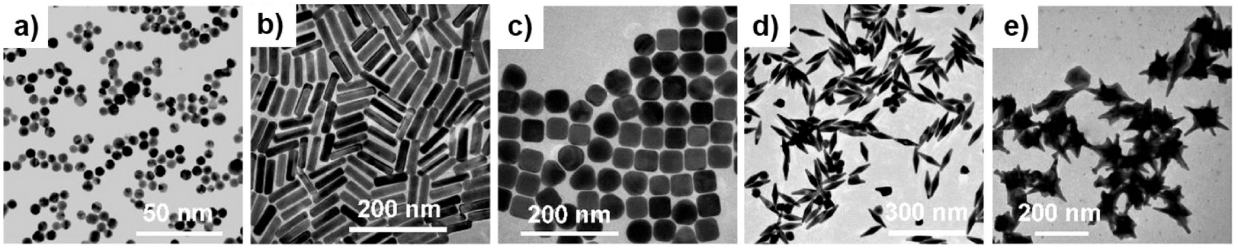

Figure 2. Representative transmission electron microscopy images of plasmonic AuNPs: (a) nanospheres, (b) nanorods, (c) nanocubes, (d) nanobipyramids, and (e) nanostars. Adapted with permission from ref 11. Copyright 2008 American Chemical Society.

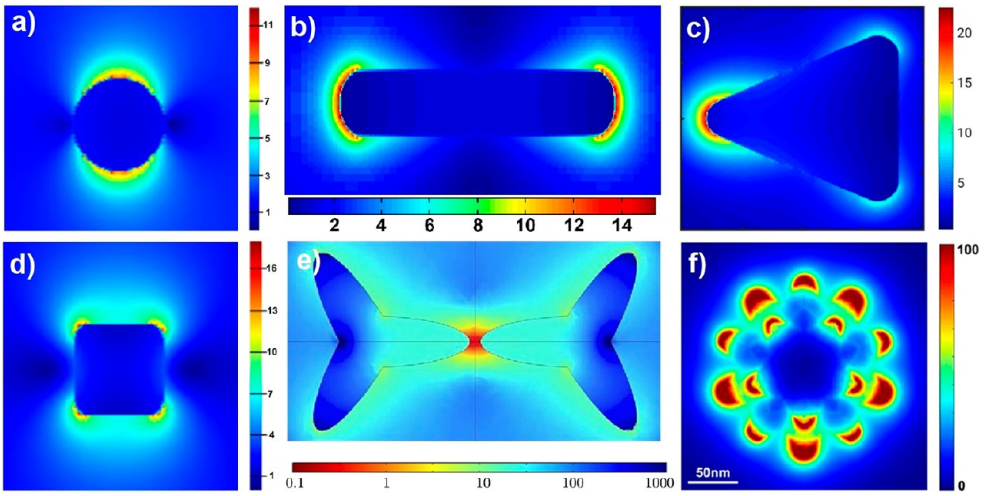

Figure 3. Simulated electric field distributions of (a) nanospheres,[26] (b) nanorods,[16] (c) nanotriangles,[17] (d) nanocubes,[26] (e) nanotripods,[18] and (f) nanostars[27] when interacting with light. Reproduced and adapted with permission from refs 16−18, 26, and 27. Copyright 2021 American Chemical Society (ref 27, part f).

morphologies (Figure 2) and unique electronic, optical, and chemical properties have been synthesized and studied. Exploiting their LSPR characteristics, various applications spanning a wide range of technological fields have been explored, developed, and implemented based on plasmonic nanostructures, including photothermal treatment,[2] targeted drug delivery,[5] precision sensing,[6] enhanced imaging,[7] catalysis,[8,9] and photovoltaics.[10]

Noble metal nanostars are one of the most recently developed types of plasmonic nanostructures and have drawn significant attention from many different research communities. The remarkable interest in plasmonic nanostars mostly originates from their superior specific surface areas and dominant numbers of plasmonic hotspots compared to those of other plasmonic nanostructures,[12,13] as illustrated in Figure 3. Combined with the opening of more crystal facets for surface modification as well as complex combinations, larger surface area-to-volume ratios make plasmonic nanostars much more promising for applications that would benefit from extended contact surfaces, such as sensing and catalysis.[14,15] Furthermore, plasmonic nanostars possess isotropic plasmonic properties owing to the highly omnidirectional orientation of their arms. This plasmonic isotropy lends versatility to the nanostars when compared to other plasmonic structures such as nanorods,[16] nanotriangles,[17] and nanotripods.[18] Moreover, a greatly intensified electric field[19] with high numbers of plasmonic hotspots (Figure 3f) is

https://doi.org/10.1021/acsanm.2c02533
ACS Appl. Nano Mater. 2022, 5, 14051−14091

Table 1. Synthesis Methodologies for Plasmonic Nanostars[a]

entry	nanostar type	method	surfactant/directing agent	conditions	size range (nm)	ref
1	AuNSt	one-pot		RT	50−150	29
2	AuNSt	seed-mediated	PVP	100 °C, RT	45−116	30
3	AuNSt	seed-mediated, silver-assisted	Triton-X-100	RT	100−160	31
4	AuNSt	seed-mediated, silver-assisted	CTAB	100 °C, RT	200−400	32
5	AuNSt	one-pot, silver-assisted	Triton-X-100	RT	100−300	33
6	AuNSt	one-pot, silver-assisted	SDS, AOT, BDAC	RT	74−196	34
7	AuNSt	one-pot, silver-assisted		RT	100−250	35
8	AgNSt	seed-mediated		RT	60−500	36
9	Ag@AuNSt	seed-mediated, gold coating		100 °C, RT	70−110	37
10	Au@AgNSt	seed-mediated, silver coating	CTAB	100 °C	50−70	38
11	AuCuNSt	seed-mediated	HDA	RT, 100 °C	∼200	39
12	AuCuNSt	seed-mediated	OLA, HDA	RT, 130 °C	130−220	40
13	hAuAgNSt	seed-mediated, galvanic replacement		RT	150−300	13

[a]Abbreviations: AuNSt: gold nanostar, AgNSt: silver nanostar, Ag@AuNSt: silver−gold core−shell nanostar, Au@AgNSt: gold−silver core−shell nanostar, AuCuNSt: gold−copper nanostar, hAuAgNSt: semihollow gold−silver nanostar, SDS: sodium dodecyl sulfate, AOT: dioctyl sodium sulfosuccinate, BDAC: benzylhexadecyldimethylammonium chloride, HDA: hexadecylamine, OLA: oleylamine, CTAB: cetyltrimethylammonium bromide, PVP: poly(vinylpyrrolidone), and RT: room temperature.

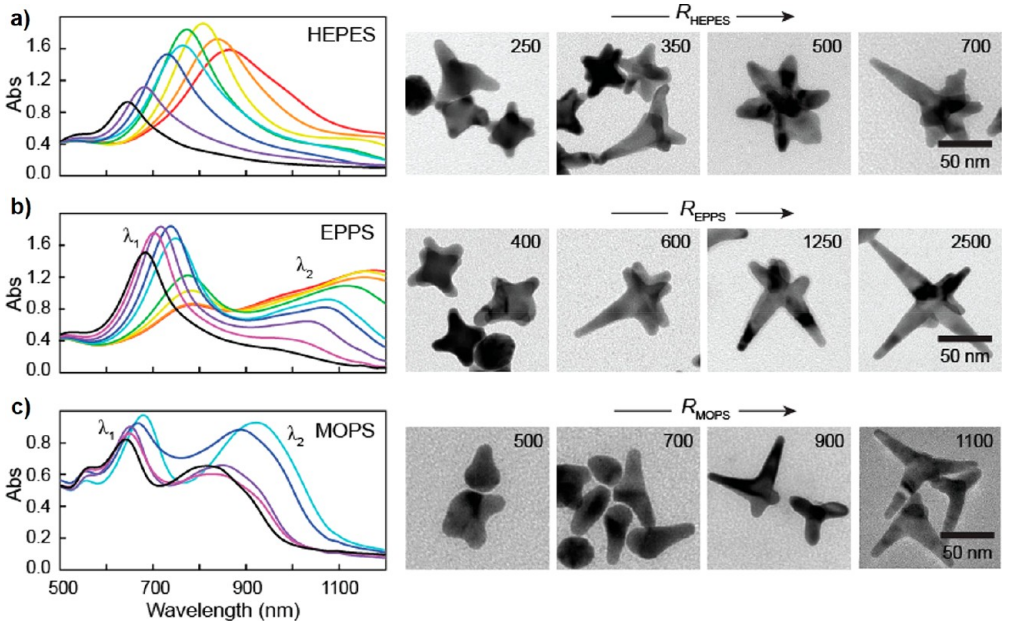

Figure 4. Absorbance spectra and TEM micrographs of AuNSts synthesized with (a) 250−750 R_{HEPES}, (b) 400−2500 R_{EPPS}, and (c) 500−1100 R_{MOPS}. From left to right is the lowest concentration (black) to the highest concentration (red or cyan). The number in the upper right-hand corner of each image is the corresponding R_{buffer} value. Adapted with permission from ref 29. Copyright 2016 American Chemical Society.

another unique advantage inherent to noble metal nanostars. In addition to enhancing the physical,[20] optical,[21] electronic,[22] or chemical[23] properties of the plasmonic nanostructures, the greatly intensified electric fields of illuminated plasmonic nanostars also enable many exotic applications that are unconventional for other plasmonic nanostructures, such as field electron generation[24] or the optical control of electrical currents.[25]

With many unique advantages over other more conventional nanostructures, plasmonic nanostars have the potential to greatly advance many current applications and enable the development of the next generations of important technologies, which can benefit human life or resolve urgent environmental problems. Despite the vast potential of plasmonic nanostars, a more rigorous understanding and better technological control are needed to realize the promise of this nascent class of nanostructures. Significant challenges still remain before the vast potential of plasmonic nanostars can be realized, such as the stability of gold nanostars in their unfunctionalized state.[13,28] Other areas with significant room for improvement include more reliable methodologies to control the optical properties and the ability for large-scale fabrication. Toward these efforts, this Review aims to provide a comprehensive picture of the current status of research, development, and applications of plasmonic nanostars for advanced technologies and utilizations, ranging from targeted cancer eradications and diagnoses to SARS-CoV-2 vaccines or next-generation photovoltaic cells.

2. SYNTHESIS OF PLASMONIC NANOSTARS

To synthesize plasmonic nanostars with various sizes, compositions, and optical properties, multiple methods have been developed over the last 15 years using different approaches and reagents. Table 1 summarizes some representative methods

https://doi.org/10.1021/acsanm.2c02533
ACS Appl. Nano Mater. 2022, 5, 14051−14091

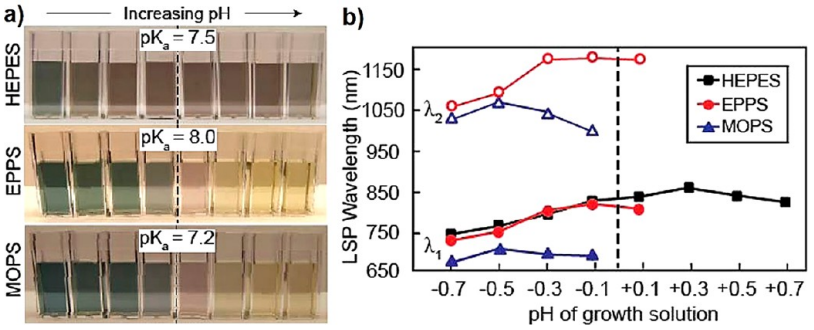

Figure 5. pH dependence of HEPES-, EPPS-, and MOPS-AuNSt formation throughout their respective buffering ranges. (a) Photographs of the solutions at different pH values; $pK_a \pm 0.7$. (b) Corresponding peak wavelengths of the absorbance spectra of AuNSts synthesized from solutions with different pH values. The solid symbols correspond to λ_1, and the open symbols correspond to λ_2. Adapted with permission from ref 29. Copyright 2016 American Chemical Society.

for the syntheses of plasmonic nanostars with varying compositions and size ranges.

Monometallic nanostars, the first members of star-shaped plasmonic nanostructures, have been synthesized by different methods under various conditions (Table 1, entries 1−8). In a recent report,[29] Chandra et al. described the fabrication of gold nanostars (AuNSts) by a seedless synthesis method based on Good's buffers. By changing the synthetic parameters, the authors demonstrated the capability to tailor the dimensions, shape, and optical properties of the synthesized AuNSts. Specifically, the study investigated the effects of different Good's buffers, such as 4-(2-hydroxyethyl)-1-piperazineethanesulfonic acid (HEPES), 4-(2-hydroxyethyl)-1-piperazinepropanesulfonic acid (EPPS), and 3-(*N*-morpholino)propanesulfonic acid (MOPS), on the size and shape of the resulting AuNSts. The results in Figure 4 show that the AuNSts synthesized with HEPES buffer had only one LSPR peak (Figure 4a), but the AuNSts synthesized with EPPS and MOPS buffers had two LSPR peaks, λ_1 and λ_2 (Figures 4b and c). The authors attributed the pronounced emergence of the secondary LSPR peaks of the EPPS- and MOPS-AuNSts to their longer star branches compared to the star branches of HEPES-AuNSts. For all three buffers, the authors also studied the effects of R_{buffer} ([buffer]/[$HAuCl_4$] ratio) on the morphologies of the resulting AuNSts. Specifically, when R_{buffer} was increased, more buffer molecules bound to the particles and directed the particle growth, leading to more Au ions being reduced onto some specific facets of the nanoparticles. This directed growth led to AuNSts with longer branches, as observed by the TEM micrographs shown in Figure 4.

The authors also studied the influence of the pH of the synthesis solution on the stability of the resulting AuNSts. The pH values of the synthesis solutions were adjusted by adding NaOH to the buffers. For the HEPES synthesis solution (pK_a = 7.5), stable AuNSts were formed throughout the entire buffering range of 6.8−8.2 (Figure 5a) with slight red shifts in the LSPR peak wavelengths (Figure 5b). However, for both the EPPS (pK_a = 8.0) and MOPS (pK_a = 7.2) synthesis solutions, stable AuNSts could be obtained only from the synthesis solutions with pH values below or equal to the pK_a values of the buffers. At pH values above the buffer pK_a values, the aggregation of the EPPS- and MOPS-AuNSts occurred (Figure 5a), which limited the synthetic range of these buffers. This work provided further insights into the influence of synthesis solution conditions on the seedless growth of AuNSts, which can be valuable when optimizing the synthesis conditions to obtain AuNSts with desired properties. Many other studies on the syntheses of monometallic plasmonic nanostars were also reported using either seedless (one-pot) methods[33−35] or seed-mediated processes with[30−32] and without the use of surfactants.[28]

The applications of conventional monometallic AuNSts are quite limited because they have an optical window that only ranges from the red end of the visible region to the near-infrared region. Recently, Ngo et al. were the first to report the fabrication of semihollow gold−silver nanostars (hAuAgNSts) with a new optical window in the ultraviolet and visible regions.[13] This work utilized a properly tuned galvanic replacement process of presynthesized silver nanostars (AgNSts) in open-air conditions at room temperature. The aqueous etching solution contained $HAuCl_4$ and potassium carbonate (K−Au). The procedure allowed the formation of bimetallic hAuAgNSts with good size distributions. The corresponding energy-dispersive X-ray spectroscopy (EDX) elemental maps showed uniform distributions of both gold and silver throughout the structures of the hAuAgNSt, which confirms the presence of both metals in these unique bimetallic semihollow nanostars.

The hAuAgNSts exhibited a linear correlation between the Au contents in the resulting nanostars and the K−Au/AgNSt ratios used in the fabrication process.[13] This linear relationship allows hAuAgNSts to be synthesized with a desired Au content by adjusting the galvanic replacement conditions accordingly. These bimetallic nanostars showed a new LSPR active window for plasmonic nanostars in the ultraviolet and visible regions, which is spectrally complementary to the existing optical window of AuNSts. Notably, the LSPR peak position of the hAuAgNSts was also demonstrated to be tunable through the control of the Au contents in their structures. The linear predictability of the Au contents led to a much more versatile LSPR composition-based tunability of hAuAgNSts than the size-based tunability of AuNSts, as shown in Figure 4. The new operational window offered by hAuAgNSts and the facile LSPR composition-based tuning method reported in this study have expanded the working range and further advanced the utilization prospect of plasmonic nanostars, especially for solar-powered applications, such as photocatalysis and photovoltaics. Several other studies also demonstrated different synthetic methods for bimetallic nanostars, such as Ag@Au,[37] Au@Ag,[38] or Au−Cu nanostars.[39,40]

https://doi.org/10.1021/acsanm.2c02533
ACS Appl. Nano Mater. 2022, 5, 14051−14091

Table 2. Plasmonic Nanostars for Medical Diagnostics[a]

core NP	combinatory components	diagnostic target	diagnostic method	level of study	key results	ref
AuNSt–SiO_2	label DNAs	cancer miRNAs	bioimaging	in vitro	21-fold fluorescence enhancement and 0.21 pM miRNA-21 LOD	27
Ag–AuNSt	Raman reporter molecule	CRS biomarker	SERS immunoassay	in vitro, clinical	LOD up to 0.41 fg/mL	45
AuNSt	Raman reporter molecule	breast cancer cell	SERS imaging	in vitro	five types of breast cancer cells with reproducible signals and noncytotoxicity	46
AuNSt	graphene oxide	breast cancer exosomes	SERS	in vitro	LOD of 380 exosomes/mL and FDTD simulation results showed 10^4-enhanced SERS signal	47
AuNSt	SERS tag	prostate cancer PSMA	SERS	in vitro	quantification of PSMA protein at pM-concentration both at the single-cell level and in tissue microassays	48
AuNSt	aptamer probe	CTCs	electrochemical current	in vitro, clinical	ultrasensitive label-free detection of CTCs at concentrations as low as 5 cells/mL	49
AuNSt	LK26 antibody	ovarian cancer folate receptors	ratiometric imaging	in vitro, in vivo	detection of ovarian tumors as small as 370 μm	50
AuNSt	N/A	breast cancer	SERS	in vitro	label-free discernment of three cell phenotypes based solely on the acquired Raman spectra	51
AuNSt	EpCAM aptamer	CTCs	electrochemical aptasensing	in vitro, clinical	single-cell detection of target cancer cell even in human serum	52
AuNSt	N/A	cervical and liver cancer	SERS imaging	in vitro	SERS detection of cancer cells at a higher sensitivity with AuNSts than with Au nanospheres	53
AuNSt	glycyrrhetinic acid	liver fibrosis	SERS	in vivo	selectively detected liver fibrosis and demonstrated good biocompatibility	54
AuNSt@ Ag@SiO_2	anti-AFP antibody	liver cancer biomarker AFP	SERS immunoassay	in vitro	detected AFP at a low LOD of 0.72 pg/mL and a wide range of linear detection from 3 pg/mL to 3 μg/mL	55
AuNSt@ SiO_2	uPAR- and EGFR-targeting peptides	breast cancer	SERS imaging	in vitro	simultaneous quantitative detection and discrimination of both biomarkers without background interference	56

[a]Abbreviations: miRNA: microRNA, LOD: detection limit, CRS: cardiorenal syndrome, SERS: surface-enhanced Raman spectroscopy, FDTD: finite-difference time domain, PSMA: prostate-specific membrane antigen, CTCs: circulating tumor cells, N/A: not applicable, EpCAM: epithelial cell adhesion molecule, AFP: α-fetoprotein, uPAR: urokinase plasminogen activation receptor, and EGFR: epidermal growth factor receptor.

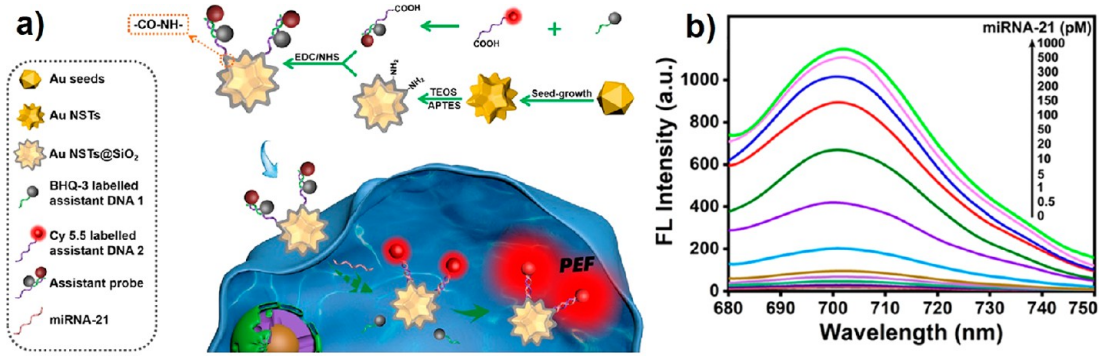

Figure 6. (a) Schematic illustration of the AuNSt@SiO_2-based plasmon-enhanced fluorescence probe for the in situ detection of intracellular miRNA-21 and (b) fluorescence spectra emitted by the probe in the presence of miRNA-21 at different concentrations. Adapted with permission from ref 27. Copyright 2021 American Chemical Society.

3. APPLICATIONS OF PLASMONIC NANOSTARS

The inherently large surface area, high number of plasmonic hotspots, and excellent biocompatibility make plasmonic nanostars particularly attractive for a wide and diverse range of applications. In the past decade, for example, plasmonic nanostars (especially gold nanostars) have been shown to enhance a wide range of existing technologies and to enable a multitude of new technological and scientific capabilities ranging from ultrasensitive detection, enhanced catalysis, and efficient photovoltaics to multimodal imaging, biomedical therapies, and neural modulation. In this section, we will highlight the important advances of applications of plasmonic nanostars in these fields.

3.1. Biomedical Applications. Noble metal-based plasmonic nanostructures have attracted great research interest concerning biomedical diagnostics because of their high biocompatibilities and unique properties, including superior surface areas and large numbers of plasmonic hotspots.[41] Under the illumination of electromagnetic waves with suitable wavelengths, the plasmonic resonance generated by these nanostructures can enhance many physical phenomena, such as Raman scattering and fluorescence.[42] Such enhanced effects of NSt-based materials have been utilized in many biomedical applications, including diagnostics, drug delivery, photothermal and photodynamic therapies, and antibacterial applications.

3.1.1. Plasmonic Nanostar-Enhanced Diagnostics. The superior specific areas and numbers of hotspots[27] of nanostars compared to those of other plasmonic nanostructures (e.g., spheres, rods, triangles, or cubes) make them particularly interesting for diagnostic technology development. Specifically, the plasmonic resonance wavelengths in the first and second biological optical windows[43] together with the excellent

https://doi.org/10.1021/acsanm.2c02533
ACS Appl. Nano Mater. 2022, 5, 14051−14091

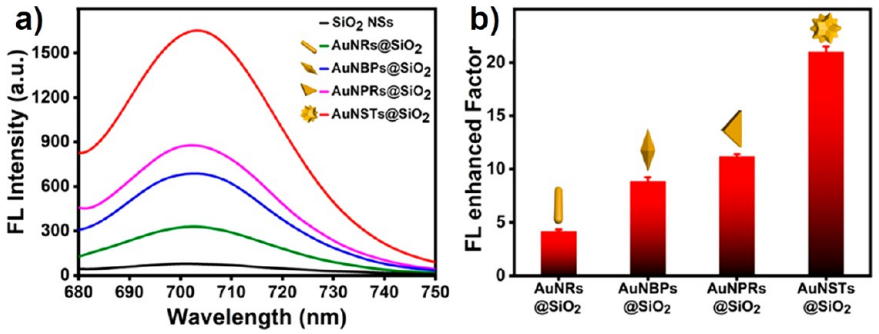

Figure 7. (a) Fluorescence spectra of silica-coated nanoparticles with different morphologies and (b) their corresponding fluorescence-enhanced factors. Adapted with permission from ref 27. Copyright 2021 American Chemical Society.

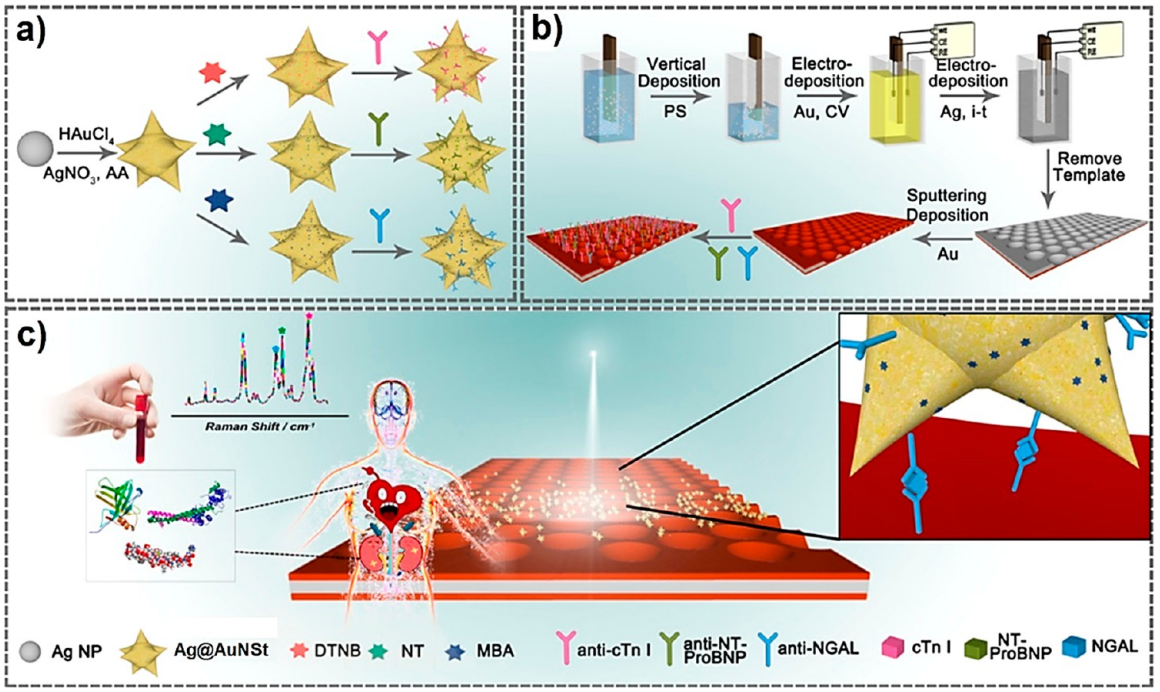

Figure 8. (a) Fabrication of the three Raman reporter molecules and three antibody-functionalized Ag@AuNSt hybrid nanotags. (b) Preparation of the Ab1-functionalized 3DOM Au−Ag−Au SERS substrate and (c) the SERS immunoassay platform for the simultaneous detection of cTnI, NT-ProBNP, and NGAL. Adapted with permission from ref 45. Copyright 2019 American Chemical Society.

biocompatibility[44] of gold nanostars endow them with great potential in high-performance diagnostics for many medical conditions and diseases. Table 2 summarizes the current use of plasmonic nanostars in the diagnosis of various diseases.

In a recent report,[27] Gao et al. reported the in situ detection and imaging of intracellular microRNAs (miRNAs) using tumor cell miRNA-21. The work included the fabrication of plasmon-enhanced fluorescence (PEF) probes by conjugating silica-coated AuNSts with BHQ-3- and Cy5.5-labeled assistant DNAs, which were partially hybridized with each other. In the presence of miRNA-21, Cy5.5-labeled assistant DNAs were completely hybridized with miRNA-21, and BHQ-3 DNAs were removed. This led to an increase in the fluorescence signal because the signal-suppressing fluorescence resonance energy transfer between BHQ-3 and Cy5.5 DNAs was disrupted, as illustrated in Figure 6a. With the minimum fluorescence signal observed at 0.5 pM (Figure 6b), the authors calculated a limit of detection (LOD) of 0.21 pM ($3\sigma/s$) for miRNA-21. The study also demonstrated the capability to adjust the fluorescence enhancement of the PEF probes by regulating the silica shell thickness, with a maximum enhancement of 21-fold obtained at a shell thickness of ∼22 nm.

Through a comparison with other nanostructures, such as nanorods (4.2-fold fluorescence enhancement), nanobipyramids (8.9-fold fluorescence enhancement), and triangular nanoprisms (11.2-fold fluorescence enhancement), the superiority of nanostars was demonstrated with the 21-fold enhancement of the fluorescence signal (Figure 7).[27] The authors attributed this result to the large numbers of symmetric hotspots present in the AuNSt-based probes, which produced stronger localized electric fields and led to a higher sensitivity and improved LOD. The experimental investigation of the influences of nanoparticle morphologies on the fluorescence enhancement in this work provides valuable guidance for the future design and utilization of plasmonic nanostars.

Early diagnosis of cardiorenal syndrome (CRS) is important for treating the disease effectively and preventing the dysfunction of the heart and kidneys in affected patients. Recently, Su et al. reported a sandwich immunoassay utilizing surface-enhanced Raman scattering (SERS) for the simulta-

https://doi.org/10.1021/acsanm.2c02533
ACS Appl. Nano Mater. 2022, 5, 14051−14091

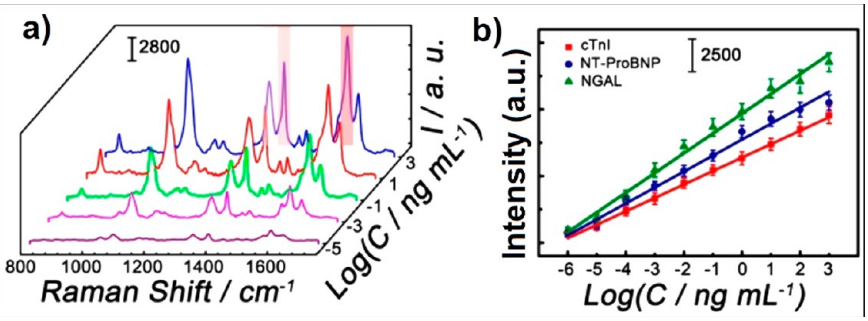

Figure 9. (a) Integrated SERS spectra of the immunosensor after cTnI, NT-ProBNP, and NGAL were incubated at different concentrations. (b) Calibration curves of nTnI, NT-ProBNP, and NGAL on a semilog scale. Adapted with permission from ref 45. Copyright 2019 American Chemical Society.

Table 3. Plasmonic Nanostars for Vaccine and Drug Delivery[a]

core NP	combinatory components	delivery target	triggering/ transport mechanism	level of study	key results	ref
AuNSt	chitosan	intranasal SARS-CoV-2 vaccine	N/A	in vitro, in vivo	strong and consistent antibody surge, effective neutralization of viruses, enhanced antibody response within 1 week	64
AuNSt	silica, liposome	DOX	photothermal with NIR	in vitro	enhanced cytotoxicity and growth inhibition to cancer cells; capable of codelivering hydrophilic−hydrophobic drugs	65
AuNSt	i-motif DNA	DOX	NIR, pH	in vitro	effectively triggered dug release, good biocompatibility, combined photothermal effect enhanced therapeutic efficiency	66
Fe_3O_4@ AuNSt	FAM-DEVD, PEI, SPDP	RGD-TRAIL and ATAP	external magnetic field	in vitro, in vivo	successful site-specific delivery to tumor, outstanding inhibition of tumor growth, monitoring of cell apoptosis in real-time	67
AuNSt	cucurbit[7]uril	camptothecin	NIR	in vitro	effective synergistic anticancer photothermal therapy and chemotherapy	68
AuNSt	HApt	HApt	N/A	in vitro	HApt-AuNSt inhibited cancer cell proliferation with induced cell death	69
AuNSt	lipid bilayer nanomembrane	DOX	N/A	in vitro, in vivo	significantly enhanced delivery of DOX to cancer cells compared to spherical NPs	70
AuNSt	EpCAM antibody	siRNA, mRNA	NIR laser	in vitro	site-specific optoporation and selective delivery	71
AuNSt	ZIF-8	bisbenzimide	NIR light	in vitro	high drug loading and thermoplasmonic capabilities together with aqueous and cellular stability	72
Fe_3O_4@ SiO_2− AuNSt	mesoporous silica	paclitaxel	NIR laser	in vitro	successful drug delivery and photothermal therapy with low toxicity	73
AuNSt@ SiO_2	octadecyltrimethoxysilane, heneicosane	DOX	NIR laser	in vitro	optically controlled release with no cytotoxicity even at low laser power density	74
AuNSt	HApt	DOX	NIR light	in vitro	high degree of on-demand DOX release with enhanced toxicity against cancer cells	75
AuNSt	penetrating peptide	Ru(II) complex	NIR light	in vitro, in vivo	luminescence-tracked drug delivery with high biocompatibility, hemocompatibility, and low toxicity	76

[a]Abbreviations: SARS-CoV-2: severe acute respiratory syndrome coronavirus 2, DOX: doxorubicin, NIR: near-infrared, AuNSt: gold nanostar, DEVD-FAM: carboxyfluorescein-conjugated caspase 3-responsive aspartic-glycine-valine-aspartic acid, PEI: polyethylenimide, SPDP: *N*-succinimidyl 3-(2-pyridyldithio) propionate, RGD: arginine-glycine-aspartic acid, TRAIL: tumor-necrosis-factor-related apoptosis-inducing ligand, ATAP: amphiphilic tail-anchoring peptide, HApt: anti-HER2 aptamer, NPs: nanoparticles, EpCAM: epithelial cell adhesion molecule, and ZIF-8: zeolitic-imidazolate-framework-8.

neous detection of cardiac troponin I (cTnI), the N-terminal prohormone of brain natriuretic peptide (NT-ProBNP), and neutrophil gelatinase-associated lipocalin (NGAL) for early CRS diagnoses.[45] The authors used silver−gold core−shell nanostars (Ag@AuNSt) (Figure 8a) labeled with Raman reporter-molecule nanotags. The Raman reporters used in this study include 4-mercaptobenzoic (4-MBA), 5′-dithiobis(2-nitrobenzoic acid) (DTNB), and 2-naphthalenethiol (NT). The nanotags were then added to a macroporous Au−Ag−Au plasmonic array, which was used as a substrate in the immunoassay technique (Figure 8c). The array was fabricated by a series of deposition processes before anti-nTnI, anti-NT-ProBNP, and anti-NGAL antibodies were immobilized on its surface, as illustrated in Figure 8b.

A greatly enhanced SERS signal (Figure 9a) of the immunosensors was obtained as a result of the plasmonic near-field coupling that occurred when the plasmonic star nanotags and substrate came into contact through selective binding between the targeted antigens and their antibodies, which were grafted onto the nanotags and plasmonic arrays, as shown in Figure 8c.[45] This work also observed linear relations between SERS signals and antigen concentrations in the range of 1 fg/mL to 1 μg/mL (Figure 9b). Using linear regression calculations, the authors determined LODs of 0.76, 0.53, and 0.41 fg/mL for cTnI, NT-ProBNP, and NGAL, respectively. Such LODs are orders of magnitude smaller than those of other reported plasmonic nanoparticle-based platforms for the detection of cTnI,[57,58] NT-ProBNP,[59] and NGAL.[60,61] These

https://doi.org/10.1021/acsanm.2c02533
ACS Appl. Nano Mater. 2022, 5, 14051−14091

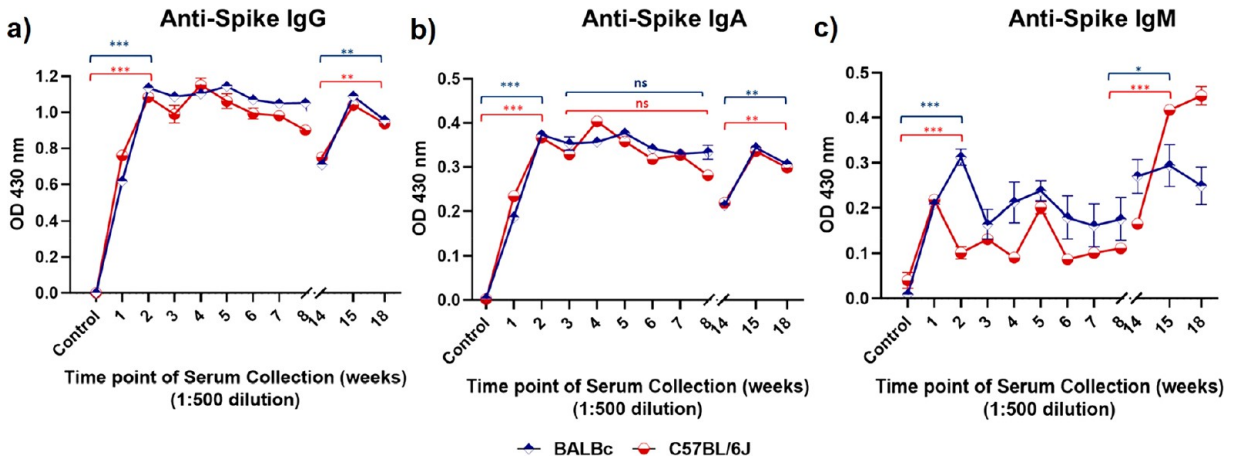

Figure 10. Antibody-mediated immune responses after intranasal immunization of SARS-CoV-2 S protein DNA vaccine using AuNSt-chitosan measured against (a) IgG, (b) IgA, and (c) IgM levels over 18 weeks. Adapted with permission from ref 64. Copyright 2021 American Chemical Society.

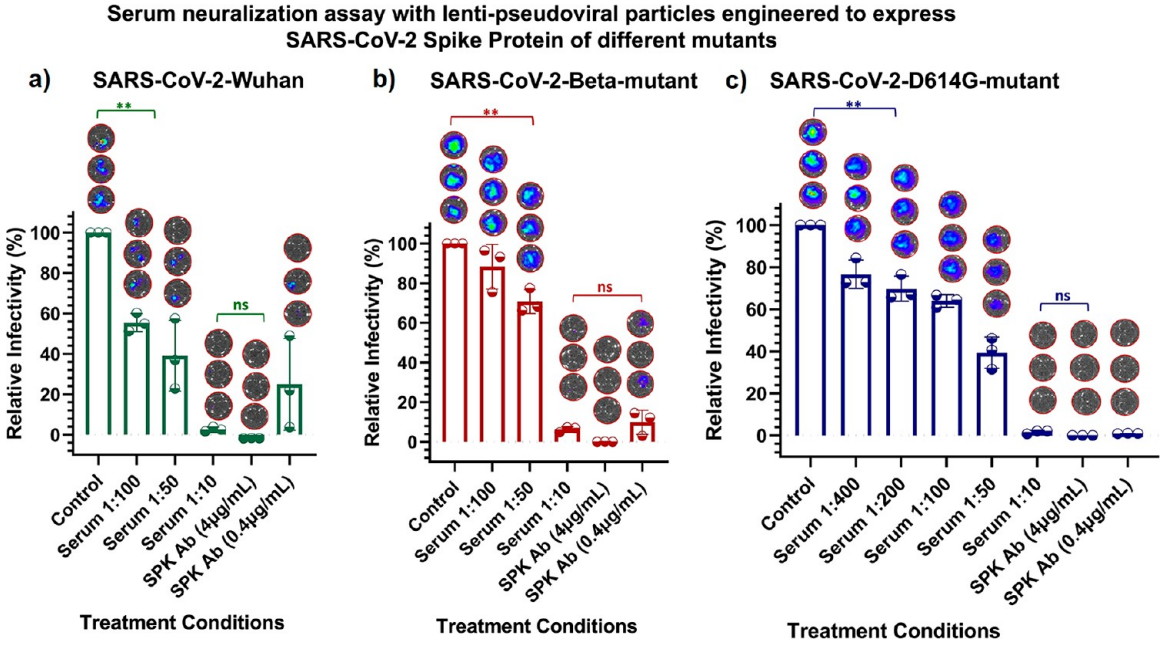

Figure 11. Inhibition of infectivity against lentiviral particles engineered with (a) S protein SARS-CoV-2-Wuhan, (b) SARS-CoV-2-beta mutant, and (c) SARS-CoV-2-D614G mutant variants. Adapted with permission from ref 64. Copyright 2021 American Chemical Society. SPK Ab: simultaneous pancreas kidney antigen.

dramatic decreases in LODs enabled by the use of plasmonic nanostars highlight the superiority of this unique type of plasmonic nanostructure in developing advanced diagnostic technologies. The reported device was also able to perform multiplex detection of three biomarkers, DTNB, NT, and 4-MBA, in a single assay by using three distinguishable 1323, 1363, and 1584 cm^{-1} SERS peaks. This multiplexing capability not only reduced the device use but also allowed low-cost and fast diagnostics. This work demonstrated the unique strength of plasmonic alloy nanostars, especially their inherently high numbers of hotspots, in enhancing advanced spectroscopic diagnostic techniques.

In addition to the highlighted works above, many remarkable studies on AuNSt-based diagnostics have also been reported recently, as listed in Table 2. Plasmonic nanostars have been used to develop diagnostic methods for various detrimental cancers, including breast,[46,47,49,51,56] prostate,[48] ovarian,[50] cervical,[53] and liver cancer.[55] Until now, most of the studies have remained focused on cancer-related techniques, possibly owing to the severity of the diseases and the ease of adaptability when transitioning from the well-known gold nanoparticles, the most popular type of plasmonic nanoparticles, to gold nanostars. However, the use of plasmonic nanostars to diagnose other medical conditions can also facilitate promising research areas when AuNSts and/or other plasmonic nanostars are combined with suitable conjugates in proper structures.

3.1.2. Vaccine and Drug Delivery with Plasmonic Nanostars. The prevention and treatment of critical diseases, such as cancers or viral infections, are always attracting great attention. With the rapid progress of nanomaterial studies, a great amount of research effort has been spent on inventing nanobased methods for preventing and treating diseases while minimizing the unintended collateral damage that is inherent to traditional techniques (e.g., chemo- and radiotherapy or general

https://doi.org/10.1021/acsanm.2c02533
ACS Appl. Nano Mater. 2022, 5, 14051−14091

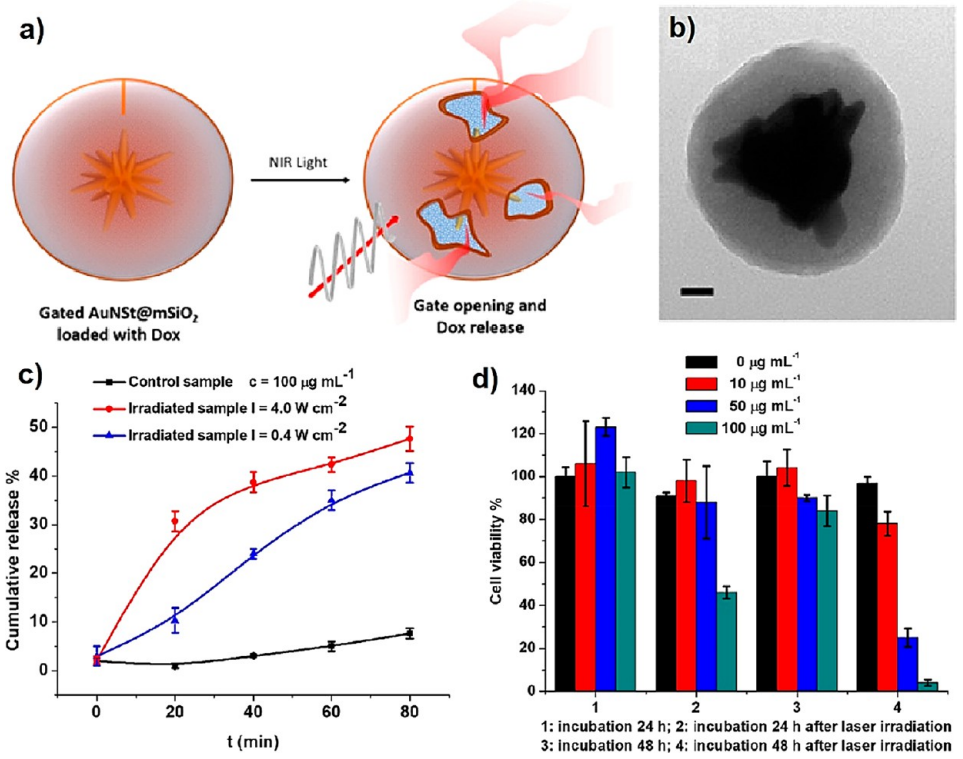

Figure 12. (a) Illustration and (b) transmission electron microscopy image of the drug release system based on AuNSts coated with mesoporous silica shells and paraffin as a thermosensitive release gate. (c) Cumulative release of Dox from AuNSt-based nanocarriers under different laser powers. (d) Viability of HeLa cancer cells in the presence of the Dox-loaded AuNSt drug carriers at different incubation times and concentrations upon 808 nm laser irradiation at 4 W/cm^2 for 15 min. Adapted with permission from ref 74. Copyright 2018 American Chemical Society.

pharmaceutical intake).[62] High-specificity drug delivery enabled by nanostructures has been an attractive theme in developing applications of nanostructures.[63] The large surface area-to-volume ratios and high numbers of hotspots of plasmonic nanostars are great advantages for the development of efficiently targeted vaccine and drug delivery technologies based on this unique class of nanomaterials. Recent studies on vaccine and drug delivery utilizing plasmonic nanostars are summarized in Table 3.

The current COVID-19 global pandemic caused by SARS-CoV-2 and its variants has been devastating the world medically, economically, and socially. Efficient and safe vaccines are arguably still the most feasible long-term approach to ending this medical crisis, and nanotechnology has contributed significantly to that effort.[77] In a recent study,[64] Kumar et al. studied the effects of intranasally administered AuNSt-based DNA vaccines against SARS-CoV-2 in mouse models. The work used chitosan-coated AuNSts to encapsulate the encoded sequence of SARS-CoV-2 S protein DNA (pcDNA) to form a vaccine delivery nanocarrier. Delivery of the AuNSt-based DNA vaccine yielded successful expression of the antigen in the respiratory mucosa and lungs of mouse models, which led to an enhanced antibody response, as shown in Figure 10. The antibody response developed as early as 1 week after the administration of three doses of DNA vaccine and was consistently elevated for several months without a significant decline in both the BALB/c and C57BL/6J mouse models.

The AuNSt-facilitated DNA vaccine also effectively neutralized pseudoviruses expressing the S proteins of different SARS-CoV-2 variants (Wuhan, beta, and D614G), as shown in Figure 11.[64] The findings of this work highlight the merits of gold nanostars as carriers for delivering genetic vaccines and therapies both in vitro and in vivo. It also demonstrated a promising approach for developing a long-lasting and wide-spectrum antibody response to combat the increasing number of SARS-CoV-2 variants.

In addition to antiviral applications, cancer-related therapy has been a major focus of advanced nanoparticle-based drug delivery technologies.[78] The development of plasmonic nanostars in recent years has facilitated the use of this promising new type of nanostructure for biomedical targeted delivery technologies.[74] Montoto et al. developed a laser-induced delivery method for anticancer drugs based on gold nanostars.[74] The silica-coated AuNSts were used as doxorubicin (Dox) nanocarriers (Figures 12a and b), which could be triggered by an NIR laser to release the anticancer drug through the melting of the encapsulating paraffin, as illustrated in Figure 12a. Notably, the cumulative release of Dox over time can be adjusted by changing the laser power (Figure 12c). With proper dosages of Dox and incubation times after drug delivery, an eradication of ~95% of HeLa cancer cells was achieved after 10−15 min of laser irradiation and 48 h of incubation (Figure 12d). This level of cancer cell eradication is significantly higher than those of gold nanocages[79] or nanorods[80] under similar conditions, indicating the advantage of plasmonic nanostars. The Dox-loaded AuNSt carriers also showed no leakage of the cargo in an aqueous solution before significant payload delivery was observed upon NIR irradiation, thus minimizing the cytotoxicity of the drug toward noncancer cells. The results demonstrated in this report show the potential of AuNSts and other plasmonic nanostars as components of efficient drug delivery methods with less collateral damage than traditional treatments such as chemo- or radiotherapy.

https://doi.org/10.1021/acsanm.2c02533
ACS Appl. Nano Mater. 2022, 5, 14051−14091

Table 4. Photothermal and Photodynamic Therapy Applications of Plasmonic Nanostars[a]

core NP	combinatory components	therapy's target	irradiation source, power density	level of study	key results	ref
AuNSt	anti-PD-L1 antibody	MB49 bladder cancer	808 nm laser, 0.6 W/cm^2	in vivo	complete eradication of and long-lasting immunity against MB49 cancer cells in mice	82
AuNSt	ZIF-8	photothermal cyclization in cells	808 nm laser, 10 W/cm^2	in vitro	photothermal-promoted chemical reactions in living cells for light-controlled therapies	83
AuNSt	siHSP72/HA/CD44	breast cancer	808 nm laser, 1 W/cm^2	in vitro, in vivo	successfully sensitized TNBC cells for PTT with superior conversion efficacy and hemo-/biocompatibility	84
AuNSt	glycopolymer	cancer	808 nm laser, 1 W/cm^2	in vitro, in vivo	selectively targeted and photothermally reduced tumors with excellent biocompatibility	85
AuNSt	GO	breast cancer	808 nm laser, 0.75 W/cm^2	in vitro	cellular internalization and remarkable photothermal effect with extremely low cytotoxicity	86
AuNSt	NLS, HA, CD44	cancer	808 nm laser, 1 W/cm^2	in vitro, in vivo	high-accuracy tumor targeting, internalizing, and photothermal anticancer effect	87
AuNSt	N/A	cervical cancer	980 nm laser, 1.34 W/cm^2	in vitro	exhibited significantly higher photothermal transduction than AuNR and Au nanosphere as well as effective cancer cell ablation	88
AuNSt@MnO_2	PEI, Ce6, HA	cancer cells	808 nm (3 W/cm^2) and 650 nm (30 mW/cm^2)	in vitro	PTT/PDT synergistic therapy killed cancer cells much more effectively than single therapy	89
AuNSt-dPG	HA, RA	CSCs eradication	808 nm laser, 1 W/cm^2	in vitro, in vivo	effective elimination of the self-renewal of CSCs and tumor growth and prevention of relapse	90
AuNSt	Pt	MDR tumor	NIR laser, 0.9 W/cm^2	in vitro, in vivo	efficient photothermal ablation and ferroptosis of MDR tumors by Pt−AuNSt with good biocompatibility	91

[a]Abbreviations: PD-L1: programmed death-ligand 1, siHSP72: siRNA against heat shock protein 72, HA: hyaluronic acid, TNBC: triple-negative breast cancer, CD44: TNBC-overexpressed surface molecule, PTT: photothermal therapy, NLS: nuclear localization sequence, N/A: not applicable, PEI: polyethylenimine, PDT: photodynamic therapy, dPG: dendritic polyglycerol, RA: retinoic acid, CSCs: cancer stem cells, and MDR: multidrug-resistant.

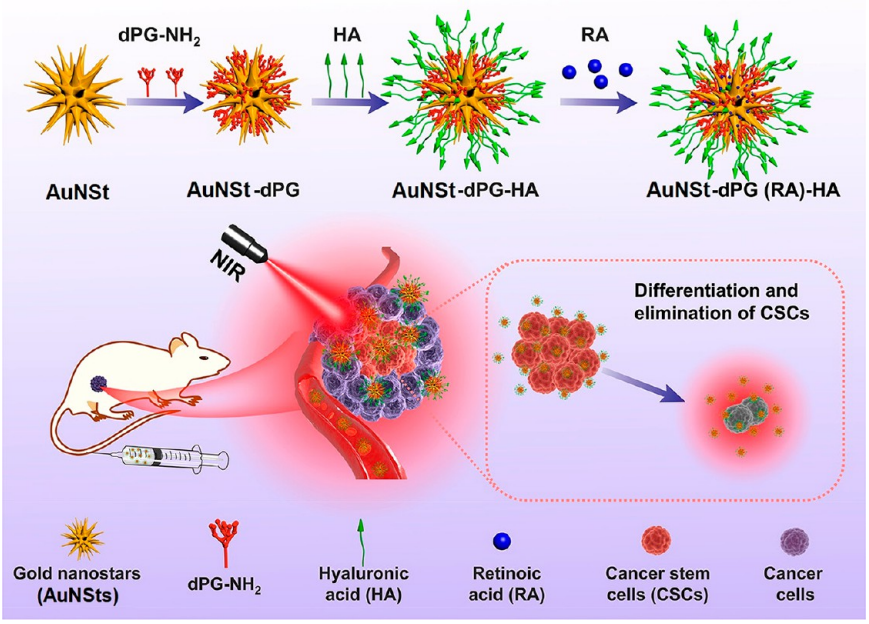

Figure 13. Schematic of RA-loaded AuNSt-dPG for targeted PTT in breast cancer stem cells. Reproduced with permission from ref 90. Copyright 2021 American Chemical Society.

Many other recent reports on nanostar-based drug delivery methods are summarized in Table 3, with delivery targets ranging from anticancer drugs[65,66,70] to genetic agents.[69,71] Many of these nanostar-based vaccine and drug delivery methods utilized the large numbers of hotspots present on plasmonic nanostars to enhance light-triggered heating effects, which enabled faster drug release compared to those of other plasmonic nanostructures. Furthermore, the more efficient heating facilitated by plasmonic nanostars can also enable even more effective medical techniques through the incorporation of photothermal therapy into synergistic technologies, which will be discussed in more detail in Section 3.1.5 below.

3.1.3. Photothermal and Photodynamic Therapy Enabled by Plasmonic Nanostars. Localized surface plasmon resonance (LSPR), the collective resonant oscillation of free electrons in metal nanostructures under suitable electromagnetic irradiation, is a distinctive feature of plasmonic nanostructures.[3] Through the occurrence of LSPR, nanostructures can convert electromagnetic radiation energy into heat, which in turn can eliminate tumors through photothermal therapy (PTT) or can be used for other purposes. Furthermore, in combination with suitable photosensitizers, plasmonic nanostructures can trigger the production of radical oxygen species (ROSs) or other photochemical processes.[81] These ROSs can be used for

https://doi.org/10.1021/acsanm.2c02533
ACS Appl. Nano Mater. 2022, 5, 14051−14091

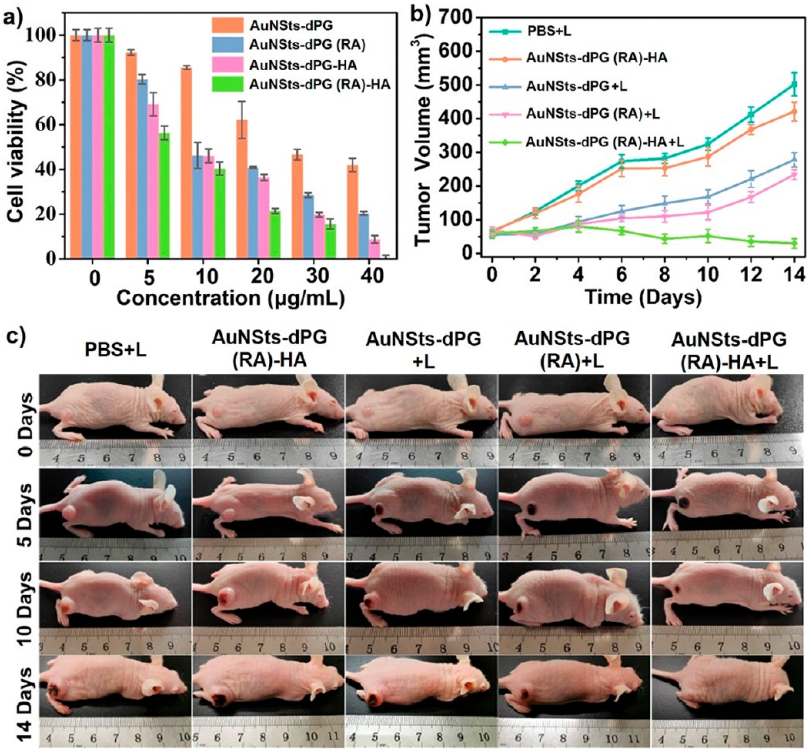

Figure 14. (a) Viabilities of MDA-MB-231 breast cancer cells treated with different AuNSt-based particles under laser irradiation for 10 min. (b) Tumor growth curves and (c) digital images of 4T1 tumor-bearing mice on different days injected with different AuNSt-based nanoparticles and treated with a laser (+L). Adapted with permission from ref 90. Copyright 2021 American Chemical Society.

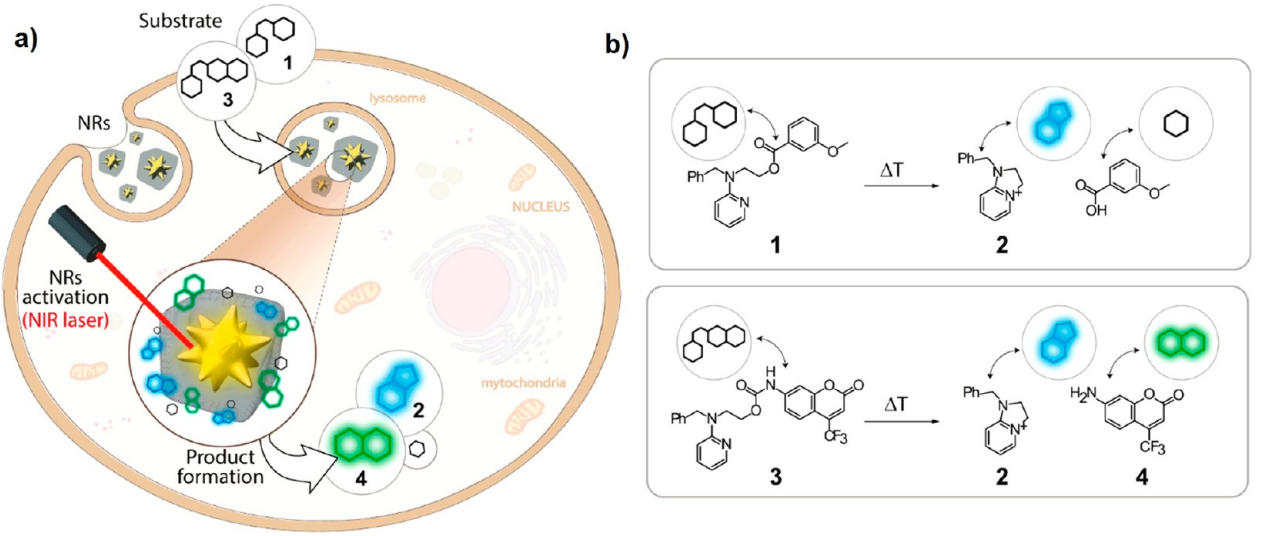

Figure 15. (a) Core−shell AuNSt-ZIF-8 nanoreactors for the photogated intracellular transformation of thermolabile substrates inside living cells (thermocyclization). (b) Reacting probes used (substrates 1 and 3) and fluorescent products (2 and 4) arising from the thermoplasmonic-promoted reaction. Adapted with permission from ref 83. Copyright 2021 American Chemical Society.

photodynamic therapy (PDT) in anticancer treatments with higher efficacy and fewer side effects compared to treatments involving the use of conventional plasmonic nanostructures. Recent works in PTT and PDT based on plasmonic nanostars are listed in detail in Table 4.

In a recent report,[90] Haag and co-workers developed a photothermal therapy for efficiently eradicating breast cancer stem cells (CSCs) both in vitro and in vivo using a AuNSt-based nanoplatform. In this work, the authors functionalized AuNSts with dendritic polyglycerol (dPG) for better biocompatibility, hyaluronic acid (HA) for effective CSC targeting, and retinoic acid (RA) for the differentiation of breast CSC types (Figure 13).

After being illuminated by an NIR laser for 10 min in the presence of the AuNSt-dPG-RA-HA nanocomplex at a concentration of 40 μg/mL, MDA-MB-231 breast cancer cells were almost totally eradicated, as shown in Figure 14a.[90] This level of MDA-MB-231 cancer cell eradication was significantly greater than those achieved by gold clusters[92] or gold nanorods,[93,94] demonstrating the comparatively greater photo-

https://doi.org/10.1021/acsanm.2c02533
ACS Appl. Nano Mater. 2022, 5, 14051−14091

thermal performance of plasmonic nanostars over those of conventional plasmonic nanostructures. The self-renewals of breast CSCs and tumor growth were also efficiently inhibited. This work also showed how the suppression of CSCs inhibited the formation and growth of the tumor by comparing the tumor sizes in mice treated with different AuNSt-based nanoparticles with/without laser irradiation. The results in Figure 14b revealed the significant inhibition of tumor growth and reduction in tumor size in mice treated with the AuNSt-dPG-RA-HA nanocomplex and illuminated with an NIR laser. In the mice treated with AuNSt-dPG-RA-HA but without NIR laser irradiation, the tumor size remained almost the same as that in the control group after 14 days (Figures 14b and c). The results highlighted the efficacy of the photothermal effect of the AuNSt-based nanoplatforms on CSC elimination and tumor reduction. These findings demonstrate the great potential of AuNSt-based platforms for efficient targeted eradication and prevention of cancer relapse.

In addition to photothermal therapy, photodynamic therapy, which involves photopromoted chemical reactions, has been another promising approach for light-controlled therapies enabled by plasmonic nanostructures.[95] In one of the few relevant reported studies in the field,[83] Pino and co-workers described the use of AuNSt-based core−shell nanoreactors (NRs) to carry out NIR-driven photothermal cyclizations inside living cells, as illustrated in Figure 15.

The nanoreactors included a AuNSt core embedded within a metal−organic framework (MOF) based on a polymer-stabilized zeolitic imidazole framework-8 (ZIF-8) (Figures 16a and b).[83] These nanoreactors were tested with HeLa cells, and the results showed that at low molar percentages of NR (%NR), a 98% yield of product 2 was obtained, as shown in Figure 16c (blue bar). The result demonstrated the feasibility of photothermally promoted chemical reactions in the interior of living cells using AuNSt-MOF nanocomposites upon NIR irradiation. Thus, this report further elaborated on the potential scope of AuNSts for light-controlled therapies in addition to photothermal therapy.

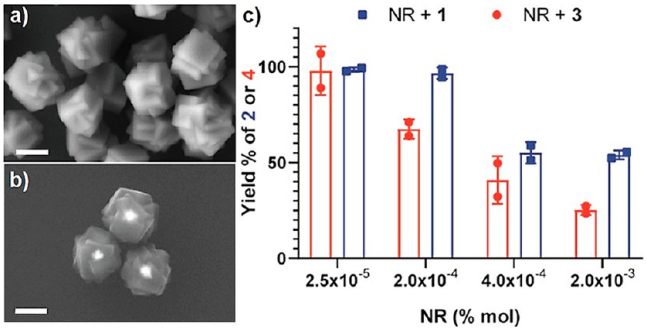

Figure 16. Scanning electron images of the AuNSt-ZIF-8 nanoreactors taken at (a) 3 and (b) 20 kV with a 200 nm scale bar. (c) Yields of product 2 (blue bars) and product 4 (red bars) after NIR treatment (8 W/cm^2 for 2 min) of substrate 1 or 3 with NRs dispersed in water (0.2 nM and 0.04 pmol) with different NR/substrate molar ratios. Adapted with permission from ref 83. Copyright 2021 American Chemical Society.

Other recent studies on the photothermal and photodynamic applications of plasmonic nanostars are summarized in Table 4. The majority of these studies focus on laser-activated therapy for cancer treatments ranging from breast[84,86] and cervical[88] to bladder cancer.[82] This myopic focus indicates the great potential for further explorations of plasmonic nanostars in regard to the light-enabled treatments of other noncancer diseases, such as viral infection.

3.1.4. Antibacterial Applications of Plasmonic Nanostars. Bacterial infections have a history as intractable public health problems, especially in developing countries. The development of nanomaterials has introduced new strategies for developing more efficient methods for the treatment of bacterium-induced diseases. By using a suitable stimulus, the heat and/or ROSs generated by nanostructures can circumvent the ever-increasing antibiotic resistance of bacteria, which is becoming a great threat to human society.[96] Owing to their unique photothermal heating, ROS-generating properties, or even their spiky morphologies, plasmonic nanostars have been studied and reported in many research efforts for antibacterial applications, as summarized in Table 5.

In a recent report,[102] Han and co-workers demonstrated the use of vancomycin (Van)-modified AuNSts (AuNSt@Van) for the selective targeting and effective eradication of methicillin-resistant *Staphylococcus aureus* (MRSA) bacteria. AuNSt@Van could target MRSA bacteria (as shown in Figure 17a), and when laser illumination was applied, the bacterial cell membranes were destroyed, resulting in an increase in the recorded red fluorescence signal arising from propidium iodide fluorescent dye staining (Figure 17b). The authors attributed the selective targeting of AuNSt@Van to the high affinity of Van for the cell wall of MRSA.

In vivo tests on mice infected with MRSA showed obvious reductions in the wound areas in the mice treated with AuNSt@Van and irradiated with an NIR laser (808 nm, 2.5 W/cm^2 in 10 min) (Figures 18a and b).[102] After 7 days, the AuNSt@Van-treated and irradiated mice had wound areas reduced to 11.98%, while the wound areas of mice in other groups (untreated, Van treatment, and dark treatment) remained over 45%. These results demonstrated the healing of bacterial infectious wounds promoted by the AuNSt-based treatment. Additionally, these reductions in cancer cell viability and wound area are greater than those of traditional nanoparticles,[108,109] exhibiting the superior strength of the plasmonic nanostars in antibacterial treatments. Moreover, the antibacterial effect of the treatment was assessed by collecting the bacteria in the wounds of the mice, and the results (Figure 18c) showed a significant decrease in the numbers of bacterial colonies in the mice treated with AuNSt@Van, resulting in a bacterial survival rate of 5.26% (Figure 18d). Thus, the antibacterial agent designed and studied in this report highlights the potential of plasmonic nanostars in the development of high-selectivity and high-efficiency antibacterial therapies.

In addition to gold, Bessa et al. reported an investigation of the antibacterial properties of silver nanostar (AgNSt)-coated surfaces.[100] Specifically, AgNSts were uniformly coated onto glass surfaces and dried before being used for antibacterial tests. The silver atoms (Ag^0) in AgNSts, when oxidized, can leave the nanostars as Ag^+ cations, which can affect the cell membrane, membrane proteins, and DNA, leading to its antibacterial activity. The bactericidal effects of the AgNSt-coated surfaces were observable after 6 h of contact with the inoculated bacteria, *P. aeruginosa* and *S. aureus* (Figure 19). The bacteria deposited onto the AgNSt-coated surfaces were not able to replicate and were totally dead after 24 h. This work shows the potential of the much less studied silver plasmonic nanostars in the development

https://doi.org/10.1021/acsanm.2c02533
ACS Appl. Nano Mater. 2022, 5, 14051−14091

Table 5. Antibacterial Applications of Plasmonic Nanostars[a]

core NP	combinatory components	treatment target	antibacterial mechanism	level of study	key results	ref
AuNSt	rGO	MDR bacteria	photothermal lysis	in vitro	significantly enhanced inhibition and photothermal lysis of MRSA bacteria with high biocompatibility	97
AuNSt@PE	PSS, PDADMAC	gram (+) and gram (−) bacteria	chemo-photothermal effect	in vitro, in vivo	synergistic chemo-photothermal elimination of bacterial infection and promoted wound healing	98
AuNSt	CV dye	gram (+) and gram (−) bacteria	ROS generation	in vitro	great antimicrobial activity with 5 and 2.5 orders of magnitude enhancement regarding gram (+) and gram (−) bacteria, respectively	99
AgNSt	N/A	*P. aeruginosa*, *S. aureus*	silver antibacterial effect	in vitro	AgNSts showed greater potential for biocidal effects than when used in suspension	100
AuNSt	N/A	propionibacterium acnes	membrane destruction by AuNSt	in vitro	significant antibacterial effects against propionibacterium acnes	101
AuNSt	vancomycin	MRSA bacteria	photothermal effect	in vitro, in vivo	selective recognition and elimination of MRSA with satisfactory biocompatibility	102
AuNSt	thiol monolayer	planktonic bacteria	photothermal effect	in vitro	99.99% elimination of bacterial strains even after 3 months on the shelf	103
AuNSt, AgNP	PVA film	*E. coli*, *S. aureus*	photothermal effect	in vitro, clinical	on-demand, fast antibacterial action with 80−90% death of bacteria in contact with the AuNSt-containing film	104
AuNSt	PVA film	*S. aureus*	photothermal effect	in vitro	efficient bacterial eradication by photothermal effect under NIR irradiation	105
AuNSt	N/A	*S. aureus*	photothermal effect	in vitro	AuNSt monolayer efficiently induced cell death in *S. aureus* biofilms	106
AuNSt	N/A	*S. aureus*	morphological effect	in vitro	∼fourfold increase in antibacterial effect with no indication of cytotoxicity	107

[a]Abbreviations: rGO: reduced graphene oxide, MDR: multidrug-resistant, MRSA: methicillin-resistant *Staphylococcus aureus*, PE: polyelectrolyte, PSS: poly(sodium-*p*-styrenesulfonate), PDADMAC: poly(diallyldimethylammonium chloride), CV: crystal violet, ROS: reactive oxygen species, AgNSt: silver nanostar, N/A: not applicable, *P. aeruginosa*: *Pseudomonas aeruginosa*, *S. aureus*: *Staphylococcus aureus*, PVA: poly(vinyl alcohol), *E. coli*: *Escherichia coli*, and NIR: near-infrared.

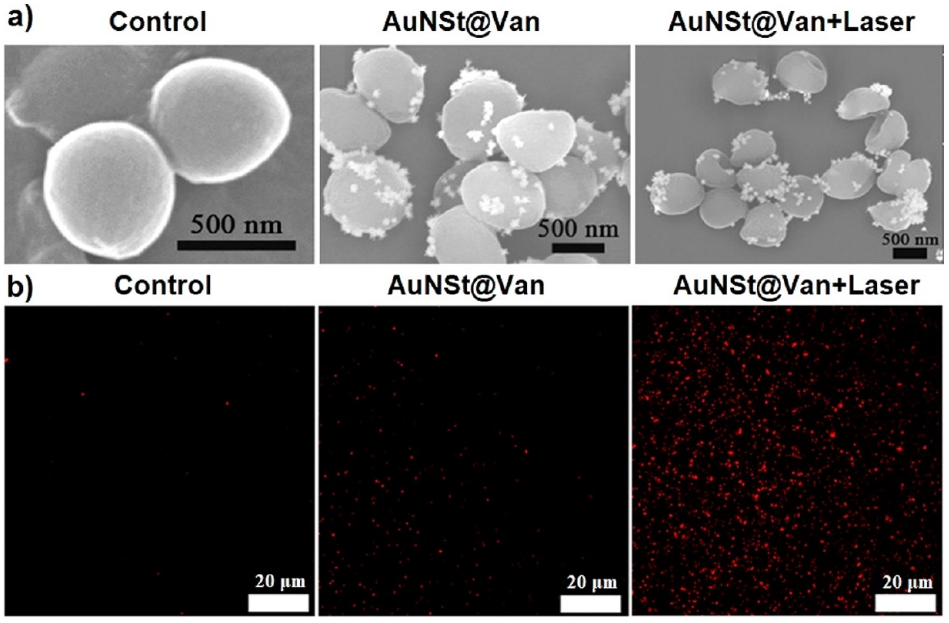

Figure 17. (a) Scanning electron microscopy images of MRSA untreated and treated with AuNSt@Van with and without NIR light irradiation. (b) Fluorescent images of MRSA stained by propidium iodide following various treatments. Adapted with permission from ref 102. Copyright 2019 American Chemical Society.

of effective and affordable platforms for antibacterial applications.

Various other reports on the antibacterial applications of plasmonic nanostars are summarized in Table 5. These studies used either bare nanostars[101,106] or nanostars in combination with other conjugates.[97−99] Most of the studies utilized the photothermal heating induced by the plasmonic nanostars under suitable electromagnetic irradiation as the antibacterial mechanism. These trends suggest the great potential of utilizing plasmonic nanostars, especially affordable AgNSts, for large-scale applications, such as the contact surfaces in hospitals or the glass panels of high-rise buildings.

3.1.5. Multifunctional and Theranostic Biomedical Applications of Plasmonic Nanostars. Conventional biomedical diagnostics and therapies mostly involve single modes, mechanisms, or applications, making medical procedures limited in efficacy and/or response time. The development of nanostructure-based technology has enabled the possibility of

https://doi.org/10.1021/acsanm.2c02533
ACS Appl. Nano Mater. 2022, 5, 14051−14091

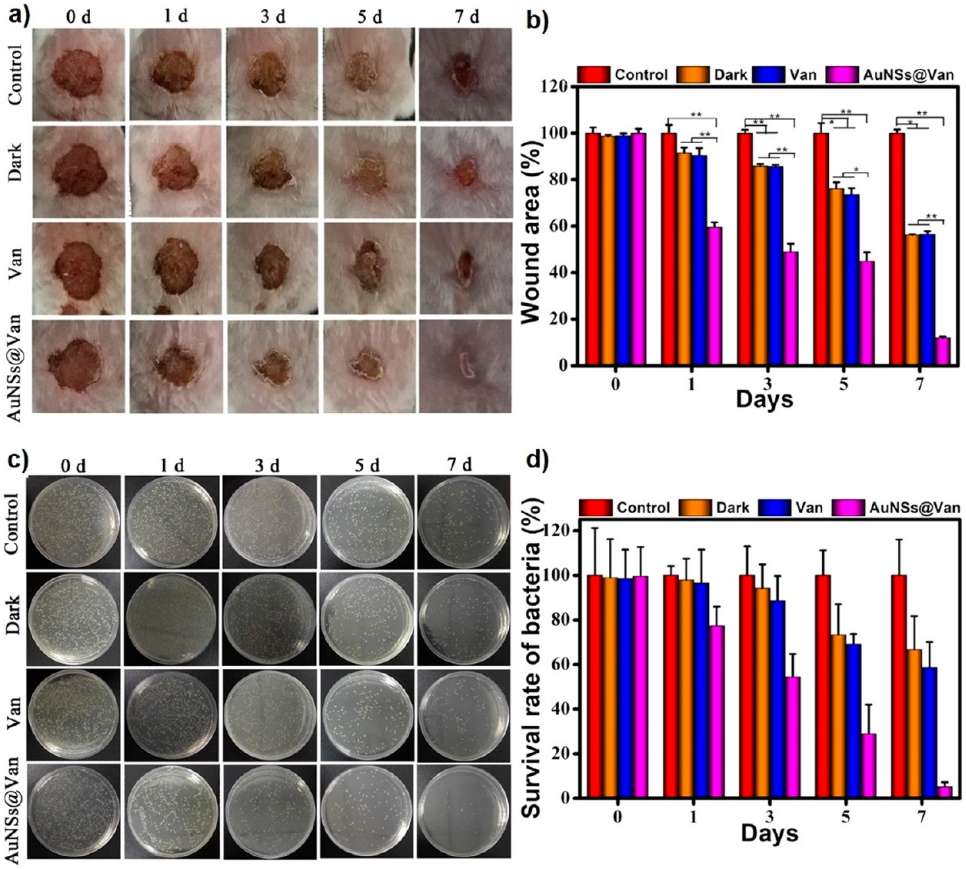

Figure 18. (a) Photographs and (b) corresponding wound areas from the four groups of infected mice under different treatments after 0, 1, 3, 5, and 7 days. (c) LB-agar plate images of surviving bacteria and (d) bacterial survival rates. Adapted with permission from ref 102. Copyright 2019 American Chemical Society.

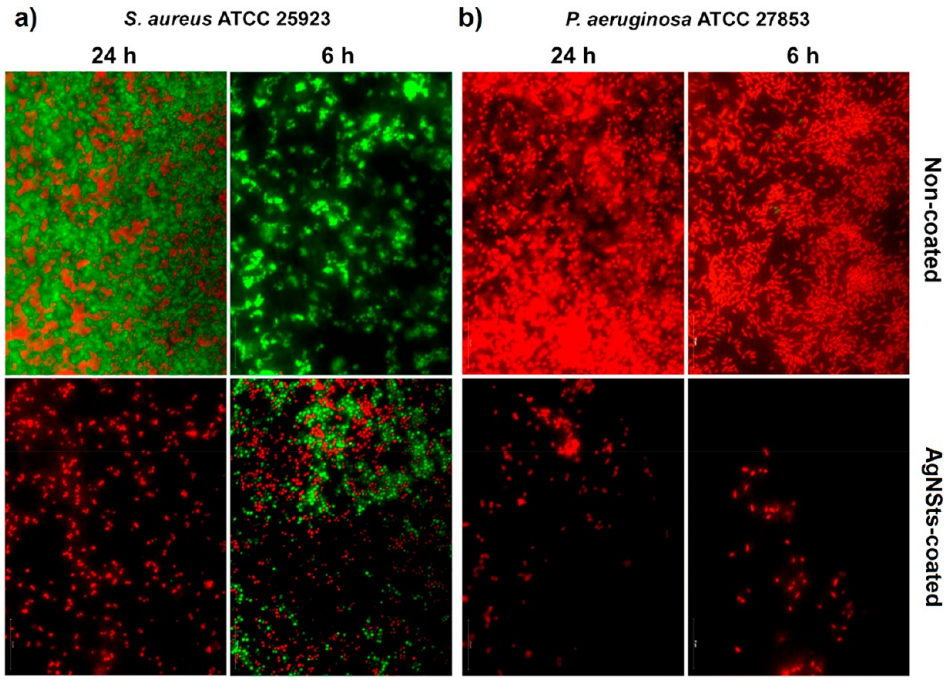

Figure 19. Staining images of (a) *S. aureus* ATCC 25923 and (b) *P. aeruginosa* ATCC 27853 bacteria deposited onto noncoated and AgNSt-coated surfaces for 6 and 24 h. Adapted with permission from ref 100. Copyright 2020 MDPI.

many different functions or multimodal applications on one nanoplatform.[62,110] Moreover, recent advances in these combinatory approaches, especially those based on plasmonic nanostructures, have allowed the collection of more in-depth

https://doi.org/10.1021/acsanm.2c02533
ACS Appl. Nano Mater. 2022, 5, 14051−14091

Table 6. Combined and Multifunctional Biomedical Applications of Plasmonic Nanostars[a]

core NP	combinatory components	target application	functions/ mechanisms	level of study	key results	ref
rGO-AuNSt	lipid bilayer membrane	pancreatic cancer-guided therapy	imaging-guided dual therapy	in vitro, in vivo	dual-modal imaging-guided synergistic therapy for pancreatic cancer therapy with negligible toxicity	112
AuNSt	ASON	tumor margin demarcation	fluorescent and photothermal	in vitro, in vivo	precise tumor delineation with high fluorescence contrast and outstanding spatial resolution for guided tumor resection	113
AuNSt@MOF	ZD2	breast cancer theranostics	MRI and photothermal	in vitro, in vivo	efficient MRI imaging and PTT for TNBC-visualized theranostics with molecular classification and good biocompatibility	114
GO/AuNSt	Ce6	cancer theranostics	PDT and PTT with fluorescence imaging	in vitro, in vivo	efficiently photoablated EMT6 tumor through guided synergistic PDT and PTT effect with excellent biocompatibility	115
SPION-AuNSt	TDF	drug delivery	magnetic and plasmonic	in vitro	multimodal quantitative imaging and image-guided drug delivery with tunable drug release capacity	116
AuNSt	fluorescent dye	tumor-targeting PTT	fluorescent and plasmonic	in vitro	demonstrated excellent photothermally induced cell apoptosis with precise assessment of efficacy by fluorescence imaging	117
AuNSt@SiO_2	DOX	cancer theranostics	photoacoustic imaging and chemo-PTT	in vitro, in vivo	targeted imaging and chemo-photothermal synergistic therapy of tumor at low cytotoxicity	118
AuNSt	IR820/DTX	prostate cancer theranostics	dual-mode imaging and PTT/PDT/ChT	in vitro, in vivo	dual-mode monitoring of tumor targeting and excellent antitumor effects by PTT/PDT/ChT synergistic strategy	119
AuNSt@SiO_2	FA	FR-targeted theranostics	SERS imaging and PDT	in vitro	FR-specific SERS detection and PDT	120
AuNSt	DOX	tumor-targeted theranostics	chemo- and thermotherapy	in vitro	fluorescence-based monitoring and PTT/ChT synergistic therapeutic efficiency together with targeted delivery of DOX	121
AuNSt	DOX	cancer theranostics	fluorescence-guided drug delivery	in vitro, in vivo	activatable visualization and controlled drug delivery for cancer therapy with good biocompatibility	122
SPION-AuNSt	Ce6	breast cancer-guided therapy	fluorescence imaging and PTT/PDT therapy	in vitro, in vivo	enhanced delivery efficiency and complete tumor growth suppression as well as trimodal imaging of tumors	123
AuNSt/Rh-6G	DNA aptamer	SARS-CoV-2	viral detection and inactivation	in vitro	rapid diagnosis of SARS-CoV-2 at 8 viruses/mL concentration and infection blocking	124
AuNSt	Cy5-DEVD	cancer treatment	fluorescence-guided PTT	in vitro, in vivo	cellular apoptotic induction by PTT with fluorescence monitoring	125
AuNSt	pHLIPs	tumor therapy	CT/PA-guided PTT	in vitro, in vivo	desirable targeting efficiency and significantly improved PTT efficacy with minimal effects on normal tissue and good biocompatibility	126
AuNSt-PDA	Ce6	breast cancer phototheranostics	PA imaging and PTT/PDT	in vitro, in vivo	enhanced PA imaging and PTT performance that completely eliminated tumors as well as inhibited lung metastasis	127
AuNSt	MRSA aptamer	antibacterial treatment	fluorescence imaging and PTT	in vitro, in vivo	MRSA bacteria-targeted imaging with high sensitivity and efficient PTT of diabetic wound and implanted bone infection	128
AuNSt	PDA	anticancer theranostics	multimodal imaging and PTT	in vitro, in vivo	precise guidance of multimodal imaging and homogeneous photothermal ablation of bulky solid tumors	129
AuNSt-MOF	DOX	cancer	dual-mode imaging and synergistic therapy	in vitro, in vivo	outstanding synergistic chemo-photothermal anticancer effect while enabling NIR thermal and PA imaging	130
AuNSt	FA	cancer theranostics	CT imaging and PTT/RT therapy	in vitro	excellent photothermal conversion, enhanced anticancer efficacy, and good biocompatibility	131
AuNSt	CD147/IR820	tumor theranostics	PA imaging and PTT/PDT therapy	in vitro, in vivo	significant suppression of tumor growth by PTT/PDT synergistic effect under PA guidance	132
AuNSt–Fe_3O_4	N/A	cancer theranostics	magnetic guidance and PTT	in vitro, in vivo	synergistic inhibition of tumor growth under magnetic guidance	133
AuNSt	dsDNA-DOX	MDR breast cancer therapy	chemotherapeutic and PTT	in vitro, in vivo	targeted delivery and controlled drug release with remarkable stability together with synergistic PTT to eliminate MDR tumor	134
AuNSt	albumin	L929, NIH 3T3, KB cells treatment	CT diagnostics and PTT	in vitro, clinical	substantial hyperthermia, CT contrast, and biocompatibility on three types of tested cells and human blood	135
AuNSt	anti-*H. pylori* antibody	*H. pylori* theranostics	PA imaging and PTT	in vivo	active targeting and killing of *H. pylori* in the stomach with orally administered nanoprobes	136
Fe_3O_4@AuNSt	N/A	tumor theranostics	CT, MRI, PA	in vitro, in vivo	remarkable PTT and PDT capacities without further modification together with multimodal in vivo imaging and excellent biocompatibility	137

[a]Abbreviations: AuNSt: gold nanostar, SPION: superparamagnetic iron oxide nanoparticle, TDF: tenofovir disoproxil fumarate, PTT: photothermal therapy, rGO: reduced graphene oxide, ASON: antisense oligonucleotide, MOF: metal–organic framework, TNBC: triple-negative breast cancer, ZD2: TNBC-targeted peptide, MRI: magnetic resonance imaging, GO: graphene oxide, Ce6: chlorin e6 photosensitizer, PDT: photodynamic therapy, EMT6: xenograft tumor, DOX: doxorubicin, ChT: chemotherapy, IR820: 820 nm near-infrared dye, DTX: docetaxel, FA: folic acid, FR: folate receptor, pHLIPs: pH (low) insertion peptides, CT: computed tomography, PDA: polydopamine, PA: photoacoustic, MRSA: methicillin-resistant *Staphylococcus aureus*, RT: radiotherapy, CD147: transmembrane glycoprotein, dsDNA: double-stranded DNA, MDR: multidrug-resistant, L929: mouse fibroblast, NIH 3T3: embryonic fibroblast, KB: oral epithelial carcinoma, and *H. pylori*: *Helicobacter pylori*.

medical information or guided therapies with better therapeutic performance and fewer side effects than traditional methods.[110,111] In the past decade, the development of plasmonic nanostars has made multifunctional medical theranostics even more effective, as summarized in Table 6.

In a recent report, Jia et al. fabricated AuNSt-based nanocarriers for the imaging-guided gene/photothermal syner-

https://doi.org/10.1021/acsanm.2c02533
ACS Appl. Nano Mater. 2022, 5, 14051−14091

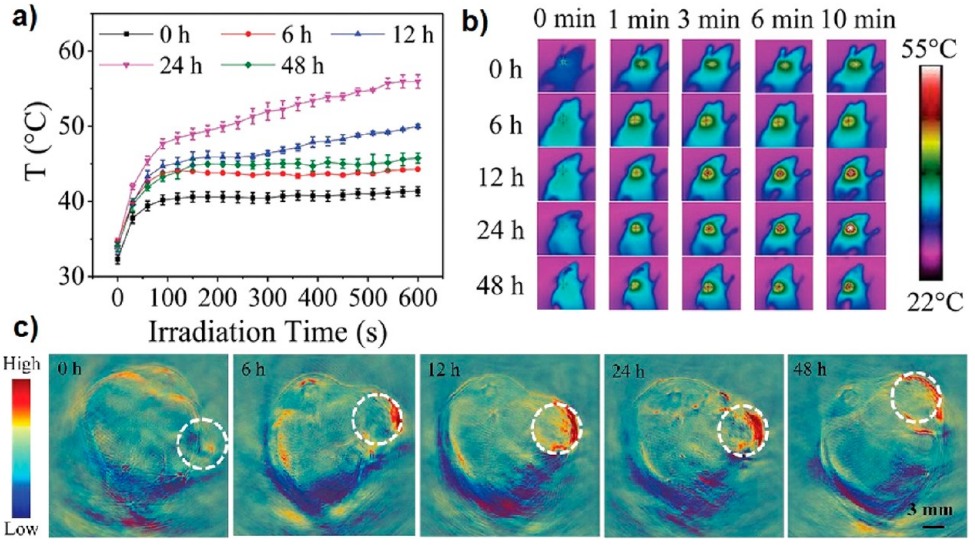

Figure 20. (a) Tumor temperature curves and (b) infrared thermal images acquired under 808 nm laser irradiation at a power density of 1.2 W/cm^2. (c) In vivo photoacoustic images of tumor regions taken at different time points. Adapted with permission from ref 112. Copyright 2020 Wiley.

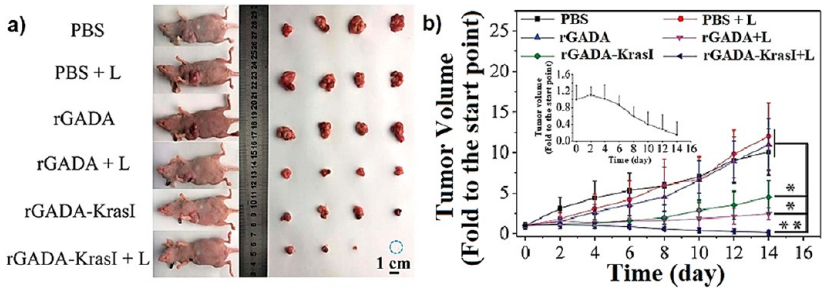

Figure 21. (a) Representative images of tumor-bearing nude mice and tumors after various treatments on day 14. (b) Relative tumor volumes (inset: enlarged curve of the rGADA-KrasI + L (laser) group) after treatment with various combinations of rGADA and KrasI with/without laser irradiation compared to those of the control group treated with PBS solution. Adapted with permission from ref 112. Copyright 2020 Wiley.

gistic therapy of pancreatic cancer.[112] The work combined both diagnosis and therapy on one platform, which can allow the recognition and specific binding of receptors on the surfaces of cancer cells. Specifically, the authors coated a positively charged lipid bilayer membrane on reduced graphene oxide@AuNSts (rGADAs) for selective tumor binding before activating dual-mode imaging with thermal (Figure 20b) or photoacoustics (Figure 20c). The temperatures at the tumor sites were increased to more than 55 °C for tumor ablations within 10 min using the photothermal heating property of AuNSts under laser irradiation (Figure 20a) at 24 h postinjection of rGADAs.

The rGADAs were also used to deliver a K-Ras gene plasmid (KrasI) for the pancreatic cancer gene and photothermal therapy.[112] The experimental results showed an excellent synergistic effect on the tumors that were virtually completely reduced after 14 days (Figure 21a), with the highest tumor growth inhibition rate of 98.5% in the gene/photothermal group (rGADA-KrasI + Laser) (Figure 21b). The lipid-coated platform was also found to be highly biocompatible. These results show not only the prospect of this platform in clinical applications of guided therapy for pancreatic cancer but also its potential adaptation to other cancers.

In another recently reported endeavor, Xue and co-workers used magnetic-plasmonic nanoheterostructures (MGNs) for multimodal imaging-guided photothermal and photodynamic therapy of triple-negative breast cancer (TNBC).[123] The star-shaped nanoheterostructures were coated with photosensitizer Ce6 to induce photothermal and photodynamic capabilities. The MGN@Ce6 nanostructures were then functionalized with cRGD (cyclo-Arg-Gly-Asp-D Phe-Lys) and TPP (4-carboxybutyl triphenylphosphonium) cationic molecules to form MGN@Ce6@RT nanocomplexes for the specific targeting of cancer cell membranes. The fluorescence imaging results in Figures 22a and b, the photoacoustic images in Figure 22c, and the thermal images in Figure 22d show that the functionalization with cRGD and TPP significantly enhanced the delivery efficiency of MGN@Ce6@RT in TNBC tumors. The multimodal imaging results also showed the capability of the AuNSt-based nanocomplex to enable tumor imaging with various mechanisms, expanding the utility and versatility of this technology.

The antitumor effects of synergistic photothermal/photodynamic therapy were evaluated in tumor-bearing mouse models with nanoheterostructure treatment under 5 min of laser exposure.[123] The results (Figures 23a and b) showed a remarkable inhibition of tumor growth, especially in mice treated with an intratumoral injection of MGN@Ce6@RT and 606 + 808 nm laser irradiation. There was a negligible variation in the average weights (Figure 23c) of the different groups of treated mice, implying the high biocompatibility of the AuNSt-based nanostructures. The results demonstrated in this work also highlight the potential of combining the biocompatible gold

https://doi.org/10.1021/acsanm.2c02533
ACS Appl. Nano Mater. 2022, 5, 14051−14091

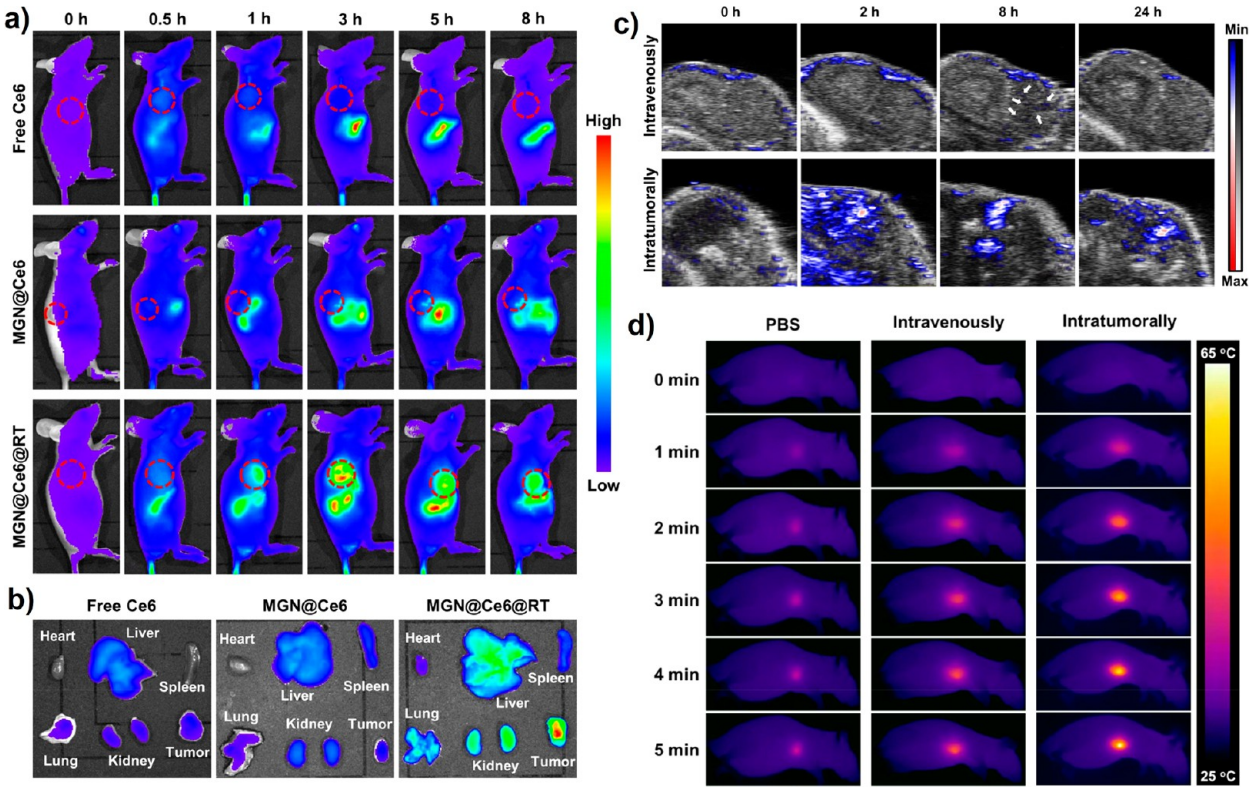

Figure 22. Fluorescent images of (a) mice at different times after intravenous injection of different formulations and (b) major organs and tumors collected from mice at 8 h postinjection. In vivo (c) photoacoustic images of tumor tissues and (d) thermal images of tumor-bearing mice at different times before and after intravenous and intratumoral injection of MGN@Ce6@RT. Adapted with permission from ref 123. Copyright 2021 Elsevier.

nanostars[44] and magnetic nanoparticles[138] for advanced biomedical applications.

The large numbers of recently reported studies on plasmonic nanostar-based multifunctional medical techniques, as summarized in Table 6, reflect the potential and attractiveness of this unique class of nanostructures in a one-stop approach for developing advanced guided therapy and/or theranostics for complex and detrimental diseases. Most of the reports understandably focused on the treatment of various types of cancer,[112,114,115,118] but diseases related to SARS-CoV-2[124] and bacteria[136] were also efficiently treated by these nanostar-based platforms, further highlighting the underexplored prospect of plasmonic nanostars in biomedical technology.

3.2. Sensing Applications of Plasmonic Nanostars. Plasmonic sensors have been well-known in the photonics and optics community for their extraordinary sensitivity resulting from the enhancement and localization of electromagnetic fields close to the interface of the metal nanostructures and a dielectric.[139] Plasmonic nanostructures have enabled new sensing platforms with much lower limits of detection on a wide range of sensing targets. In addition to their high surface area-to-volume ratios, an enhanced electromagnetic field has been a crucial factor in the success of plasmonic nanostructure-based sensors.[140] For plasmonic nanostars, both of these advantages are highly superior compared to other conventional plasmonic nanostructures (e.g., nanospheres, nanorods, nanocubes, nanoprisms, or nanocubes), endowing them with unique potential for allowing plasmonic sensing technologies to achieve even higher performances.

3.2.1. Sensing of Biological Analytes with Plasmonic Nanostars. Various noble metal nanostructures have been utilized for biosensing applications by exploiting their unique electronic and optical properties.[141] Their LSPR characteristics have enabled fast, real-time, and label-free probing for biologically relevant analytes, where the main challenges are detecting small particles and molecules at ultralow concentrations and fabricating compact devices for point-of-care analyses.[142] Many of the desirable plasmonic properties for biosensing, such as highly intensified local fields, large surface area-to-volume ratios, and superior numbers of hotspots, are highly characteristic of plasmonic nanostars, making them attractive for research efforts in biosensing, as summarized in Table 7 below.

Rapid, sensitive, and on-site detection are critical in any effective response against regional epidemics or global pandemics, such as the COVID-19 pandemic, which has been disrupting the world over the last two years. In a recent report, Srivastav et al. demonstrated a rapid and sensitive lateral flow assay (LFA) based on surface-enhanced Raman scattering (SERS) for SARS-CoV-2 biosensing.[156] The biosensor was based on AuNSts labeled with an NIR dye as Raman reporters and was able to detect SARS-SoV-2-specific IgG and IgM antibodies, as illustrated in Figure 24. The AuNSts were functionalized with mouse antihuman IgM and antihuman IgG secondary antibodies for IgM and IgG antibody targeting, respectively.

The AuNSt-based LFA test was able to facilitate the detection of both SARS-CoV-2-specific IgM and IgG antibodies in COVID-19-infected patient sera up to 4 months after the infection, as shown in Figure 25a.[156] The authors observed a clear decline in the IgM signal in comparison to the signal of IgG, which is consistent with the reporting of previous studies that SARS-CoV-2-specific IgG antibodies remain much longer in the sera of infected patients compared to IgM antibodies. Utilizing

https://doi.org/10.1021/acsanm.2c02533
ACS Appl. Nano Mater. 2022, 5, 14051−14091

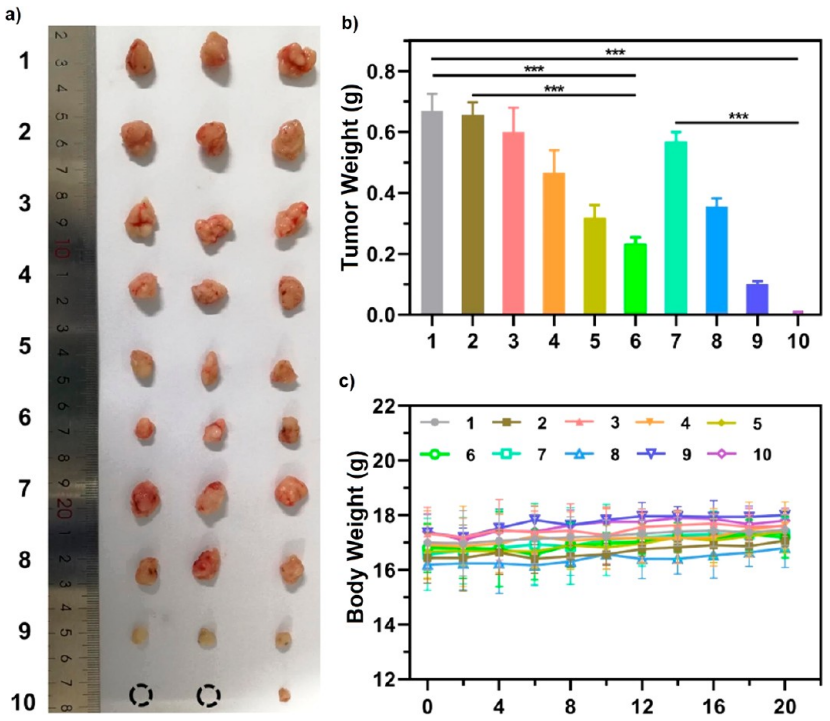

Figure 23. (a) Photographs of the sacrificed tumor tissues after various treatments (***$P < 0.001$). (b) Average tumor weight after various treatments. (c) Average body weight variations during the treatment period. Note that 1−10 represent mouse groups with different treatments: (1) intravenous injection of PBS; (2) intravenous injection of PBS and 660 + 808 nm laser irradiation; (3) intravenous injection of MGN@Ce6@RT; (4) intravenous injection of MGN@Ce6@RT and 660 nm laser irradiation; (5) intravenous injection of MGN@Ce6@RT and 808 nm laser irradiation; (6) intravenous injection of MGN@Ce6@RT and 660 + 808 nm laser irradiation; (7) intratumoral injection of MGN@Ce6@RT; (8) intratumoral injection of MGN@Ce6@RT and 660 nm laser irradiation; (9) intratumoral injection of MGN@Ce6@RT and 808 nm laser irradiation; and (10) intratumoral injection of MGN@Ce6@RT and 660 + 808 nm laser irradiation. Adapted with permission from ref 123. Copyright 2021 Elsevier.

the high IgM signal in the early period after the infection, the authors investigated the limit of detection (LOD) of this AuNSt-based biosensor. The result demonstrated an LOD as low as 100 fg/mL (as displayed in Figure 25c), which is 7 orders of magnitude better than the ∼1 μg/mL of the naked eye detection (Figure 25b). The authors estimated that the sensitivity of this method is at least 10 times higher than that of conventional LFAs, highlighting the vast potential of AuNSt-based biosensors with ultralow LODs.

The severe impacts of cancer on human life have always been great motivation for the development of early and more efficient diagnostic methods. In a recent study,[145] Fabris and co-workers described a novel biosensor for the detection and quantification of the cancer biomarker epithelial cell adhesion molecule (EpCAM) at the single-cell level. The biosensor leveraged the field-enhancing characteristic of AuNSts together with improved recognition and capture for MCF-7 and PC-3 cancer cells, which were enabled by functionalization with EpCAM aptamer molecules, as illustrated in Figure 26.

The plasmonic biosensor generated detectable SERS signals for soluble EpCAM at a detection limit of 10 pM (Figure 27a), which showed that the designed sensors could effectively detect soluble proteins.[145] With the same sensing substrate, by using the correlation between the number of EpCAM molecules per μm^2 and the SERS intensity at 1076 cm^{-1} (Figure 27b), it was feasible to identify and quantify biomarker expression at the single-cell level (Figures 27b and c). This single-cell level detection is a significant advancement from the thousand-cell level detection attained using gold nanoparticles[164] or nanorods[165] counterparts. This single-cell level quantification enabled discernment among cells carrying phenotype expression levels, allowing early cancer detection or monitoring of the onset of metastasis. These results demonstrate the strength of AuNSts in plasmon-enabled signal enhancement based on the large numbers of hotspots present in their structures.

In addition to the detection of SARS-CoV-2[161−163] and cancer biomarkers,[149,159] many other studies also reported the development of various AuNSt-based biosensors for the detection of bacteria,[146] antibiotics,[143] cortisol,[160] mRNA,[154] or nucleic acids,[155] as summarized in Table 7. The wide range of biological analytes detected by these AuNSt-enabled sensing platforms is indicative of the advantages and versatility of plasmonic nanostars.

3.2.2. Sensing of Other Analytes Based on Plasmonic Nanostars. In addition to the sensing of biological analytes for medical applications, many other analytes also require sensitive and efficient sensing methods for commercial and industrial uses. For this purpose, plasmonic nanostructures have also been demonstrated to be highly sensitive and efficient in the development of advanced sensors.[166] Because these sensors exploit the plasmonic characteristics of those metal nanostructures,[166] nanostars can be expected to greatly amplify the performance of plasmonic sensors with their superior field enhancements and surface areas. Recent works on plasmonic nanostar-based sensors for the detection of nonbiological analytes are summarized in Table 8.

The presence of heavy metal ions in water has always been a critical, long-term threat to the well-being of humans and the environment worldwide owing to its association with health problems, such as cancers, skin lesions, cardiovascular diseases,

https://doi.org/10.1021/acsanm.2c02533
ACS Appl. Nano Mater. 2022, 5, 14051−14091

Table 7. Biosensing Applications of Plasmonic Nanostars[a]

core NP	combinatory components	detection target	sensing mechanism	key results	ref
AuNSt	antiTC antibody	tetracycline antibiotic	SPR	AuNSt improved the LOD by 3 orders of magnitude to 10 aM concentration with good selectivity in environmental samples	143
AuNSt	biotinylated thiol	PSA	RI sensing	biosensor demonstrated detecting capability at 10^{-17} M concentration of PSA in serum	144
AuNSt	EpCAM aptamer	cancer biomarker	SERS	nonlabel detection of EpCAM with single-cell detection for soluble protein	145
AuNSt	CRO	*E. coli*	SERS	displayed significantly reduced detection time of biomarker produced by *E. coli* especially at the 1358 cm^{-1} peak	146
AuNSt	SCARB2	EV71	SERS	EV71 detected in protein-rich sample within 15 min without the need for temperature-controlled sample incubation	147
AuNSt	N/A	alkaline phosphatase	photothermal immunoassay	large blue shift in the LSPR frequency by silver deposition on the AuNSt triggered by alkaline phophatase and accompanied by a change in photothermal conversion efficiency	148
AuNSt	BSA-Kem	PKA cancer biomarker	SERS	identified two Raman peaks at 725 and 1395 cm^{-1} to distinguish MDA-MB-231 and MCF-7 breast cancer cells that overexpress PKA	149
AuNSt and others	N/A	DNA mutation	SERS	AuNSt showed the highest SERS activity with sensitive, direct, and rapid identification of DNA mutation in combination with PCR	150
AuNSt	α-ZIKV NS1, α-DENV NS1	Zika and dengue viruses	SERS-based immunoassay	15-fold and 7-fold lower LODs for Zika and dengue viruses, respectively	151
AuNSt	COFs	β-lactoglobulin	SERS immunoassay	LOD of 0.01 ng/mL with a linear range from 25.65 to 6.2×10^4 ng/mL by a low-cost, higher-recovery, and lower-cross-reactivity method	152
AuNSt@ SiO_2	Raman reporter	CEA	SERS	detected CEA in 30 μL of whole blood at an LOD of 1 ng/mL with a portable, disposable, point-of-care test method	153
AuNSt	Raman label	breast cancer miRNA	SERS	successfully detected short miRNA from real biological cancer sample displaying multiplexed detection capability	154
AuNSt@ Ag	iMS	nucleic acids	SERS	AuNSt−optical fiber combination enabled direct detection of miRNA in plant tissue extract without complex assays	155
AuNSt	antihuman IgM, antihuman IgG	SARS-CoV-2	SERS-LFA	SARS-CoV-2 biomarkers detected in COVID-19 serum with at least 10-times higher sensitivity than conventional LFA	156
AuNSt@ SiO_2	MIP	ENRO	SERS assay	analytical performance yielded an LOD of 1.5 nM for 10 min of incubation with limited cross-reactivity	157
AuNSt	GO	serum bilirubin	SERS	label-free detection of bilirubin in blood serum with two linear ranges of 5−150 and 150−500 μM together with an LOD of 0.436 μM	158
AuNSt-TiO_2	Raman reporter	leukemia	SERS	enhanced Raman response indicating chemotherapeutic effects	159
AuNSt	cortisol antibodies	cortisol	SERS immunoassay	AuNSt exhibited great SERS response in a faster and more reproducible immunoassay of biological fluid	160
AuNSt	GO	SARS-CoV-2	electrochemical response	displayed an LOD of 1.68×10^{-22} μg/mL and a sensitivity of 0.0048 μA μg/mL cm^2 toward SARS-CoV-2 biological media	161
AuCuNSt	N/A	SARS-CoV-2	SERS	consistent SERS signal for SARS-CoV-2 virion particles with well-defined spectra for viral detection	162
AuNSt	activated GO	SARS-CoV-2	electrochemical sensing	label-free detection of SARS-CoV-2 S1 protein in the blood samples of infected patients in 1 min with an LOD of 0.18×10^{-19} %V/V	163

[a]Abbreviations: antiTC: antitetracycline, SPR: surface plasmon resonance, LOD: limit of detection, RI: refractive index, PSA: prostate-specific antigen, EpCAM: epithelial cell adhesion molecule, SERS: surface-enhanced Raman spectroscopy, CRO: β-lactam antibiotic ceftriaxone, *E. coli*: *Escherichia coli*, EV71: enterovirus 71, SCARB2: recombinant scavenger receptor class B, N/A: not applicable, BSA-Kem: bovine serum albumin-kemptide, PKA: protein kinase A, MDA-MB-231: human breast adenocarbinoma cell, MCF-7: human breast adenocarbinoma cell, PCR: polymerase chain reaction, ZIKV: Zika virus, DENV: dengue virus, NS1: nonstructural protein 1, COFs: covalent organic frameworks, CEA: carcinoembryonic antigen, miRNA: microRNA, iMS: inverse molecular sentinel, SARS-CoV-2: severe acute respiratory syndrome coronavirus 2, LFA: lateral flow assay, IgG: immunoglobulin G, COVID-19: coronavirus disease 2019, MIP: molecularly imprinted polymer, ENRO: enrofloxacin, GO: graphene oxide, AuCuNSt: gold copper nanostar, and Rh-6G: rhodamine.

and neurological disorders.[190,191] Thus, it is extremely important to develop sensitive, reliable, and cost-effective methods for identifying and quantifying these ions in water. In a recent report,[175] Dutta et al. developed electrochemical sensors based on AuNSts for the detection of As(III), Hg(II), and Pb(II) ions in drinking water. The authors prepared and drop-casted AuNSts onto the carbon paste screen-printed electrodes (CPSPEs) of electrochemical sensors. The AuNSt-based sensors were tested for electrical responses to As(III), Hg(II), and Pb(II) ions in water under a wide range of concentrations, and the results are presented in Figure 28. The LODs were 0.8, 0.5, and 4.3 ppb for As(III), Hg(II), and Pb(II) ions, respectively. These LODs were significantly lower than those achieved by counterpart sensors with conventional plasmonic nanostructures for all targeted As(III),[192,193] Hg(II),[194,195] and Pb(II) ions.[196] The limits of quantification (LOQs) for the As(III), Hg(II), and Pb(II) ions were identified as 2.5, 1.5, and 13 ppb with linear ranges of 2.5−764.2, 1.5−538.9, and 13−323.6 ppb, respectively.

This work also investigated the utility of AuNSt-based CPSPE sensors for the detection of all three analytes in the same solution.[175] The results revealed LODs of 3.57, 11.08, and 20.55 for As(III), Hg(II), and Pb(II) ions, respectively, as well as LOQs of 10.83, 33.59, and 62.26 with linear ranges of 10.8−419.4, 33.6−361.5, and 62.3-215.6 ppb (Figure 29). These

https://doi.org/10.1021/acsanm.2c02533
ACS Appl. Nano Mater. 2022, 5, 14051−14091

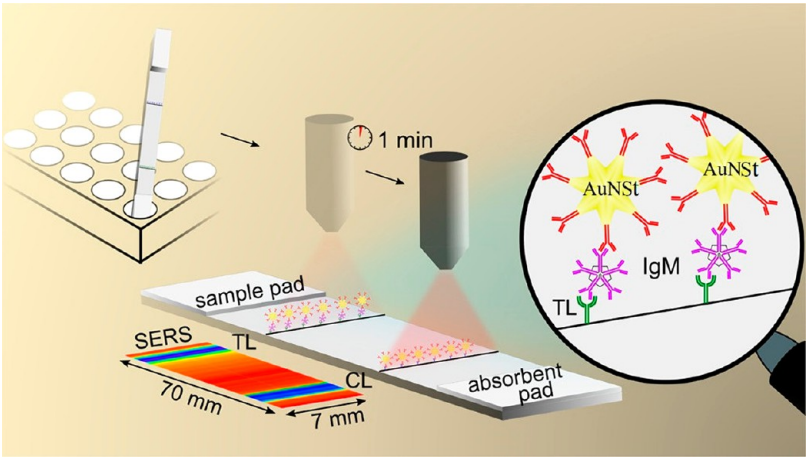

Figure 24. Schematics of the SERS-based LFA platform for SARS-CoV-2 IgM detection. TL: test line, CL: control line, and AuNSt: gold nanostar. Reproduced with permission from ref 156. Copyright 2021 American Chemical Society.

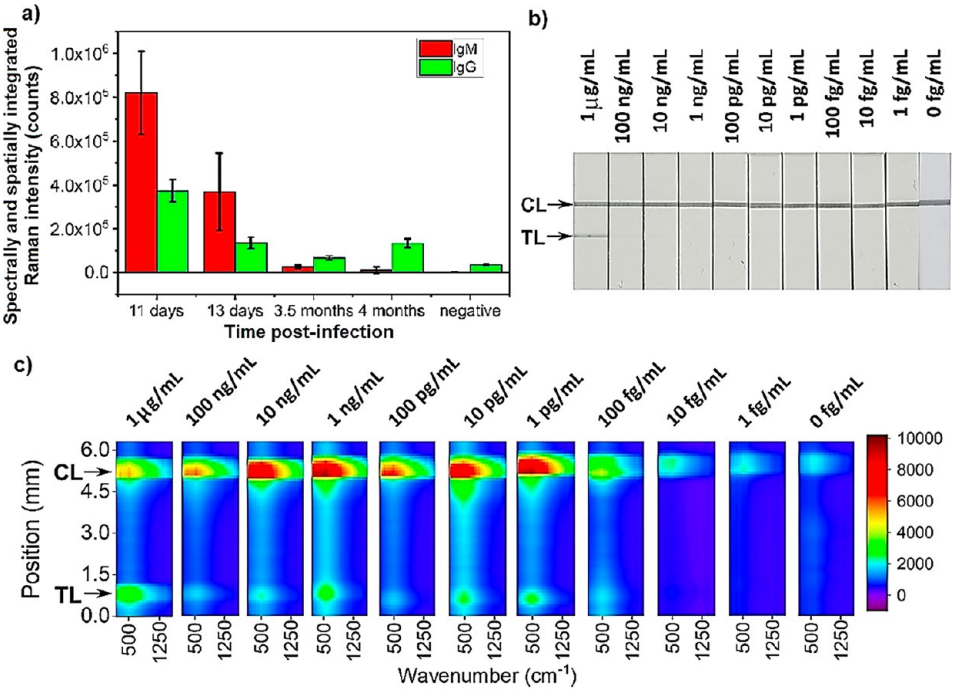

Figure 25. (a) Comparison of SARS-CoV-2-specific IgM and IgG antibody expression on AuNSt-based LFA strips. (b) Photograph of the test strips after the assay. (c) SERS-based false-color images of the areas between the sample pads and the absorbent pads on the LFA strips. Adapted with permission from ref 156. Copyright 2021 American Chemical Society.

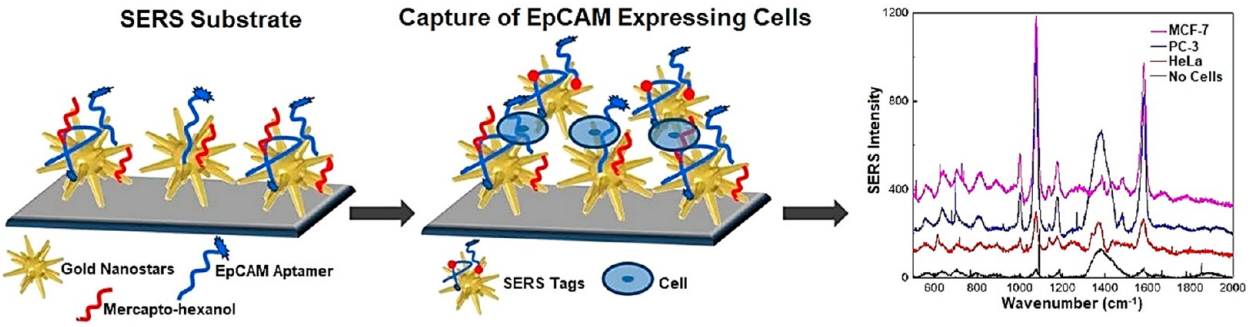

Figure 26. Schematics of AuNSt-based biosensors used to recognize and capture cancer cells and generate SERS signals. Reproduced with permission from ref 145. Copyright 2018 American Chemical Society.

https://doi.org/10.1021/acsanm.2c02533
ACS Appl. Nano Mater. 2022, 5, 14051−14091

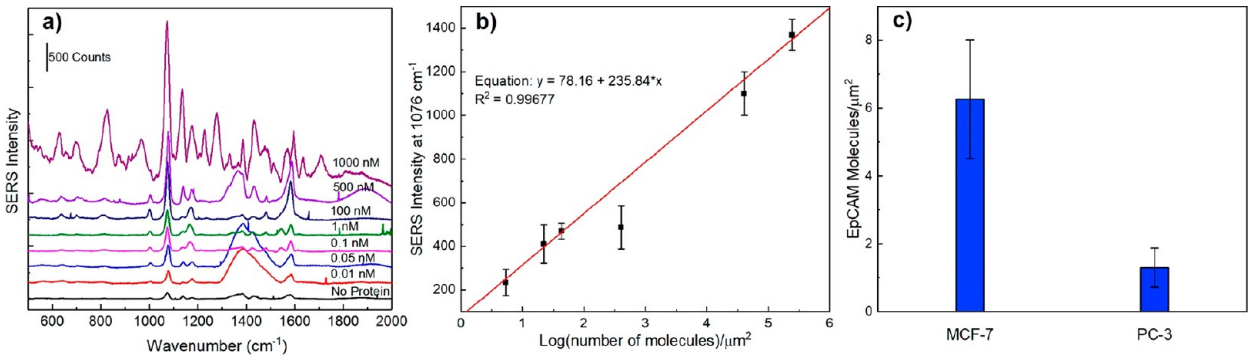

Figure 27. (a) SERS spectra generated by the AuNSt-based biosensor for protein capture carried out with increasing concentrations of 17-bp EpCAM aptamers. (b) Linear correlation between the log of the number of EpCAM molecules found per μm^2 area at different protein concentrations and their SERS response at 1076 cm^{-1} and (c) the calculated number of EpCAM molecules present per μm^2 area on MCF-7 and PC-3 cancer cells. Adapted with permission from ref 145. Copyright 2018 American Chemical Society.

results indicate the multianalyte detection capability of the AuNSt-based sensor.

The widespread use of pesticides in agricultural activities is a serious concern for human health and the environment, thus necessitating efficient corresponding detection methods. Lin and co-workers reported a fluorescent aptamer-based lateral flow sensor integrated with fluorophore-quencher nanopairs and a smartphone spectrum reader for achieving triple-target detection of chlorpyrifos, diazinon, and malathion insecticides.[178] The authors used aptamers instead of antibodies as recognition elements for better specificity and stability. AuNSts and quantum dot (QD) nanobeads were used to form fluorophore-quencher nanopairs for emitting fluorescence signals in the presence of the targeted pesticides (Figure 30).

After optimization, the sensors were tested in the presence of different concentrations of the target pesticides from 100 pg/mL to 100 μg/mL.[178] The data showed obvious and continuous increases in the intensities of the yellow and red zones when the target concentrations increased (Figure 31a). With increasing target concentration, clear maxima near a 610 nm wavelength emerged for all three types of pesticides (Figure 31b). By plotting the target peak area at ~610 nm vs the log of the concentration, the authors obtained the standard curves shown in Figure 31c and determined LODs of 0.73, 6.7, and 0.74 ng/mL for chlorpyrifos, diazinon, and malathion, respectively. These LODs are lower than the results reported for other sensing platforms based on conventional plasmonic nanostructures for all three pesticides, chlorpyrifos,[197,198] diazinon,[199] and malathion.[200,201] The portable sensing platform described in this study, with its high sensitivity and reliability, might be suitable for on-site applications of multipesticide quantification.

AuNSts were also used to develop sensors for detecting and quantifying various other harmful analytes, from bisphenol A (BPA)[176] and clenbuterol[189] to the uranyl cation[182,187] in radioactive waste, as summarized in Table 8. These studies further highlighted the high performance and versatility of AuNSt-based sensors for the detection, quantification, and monitorization of many nonbioanalytes, which are harmful and toxic to human health and the environment.

3.3. Imaging Applications of Plasmonic Nanostars.

Imaging is a powerful tool for different applications in modern life, especially in biomedical fields. The development of plasmonic nanotechnology has significantly advanced imaging methods with the use of plasmonic nanoparticles as optically stable bioimaging agents.[202] Thus, plasmonic nanostars are promising platforms for advanced imaging applications. Table 9 lists recently reported works based on plasmonic nanostars for imaging.

In an effort to develop better imaging techniques for brain tumor diagnostics, Neuschmelting et al. used silica-coated AuNSts as a contrast agent for a noninvasive dual-modality depiction of glioblastoma (GBM), the deadliest and most common primary brain cancer.[217] The AuNSt@SiO_2 probes were injected intravenously in a mouse model and capable of sending enhanced multispectral optoacoustic tomography (MSOT) signals only 1 min postinjection (Figure 32a). The MSOT signals were significantly increased (Figure 32b) and lasted for at least several hours postinjection (Figure 32c).

Notably, the AuNSt-based contrast agent was able to produce both MSOT (Figure 33a) and surface-enhanced resonance Raman scattering (SERRS) (Figure 33b) in vivo imaging of brain tumors in mouse models with high signal sensitivity and specificity.[217] The MSOT imaging also accurately and three-dimensionally depicted GBMs with high specificity, as shown in Figure 33c. A high penetration depth of several millimeters and real-time imaging also made MSOT an ideal complementary method to the highly sensitive and specific but more time-consuming and depth-limited SERRS imaging. Additionally, no adverse effects were recorded over the period of 14 h postinjection in any of the mice. The results reported in this work paved the way for a dual-mode noninvasive in vivo imaging method for brain tumors with high sensitivity and high specificity in a much less time-consuming procedure.

In another work, Paulus and co-workers developed a AuNSt-based technique for the visualization of microvasculature using both photoacoustic microscopy (PAM) and optical coherence tomography (OCT).[206] AuNSts functionalized with arginine−glycine−aspartic acid (RGD) peptides were used as multimodal contrast agents for both PAM and OCT in vivo imaging, as illustrated in Figure 34. The good biocompatibility of the functionalized AuNSt contrast agents was confirmed by flow cytometry analysis and an MTT assay using HeLa cells. The modified AuNSts were then tested in rabbit models for their performance as contrast agents for both PAM and OCT in vivo imaging.

The PAM image showed choroidal neovascularization (CNV) in the rabbit models with great contrast, as shown in the 3D photoacoustic volumetric visualization (Figure 35a), and maximum intensity projection PAM images could be obtained for the selected region of interest (Figures 35b and c).[206] The

https://doi.org/10.1021/acsanm.2c02533
ACS Appl. Nano Mater. 2022, 5, 14051−14091

Table 8. Nonbiological Sensing Applications of Plasmonic Nanostars[a]

core NP	combinatory components	detection target	sensing mechanism	key results	ref
AuNSt	polyaniline	ammonia gas	electrical conductivity	sevenfold increase in sensitivity toward ammonia gas detection compared to pure polyaniline	167
AuNSt	pNIPAM	pyrene gas	SERS	demonstrated efficient trapping for gas phase pollutant pyrene	168
AuNSt	Cy3-cDNA	hepatotoxin	SERS, fluorescence	achieved high sensitivity and selectivity toward hepatotoxin MC-LR in real water samples with high accuracy and reproducibility	169
AuNSt	4-mercaptobenzoic acid	pH	SERS	pH sensing with high reproducibility and stability in a linear range of 6.5−9.5 for quantifying the pH_i and pH_e of breast cancer cells	170
AuN@SiO_2	antibody-SERS tag	MC-LR toxin	SERS immunosensing	SERS-based detection of MC-LR toxin at an LOD of 0.014 μg/L with a linear dynamic detection range of 0.01−100 μg/L	171
AuNSt	N/A	gaseous metabolites	SERS	high sensitivity, reproducibility, and stability toward the gaseous metabolites of foodborne bacteria such as *E. coli*, *E. aureus*, and *P. aeruginosa*	172
AuNSt	N/A	Cu(II) ions	chemiluminescence	first use of AuNSt in CTC; remarkably enhanced the CTC signal with an LOD of 0.9 nM and a linear calibration range of 2 nM−9 μM for environmental and biological samples	173
AuNSt-GQD	glutamic acid	insecticide	electrochemical response	ultrahigh sensitivity and selectivity for the detection of acetamiprid with an LOD of 0.37 fM and a linear range of $1-10^5$ fM	174
AuNSt, AuNP	N/A	As(III), Hg(II), and Pb(II) ions	electrochemical response	AuNSt displayed a higher sensing performance for detecting heavy metal ions than AuNP with LODs of 0.8, 0.5, and 4.3 ppb for As(III), Hg(II) and Pb(II) ions, respectively.	175
AuNSt	4-aminothiophenol	BPA	SERS-LFA	SERS LOD 20- and 205-times more sensitive than color and visual intensity, respectively	176
AgNSt	AuNP, 1LG	Rh-6G	SERS	137-fold enhancement in Raman response and an LOD of 0.1 pM as well as simultaneous detection of Rh-6G and MB	177
AuNSt	aptamer	multipesticides	fluorescence	LODs of 0.73, 6.7, and 0.74 ng/mL for chlorpyrifos, diazinon, and malathion, respectively, in a multiplexed manner with a portable, smartphone-enabled platform	178
AuNSt	2-mercaptoethanol	Pb^{2+}	colorimetric method	detected Pb^{2+} ions with an LOD of 1.5 pM over the tested interfering Cu^{2+} ions in water samples	179
AuNSt	PEG	Hg^{2+}	SERS	successfully detected Hg^{2+} with an LOD of 0.2 ppb in water and coastal seawater samples	180
AgNSt	N/A	Rh-6G	SERS	detected Rh-6G with an LOD of 11.4 pg at an analytical enhancement factor of $\sim 10^7$	181
AuNSt	AO-PAN	uranyl cation	SERS	reproducible sorption and detection of uranyl in real-world samples without the need for radioactive tracer and extensive sample pretreatment steps	182
AuNSt	N/A	MG	SERS	effective control of AuNSt's morphology for enhanced detection of MG at nanomolar concentrations	183
AuNSt	L-cysteine	Cu^{2+} ion	SERS	practical LOD of 10 μM Cu^{2+} with remarkable selectivity	184
AuAgNSt	N/A	Rh-6G	SERS	extremely large enhancement factor of 4×10^{10} together with excellent control of hotspot location, homogeneity, and biocompatibility	185
AuNSt	PDMS substrate	benzenethiol	SERS	enhancement factor of 1.9×10^8 even under 100 cycles of physical stimuli	186
AuNSt	AO-PAN film	uranyl cation	LSPR, SERS	detected uranyl with a linear range of ∼0.3−3.4 μg uranyl/mg polymer and quantified the Gibbs free energy of the uranyl−carboxylate interaction as 8.4 ± 0.2 kcal/mol	187
AuNSt	DNA origami	TR dye	SERS	achieved a SERS enhancement factor of up to 8×10^9 for single-analyte detection with tunable interparticle gap and controlled stoichiometry	188
Au@AuNSt	anti-CL antibody	clenbuterol	colorimetric/SERS-LFA	dual-mode highly sensitive detection of clenbuterol with a visual LOD of 5 ng/mL and SERS LOD of 0.05 ng/mL	189

[a]Abbreviations: pNIPAM: poly-*N*-isopropylacrylamide, SERS: surface-enhanced Raman spectroscopy, Cy3-cDNA: cyanine dye-modified complementary DNA, MC-LR: microcystin-LR, pH_i: intracellular pH, pH_e: extracellular pH, N/A: not applicable, *E. coli*: *Escherichia coli*, *S. aureus*: *Staphylococcus aureus*, and *P. aeruginosa*: *Pseudomonas aeruginosa*, CTC: computed tomography of chemiluminescence, LOD: limit of detection, GQD: graphene quantum dot, AuNP: gold nanoparticle, BPA: bisphenol A, LFA: lateral flow assay, 1LG: monolayer graphene, Rh-6G: rhodamine 6G, MB: methylene blue, PEG: poly(ethylene glycol), AuAgNSt: gold−silver nanostar, MG: malachite green, LSPR: localized surface plasmon resonance, AO-PAN: amidoximated polyacrylonitrile, TR: Texas red, and anti-CL: anticlenbuterol.

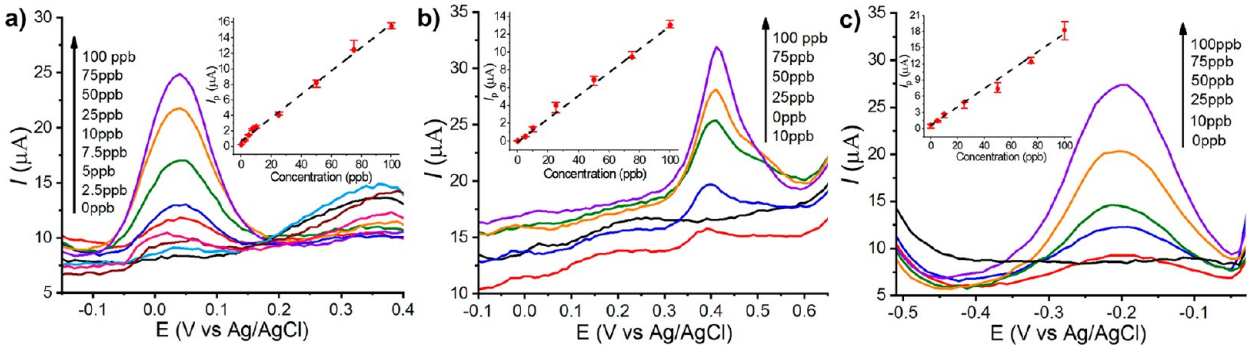

Figure 28. Calibration plots of (a) As(III), (b) Hg(II), and (c) Pb(II) ions in 0.1 M HCl on AuNSt-modified CPSPEs at different analyte concentrations. Insets: linear regression models applied to each data plot. Adapted with permission from ref 175. Copyright 2019 Elsevier.

https://doi.org/10.1021/acsanm.2c02533
ACS Appl. Nano Mater. 2022, 5, 14051−14091

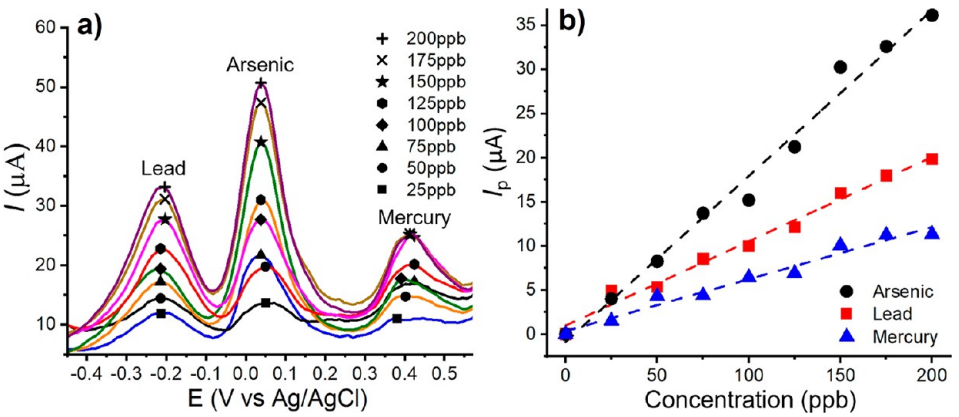

Figure 29. (a) Electrical response of the AuNSt-based CPSPE sensor for multianalyte detection of Pb(II), As(III), and Hg(II) ions over the concentration range of 0−200 ppb in 0.1 M HCl and (b) the corresponding linear calibration plots of peak heights vs concentrations of three heavy metal ions. Adapted with permission from ref 175. Copyright 2019 Elsevier.

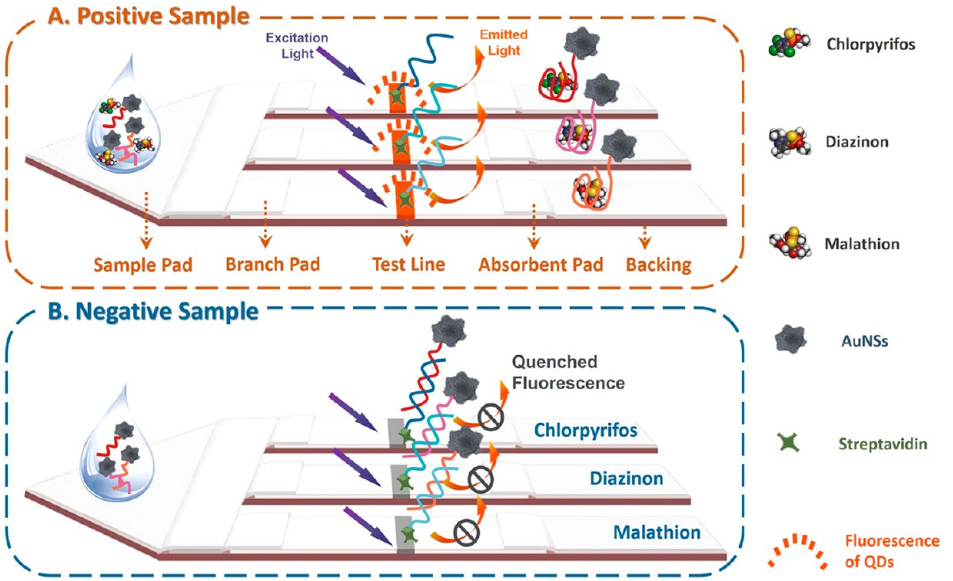

Figure 30. Schematics of a fluorescent aptamer-based lateral flow sensor in positive and negative samples. Adapted with permission from ref 178. Copyright 2018 Elsevier.

retinal vascular network was clearly observed in PAM images obtained at 578 nm. Great discrimination between CNV and hemoglobin was achieved by imaging at a longer wavelength of 650 nm because of the low optical absorption of hemoglobin at 650 nm. In addition to PAM imaging, OCT-based visualization was also demonstrated with the same conjugated AuNSt contrast agent. After injection of the AuNSts contract agent, CNV was clearly observed with a greater OCT contrast (Figure 35e) due to increased backscattering from the AuNSts compared to the preinjection image (Figure 35d), thus demonstrating the signal-enhancing capability of AuNSts for OCT imaging.

In addition to these representative works, Table 9 also summarizes many other studies that used AuNSts to enhance imaging techniques with various imaging targets and signal-transducing mechanisms. They span from the imaging of HeLa cells by enhanced fluorescence[213] to alveolar basal epithelial cells by computed tomography[211] and tumor cells by immuno-positron emission tomography.[207] The wide range of signal-transducing mechanisms enhanced by plasmonic nanostars demonstrates the strength and versatility of this type of nanostructure for enhancing signals based on their great plasmonic properties.

3.4. Catalytic Applications of Plasmonic Nanostars.

Catalysis plays an important role in industry as well as everyday life, and the development of catalysts with better activities, selectivities, and stabilities is an attractive research field. Plasmonic-based catalysis has been emerging as a promising approach for developing photocatalysts with greatly enhanced properties by exploiting the excitation of charge carriers in irradiated metal nanostructures.[218] The ability to control the plasmonic response in metal nanomaterials by varying their size, shape, composition, and functionalization has enabled exciting opportunities for exploring and developing better catalytic technologies.[219] Plasmonic nanostars with greatly enhanced fields offer particularly advantageous approaches for accelerating the growth and applications of the nascent field of plasmonic catalysis. Table 10 summarizes recent developments in plasmonic nanostar-based catalysis.

In a recent report,[236] Grzelczak and co-workers conducted a comparative study of the morphological effects of Pt-coated nanostars, nanocubes, and nanorods on the photogeneration of

https://doi.org/10.1021/acsanm.2c02533
ACS Appl. Nano Mater. 2022, 5, 14051−14091

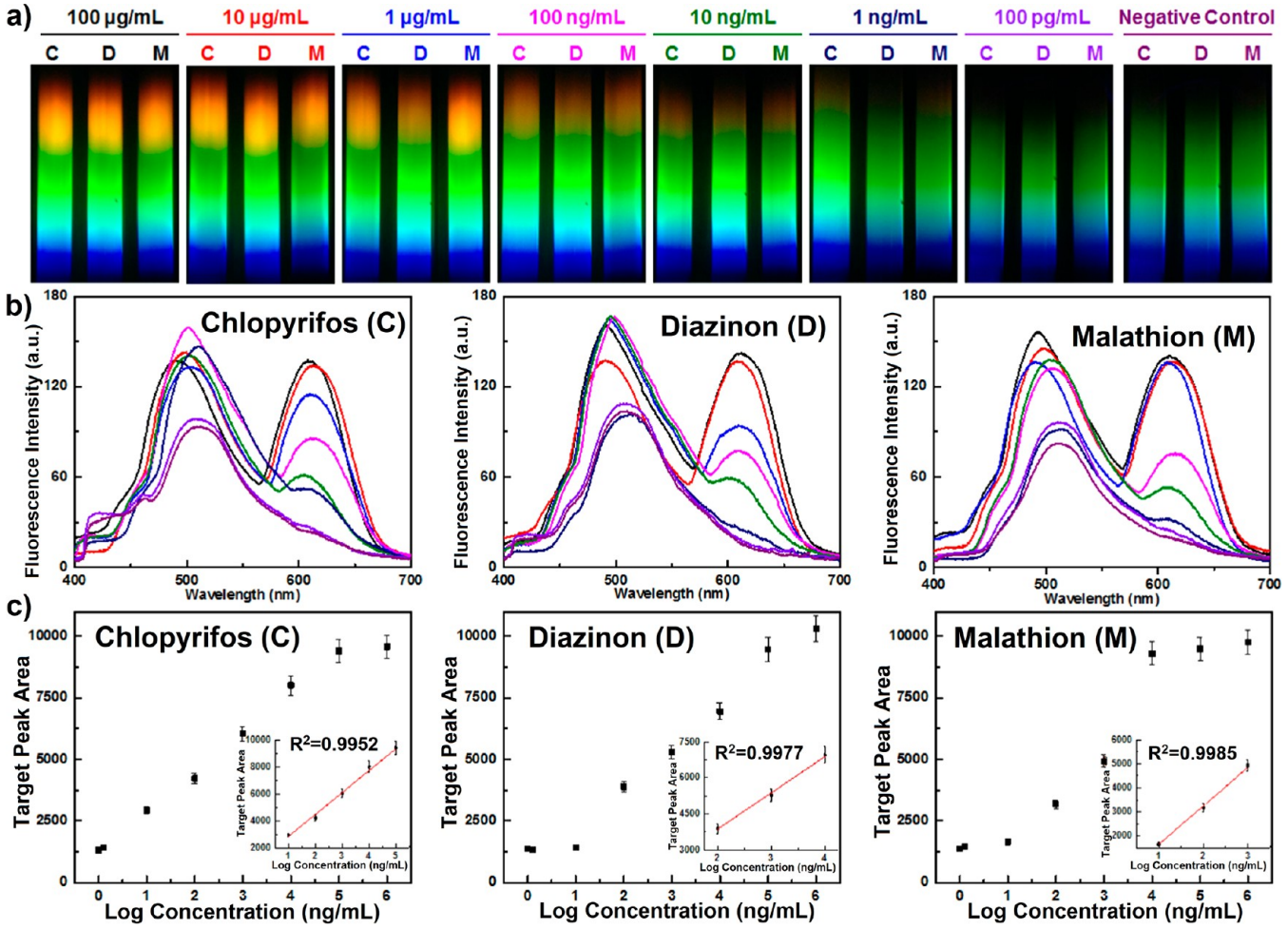

Figure 31. (a) Photographs with different target concentrations from 100 pg/mL to 100 μg/mL and negative control. Targets: chlorpyrifos (C), diazinon (D), and malathion (M). (b) Fluorescence curves of chlorpyrifos, diazinon, and malathion obtained by plotting fluorescence spectra versus concentration. (c) Standard curve of chlorpyrifos, diazinon, and malathion obtained by plotting the target peak area versus the log of concentration (ng/mL). Adapted with permission from ref 178. Copyright 2018 Elsevier.

coenzyme molecules (nicotinamide adenine dinucleotide: NADH) using triethanolamine (TEAOH) as the sacrificial agent. The gold nanostructures were decorated with platinum via a reduction process that allowed platinum growth on the surfaces of gold structures in the presence of silver cations, as shown in Figures 36a–i. To better understand the optical responses of these multimetal nanostructures, the authors simulated the scattering of their cross sections with the surface integral equation-method of moments (SIE-MoM). The results (Figure 36k) showed much less scattering by nanostars than by nanocubes and nanorods. This low level of scattering suggests that nanostars are better light harvesters than other-shaped nanostructures, which can be beneficial for photoelectrocatalytic reactions when using light with a similar spectral range (Figure 36j).

When tested in the photochemical regeneration of cofactor molecules (NADH), all Pt-decorated nanostructures were found to increase the regeneration of NADH by ~sixfold in comparison to the bare nanostructures with the same morphology, as shown in Figure 37a.[236] Importantly, the best catalytic activities were observed for the nanostars, demonstrating the geometrical advantage of nanostars over other morphologies in enhancing photocatalytic activity. The amperometric I–t curves for the electrodes covered with the alloy nanostructures of all three morphologies were obtained (Figure 37b). The presence of Pt boosted the photocurrent by approximately 10 times compared to the photocurrent obtained from the bare gold nanostructures regardless of their shape, suggesting the significant contribution of Pt in the photoelectrocatalytic process. Moreover, the magnitude of the photocurrent in the nanostars was 3.5- and 1.5-times higher than those in the nanocubes and nanorods, respectively. This enhancement showed that the activity of photoelectrocatalytic nanostars is better than those of photocatalysts having other morphologies.

In another recent work,[231] de Barros et al. investigated the biocatalytic effect of AuNSts functionalized with lipase from *Candida antarctica* fraction B (CALB) yeast under 808 nm near-infrared (NIR) laser light excitation. The authors coated CALB on AuNSts and gold nanospheres (AuNSphs) to form nanobioconjugates, which were then used for the biocatalytic hydrolysis of 4-nitrophenyl palmitate (*p*NPP) to 4-nitrophenolate (*p*NP) (Figure 38a). Under NIR laser irradiation, AuNSt@CALB displayed much higher enzymatic activity than AuNSph@CALB over a wide range of laser powers (Figure 38b). These significant enhancements of CALB activity on the surfaces of AuNSts compared to AuNSphs indicated the greatly

https://doi.org/10.1021/acsanm.2c02533
ACS Appl. Nano Mater. 2022, 5, 14051–14091

Table 9. Imaging Applications of Plasmonic Nanostars[a]

core NP	combinatory components	imaging target	imaging mechanism	key results	ref
AuNSt	N/A	MBA molecule	SERS	pH-sensitive label-free Raman mapping of MBA molecules with an enhancement factor of ∼105 over an area of hundreds of μM^2	203
AuNSt-PS bead	4-mercaptobenzoic acid	lung epithelial cancer cell	SERS, DF optical, fluorescence	enhanced cell uptake for the in vitro multimodal imaging of living cells with intermediate yielding high-SERS response	204
AuNSt@Ag@SiO_2	Raman reporter	soft- and hardwood	SERS	AuNSts penetrated both soft- and hardwood for fast SERS imaging even at low quantities without any matrix interactions	205
AuNSt	RGD peptide	microvasculature	PAM, OCT	in vitro and in vivo multimodal PAM and OCT visualization with 17-fold and 167% increase in PAM and OCT contrast, respectively	206
AuNSt	pMBA	tumor cells	SERS, immunoPET	in vivo real-time multimodal multiplexed tumor profiling with dynamic tracking of multiple immunomarkers	207
AuNSt	RGDFC peptide	cancer cells	SERS	super-resolution SERS imaging for probing membrane receptor interactions in cells with a localization precision of ∼6 nm	208
AuNSt	DNAzyme	intracellular Ca^{2+}	SERS, fluorescence	dual-mode monitoring of intracellular Ca^{2+} concentration with good selectivity and sensitivity	209
AuNSt@SiO_2	Raman reporter	microscopic tumors	SERS	visualization of different cancer types with a low LOD of 1.5 fM and a ∼400-fold improvement in Raman signal	210
AuNSt-Fe_3O_4	4-mercaptobenzoic acid	alveolar basal epithelial cells	MRI, CT, PA, optical, SERS	multimodal cellular imaging with many advantages in Janus-like over core−shell structures	211
AuNSt	SERS-labeled antibodies	SMCs	SERS	visualized the presence of SMCs in aortic walls and within atherosclerotic plague areas by multiplex immuno-SERS microscopy	212
AuNSt	NIR dye	HeLa cells	MEF	19-fold fluorescence enhancement in NIR fluorescence imaging of cells with tunable enhancement factors and high signal-to-noise ratio	213
AuNSt	4-mercaptopyridine	lysosomal pH	SERS	monitored pH changes in lysosomes during cellular autophagy and apoptosis with high reliability by high-speed SERS imaging	214
AuNSt	4-marcaptobenzoic acid	i-pH	SERS	visualized local changes in i-pH via high-resolution 3D SERS imaging with good biocompatibility and stability	215
Ag-tip AuNSt	SERS nanotag	cervical cancer exfoliated cells	SERS	ultrasensitive dual detection of cervical cancer biomarkers in clinical samples with strong and reproducible signals	216
AuNSt@SiO_2	N/A	brain tumors	SERS and MSOT	accurate three-dimensional depicting of glioblastoma with high specificity and resolution	217

[a]Abbreviations: PS: polystyrene, DF: dark field, SERS: surface-enhanced Raman spectroscopy, N/A: not applicable, MBA: mercaptobenzoic acid, RGDFC: arginine-glycine-aspartic acid-phenylalanine-cysteine, i-pH: intracellular pH, LOD: limit of detection, SMCs: smooth muscle cells, RGD: arginine-glycine-aspartic acid, PAM: photoacoustic microscopy, OCT: optical coherence tomography, pMBA: *p*-mercaptobenzoic acid, immunoPET: immuno-positron emission tomography, MRI: magnetic resonance imaging, PA: photoacoustic, CT: computed tomography, MEF: metal-enhanced fluorescence, and NIR: near-infrared.

enhancing characteristic of AuNSts enabled by the shape of the plasmonic nanostructure.

In addition to the highlighted studies, various other efforts to develop AuNSt-based catalysts have also been reported in recent publications, as summarized in Table 10. Specifically, AuNSt-based catalysts have been used for hydrogen generation,[221,228,229] methanol oxidation,[228] Suzuki coupling,[235] and pollutant degradation[220,227] via different catalytic approaches, including photocatalytic, electrocatalytic, and photoelectrocatalytic approaches. The wide range of the catalytic applications of AuNSts further indicates the versatility of this unique type of plasmonic nanostructure.

3.5. Photovoltaic Applications of Plasmonic Nanostars. Recently, the studies and applications of photovoltaic devices for converting sunlight directly to electricity have been a critical focus in the global response to the growing concern over fossil fuel-based energy usage. With more than half a century of research and development, photovoltaics is currently a mature field of science.[237] Further advancements to achieve higher-efficiency solar cells might benefit from new approaches in addition to gradual improvements in the structure and active layer materials.[238] Recent developments in the exploitation of plasmonic nanoparticles as efficient light absorbers and current collectors in photovoltaic devices have demonstrated the potential of plasmonic nanomaterials in photovoltaics.[239] The development of plasmonic nanostars has also allowed the advancement of plasmonic photovoltaics, as summarized in Table 11.

In a recent paper,[240] Yang and co-workers introduced 4-(2-hydroxyethyl)-1-piperazineethanesulfonic acid-modified gold nanostars (HEPES-AuNSts) into the SnO_2 electron-transporting layers (ETLs) of heterojunction perovskite solar cells (PSCs), as illustrated in Figures 39a and b. The presence of AuNSts was expected to modify the energy band alignment to facilitate better charge transport for enhanced photovoltaic efficiency (Figure 39c).

The current density vs voltage ($J-V$) responses of the AuNSt-modified PSCs were recorded in reverse scan (R-S) and forward scan (F-S) directions at a scan rate of 130 mV/s under 100 mW/cm^2 AM 1.5G illumination. The $J-V$ curves of AuNSt-modified PSCs remained almost constant (Figure 40a) regardless of the scanning direction. The authors calculated the power conversion efficiencies (PCEs) of R-S and F-S to be 21.13% and 21.10%, respectively, yielding a valid 21.12% efficiency for the AuNSt-modified PSCs. This performance is significantly better than that of the unmodified PSCs, while also exhibiting negligible hysteresis behavior. In addition, the AuNSt-enhanced PSCs showed a spectral response superior to that of the unmodified PSCs in the wavelength range of 350−800 nm (Figure 40b). These results indicate the potential of plasmonic nanostars for enhancing the efficiency and performance of perovskite solar cells, which is worthy of further exploration.

https://doi.org/10.1021/acsanm.2c02533
ACS Appl. Nano Mater. 2022, 5, 14051−14091

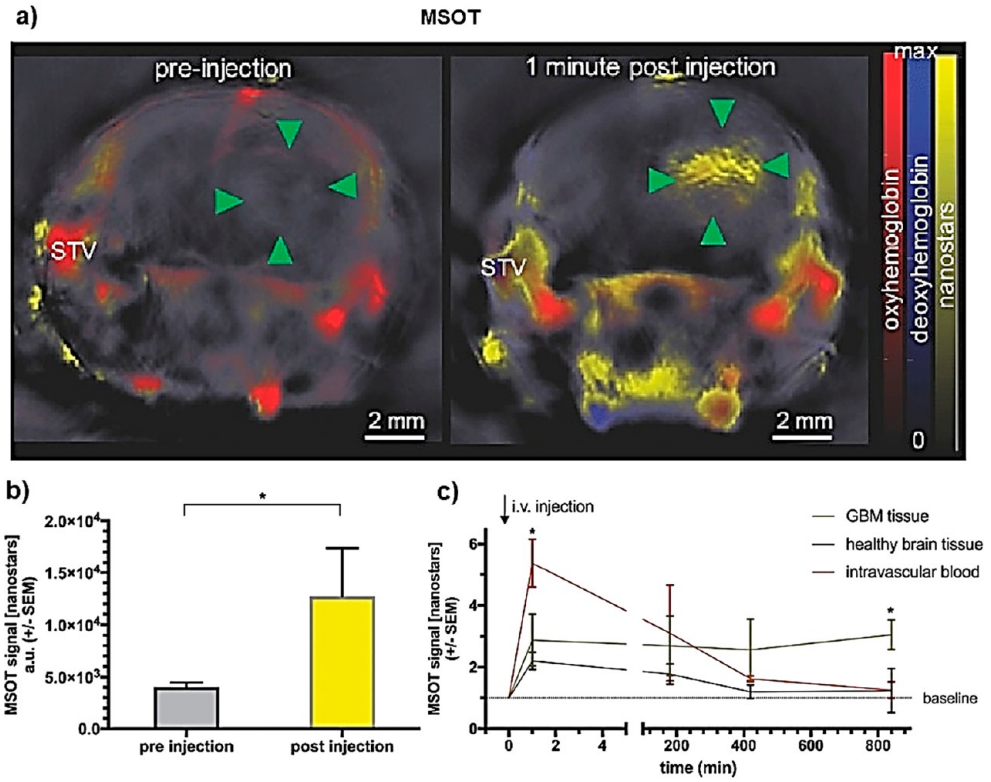

Figure 32. Pharmacokinetic profile of SERRS-MSOT-AuNSts in GBM-bearing mice with (a) MSOT imaging of the tumorous area; (b) increased MSOT signal in the tumor; (c) MSOT signal from the tumor over time following injection of the AuNSt-based contrast agent. Adapted with permission from ref 217. Copyright 2018 Wiley.

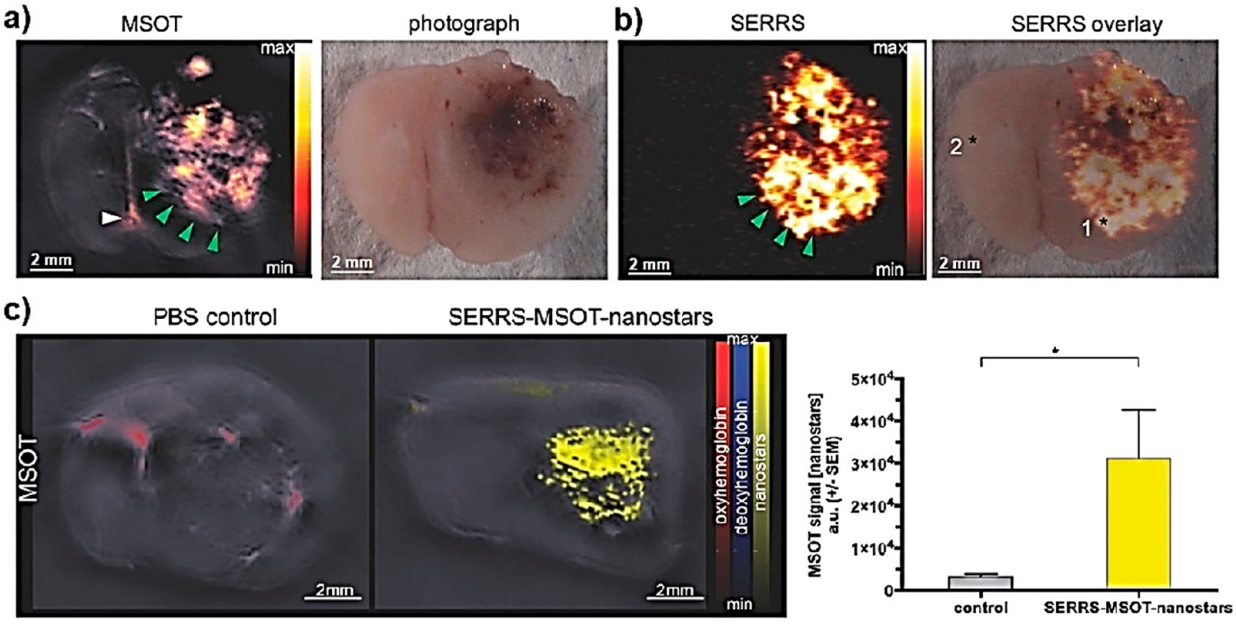

Figure 33. Performance comparisons between a (a) MSOT image and photograph and a (b) SERRS image and overlay photograph of SERRS-MSOT-AuNSt contrast agent. (c) Signal specificity of contrast-enhanced MSOT imaging in GBM tumors. Adapted with permission from ref 217. Copyright 2018 Wiley.

In another work, Ginting et al.[242] demonstrated the use of AuNSts to enhance light absorption in organic solar cells (OSCs) and PSCs. The AuNSts were functionalized with methoxypoly(ethylene glycol) (mPEG) to induce dispersion. The functionalized mPEG-AuNSts were then embedded into the blended layers of thieno[3,4-*b*]thiophene/benzodithiophene (PTB7):[6,6]-phenyl-C_{71}-butyric acid methyl ester ($PC_{71}BM$; hereinafter denoted as PCBM) in OSCs and the perovskite/2,2′,7,7′-tetrakis(*N*,*N*-di-*p*-methoxyphenyl-amine)-9,9′-spirobifluorene (spiro-OMeTAD) interfaces in PSCs, as shown in Figure 41a. The modified AuNSts were incorporated into the aforementioned active layers, with the expectation that

https://doi.org/10.1021/acsanm.2c02533
ACS Appl. Nano Mater. 2022, 5, 14051−14091

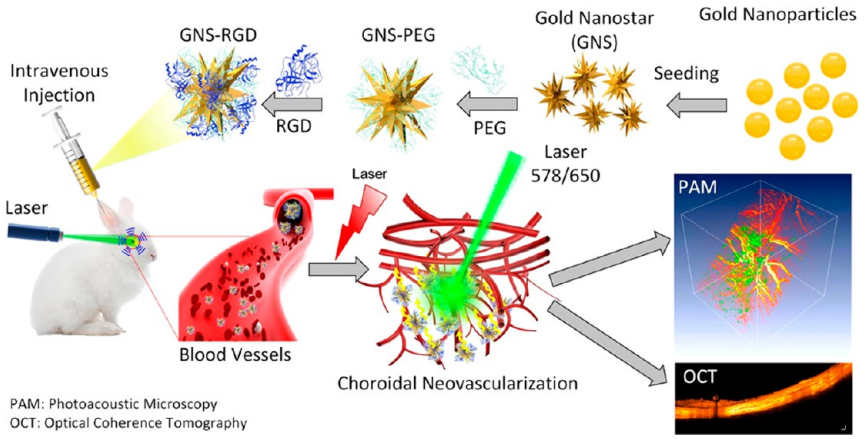

Figure 34. Illustration of an AuNSt-based contrast agent for in vivo imaging of microvasculature with photoacoustic microscopy and optical coherence tomography. Adapted with permission from ref 206. Copyright 2020 American Chemical Society.

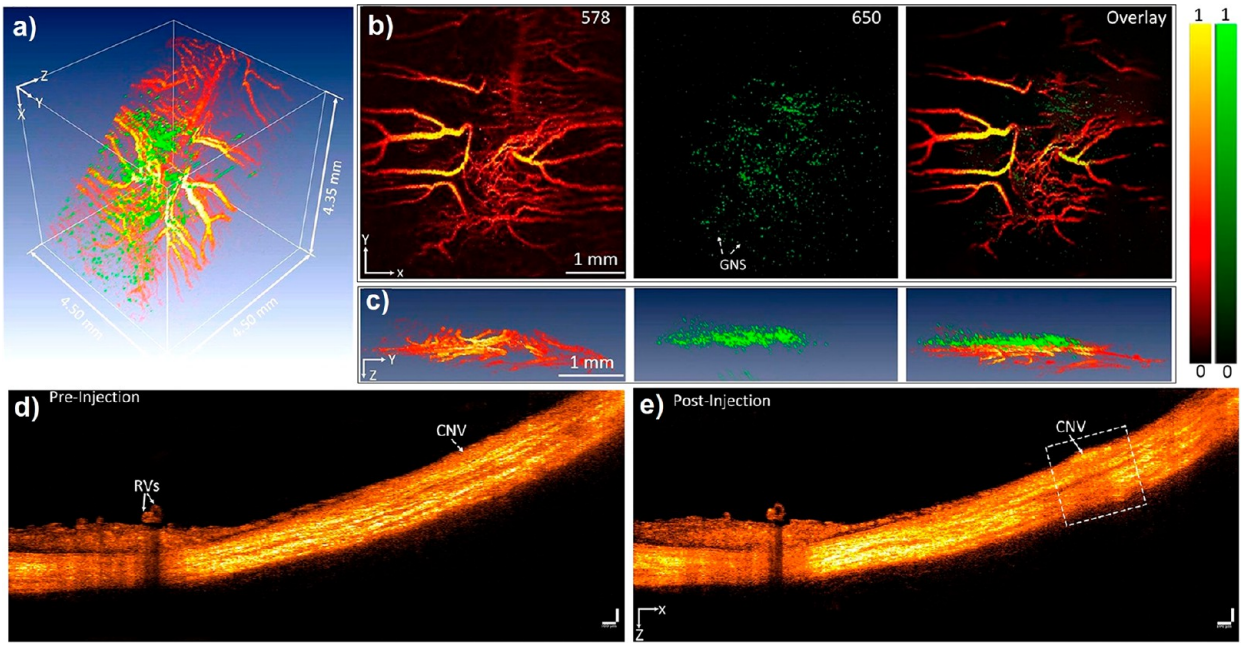

Figure 35. (a) 3D volumetric rendering of PAM images and the (b) horizontal ($y-z$) and (c) vertical PAM images of choroidal neovascularization in rabbit models. The pseudogreen color indicates the distribution of AuNSts. AuNSt-enhanced B-scan OCT images obtained (d) before and (e) after injection of an AuNSt-based contrast agent. Adapted with permission from ref 206. Copyright 2020 American Chemical Society.

the characteristically enhanced field around the AuNSts under light irradiation might assist not only light absorption but also charge transport between these active layers.

To verify the improvement in light absorption after the incorporation of AuNSts into the solar cells, the authors used the finite element method to simulate the electric field distribution around AuNSts positioned in the PTB7:PCBM and spiro-OMeTAD layers.[242] The results in Figures 41b and c show enhanced electric fields around the surfaces of the AuNSts, suggesting the higher absorption properties of the AuNSt-embedded layers. The recorded $J-V$ characteristics with the incorporation of AuNSts demonstrated that the PCEs were boosted from 8.3% to 8.78% and 12.49% to 13.97% for OSCs (Figure 42a) and PSCs (Figure 42b), respectively. These PCEs of the AuNSt-incorporated solar cells are significantly higher than the PCEs in AuNP-incorporated OSCs[248,249] or PSCs.[250] These results suggested that the embedding of AuNSts into the active layers of OSCs and PSCs enhanced their PCEs by 6% and 14%, respectively.

In addition to the studies detailed above, many other works on AuNSt-assisted photovoltaics have also been reported, as summarized in Table 11. The photovoltaic configurations incorporated with AuNSts included not only OSCs and PSCs but also GaAs solar cells[241] and dye-sensitized solar cells (DSSCs).[246] Moreover, the assistance that plasmonic nanostars can provide in photovoltaic devices included not only light absorption[242,247] and electron-transporting layers[240] but also photoanodes[246] or hole-transporting layers.[243] These reports laid out an experimental and simulation basis for further studies and developments to fully understand and realize the potential of plasmonic nanostars to boost photovoltaic performance. Furthermore, in the area of energy-related applications, plasmonic nanostars with their superior properties discussed above also have the potential to improve the efficiency of

https://doi.org/10.1021/acsanm.2c02533
ACS Appl. Nano Mater. 2022, 5, 14051−14091

Table 10. Catalytic Applications of Plasmonic Nanostars[a]

core NP	combinatory components	structure/form	catalytic application	key results	ref
SiO_2@ AuNSt	TiO_2	TiO_2 decorated on AuNSt	organic pollutant degradation	degraded organic dye with remarkable stability and dispersibility; however, the efficiency strongly depended on the anisotropy of the plasmonic component	220
Au-NSt/ NR/NP	TiO_2	core−shell NP	PC H_2 generation	dependence of photocatalytic H_2 generation rate on dimensionality and anisotropy of the plasmonic core with the highest rate at 76.6 μmol g^{-1} h^{-1} for AuNSts	221
AuNSt	Ag	core−shell NP	PC coupling of 4-aminothiophenol	NSt displayed rapid photocatalytic conversion of PATP to DMAB within a few seconds	222
AuNSt	eggshell membrane	immobilized particle	PNP reduction	good catalytic performance with enhanced stability and reusability even after 10 reaction cycles and 100 days	223
AuNSt	N/A	deposited on carbon electrode	electrocatalytic oxidation of EG	high electrocatalytic activity for EG oxidation and better poisoning-resistant ability in alkaline media than irregular Au nanocrystals	224
AuNSt	TiO_2 NR	deposited on TiO_2 photoanode	PEC properties	350% and 20% increases in photocurrent density under visible light and simulated sunlight, respectively, as well as an over 10-fold increase in IPCE efficiency	225
AuNSt	N/A	colloidal NSt	electrocatalytic oxidative reaction	significantly enhanced electrochemical performance upon LSPR excitation with AA detected at an LOD of 10 μM	226
AuNSt	N/A	decorated on GCN and rGO surfaces	PC pollutant degradation	degraded methylene blue under visible light with reusability and excellent photostability	227
AuNSt	AgPt alloy	AgPt-tipped, AgPt-edged, AgPt-covered AuNSt	PEC H_2 evolution, MeOH oxidation	AgPt-tipped AuNSts showed remarkable electrocatalytic H_2 generation and MeOH oxidation with NIR light	228
AuCuNSt	CdS	core−shell NP	PC H_2 generation	H_2 evolution rate increased 2.94-times to 607 μmol $g^{-1}h^{-1}$ with the combination of AuCuNSts and CdS under light with λ > 400 nm	229
AuNSt	N/A	colloidal NSt	PATP PC reaction	AuNSts showed faster PATP catalytic and reduction reaction than AuNP with illustration by FDTD simulation	230
AuNSt	CALB enzyme	colloidal NSt	enzymatic catalysis	58% increase in enzyme activity by LSPR excitation under NIR illumination enabled by photothermal heating	231
AuNSt	N/A	colloidal NSt	4-NTP, 4-NP, 4-NA reduction	high catalytic efficiency in reducing aromatic nitro compounds with selective dependence on the orientation of the compound molecule on the nanostar surface	232
AuNSt	TiO_2	core−shell NP	PC benzyl alcohol aerobic oxidation	enhanced the aerobic oxidation of benzyl alcohol to benzaldehyde at ambient temperature under visible light irradiation	233
AuNSt	mesoporous SiO_2	core−shell NP	4-NP reduction	high catalytic performance of 4-NP reduction; more star branches led to higher activity	234
AuPdNSt	N/A	colloidal NSt	4-NP reduction, Suzuki coupling	synthesized AuPdNSts with tunable LSPR; efficiently enhanced catalytic activity in 4-NP and nitrobenzene reduction and in Suzuki coupling reaction	235
AuNSt and others	Pt	core−shell NP	PEC and PC reaction	AuNSts showed better PEC and PC activities than other morphologies	236

[a]Abbreviations: PC: photocatalytic, NSt: nanostar, NP: nanoparticle, AuNR: gold nanorod, PATP: *p*-aminothiophenol, DMAB: 4,4′-dimercaptoazobenzene, PNP: *p*-aminophenol, EG: ethylene glycol, N/A: not applicable, IPCE: incident photon-to-current conversion efficiency, LSPR: localized surface plasmon resonance, AA: ascorbic acid, LOD: limit of detection, GCN: graphitic carbon nitride, rGO: reduced graphene oxide, NIR: near-infrared, MeOH: methanol, PEC: photoelectrocatalytic, AuCuNSt: gold−copper alloy nanostar, FDTD: finite-difference time-domain, CALB: *Candida antartic*a fraction B, 4-NTP: 4-nitrothiophenol, 4-NP: 4-nitrophenol, 4-NA: 4-nitroaniline, and AuPdNSt: gold−palladium nanostar.

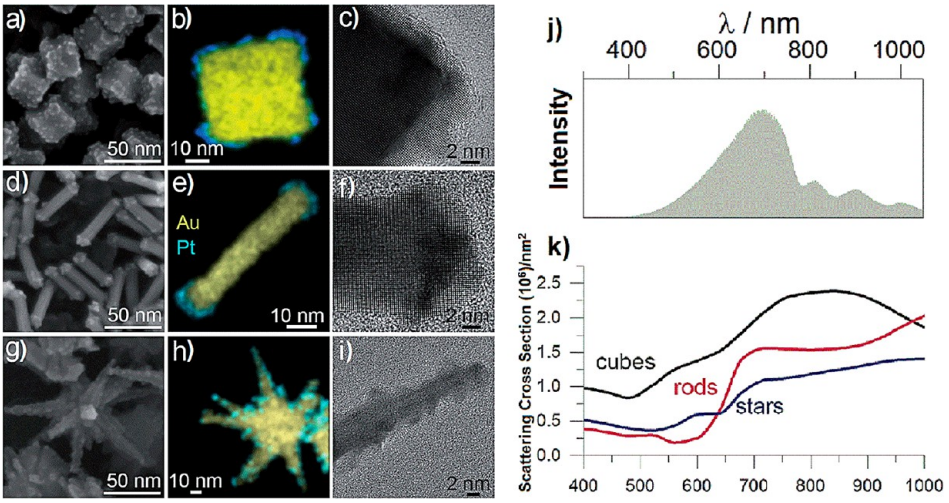

Figure 36. Electron microscopy analysis of Pt-coated gold nanostructures with different shapes: (a−c) cube, (d−f) rod, and (g−i) star. SEM images (a, d, and g) and EDX mapping (b, e, and h) confirming the presence of Pt on the gold surfaces. (c, f, i) HRTEM images of the nanostructures. All structures were covered with 10 mol % Pt. (j) Spectral profile of the lamp used in all experiments. (k) Simulated scattering cross-section spectra of the substrate consisting of three different nanostructures. SEM: scanning electron microscopy, EDX: energy-dispersive X-ray spectroscopy, and HRTEM: high-resolution transmission electron microscopy. Adapted with permission from ref 236 . Copyright 2016 Royal Society of Chemistry.

https://doi.org/10.1021/acsanm.2c02533
ACS Appl. Nano Mater. 2022, 5, 14051−14091

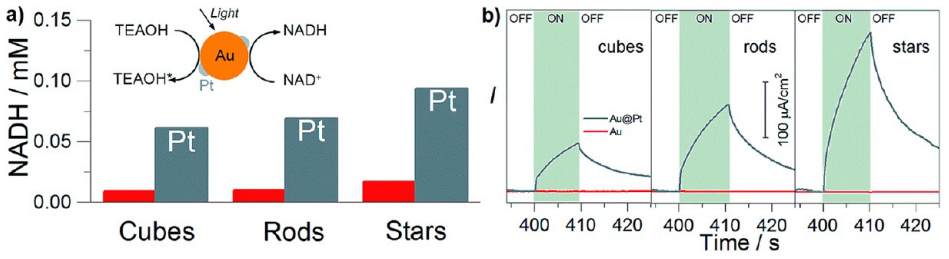

Figure 37. (a) Photochemical regeneration of cofactor molecules (NADH) under visible light irradiation on plasmonic substrate containing different particle shapes. (b) Fast current components for three samples containing Pt-coated nanostructures of different shapes, showing better performance of stars than rods and cubes. Adapted with permission from ref 236. Copyright 2016 Royal Society of Chemistry.

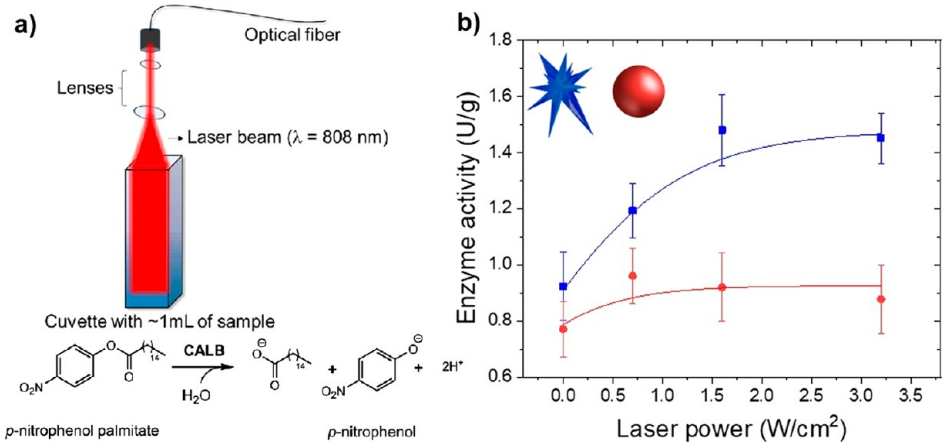

Figure 38. (a) Schematic illustration of the laser irradiation setup for the biocatalytic testing of plasmonic-based nanobioconjugates. (b) Effects of NIR laser power (λ = 808 nm) on the enzymatic activity of AuNSt@CALB (blue) and AuNSph@CALB (red). Adapted with permission from ref 231. Copyright 2021 American Chemical Society.

Table 11. Photovoltaic Applications of Plasmonic Nanostars[a]

core NP	combinatory components	role/position	application	key results	ref
HEPES-AuNSt	SnO_2	ETL	PSCs	ETLs exhibited higher conductivity and greater efficiency in the extraction, transfer, and collection of electrons; PCE reached 21.13% with negligible hysteresis	240
AuNSt	PEDOT−PSS	light trapping	GaAs SCs	enabled much stronger light trapping and increased J_{SC} and PCE up to 5.2% and 3.85%, respectively; systematic investigation of the role of AuNS in these enhancements	241
AuNSt	mPEG	light absorption and scattering	PSCs, OSCs	PCE improved by 6% and 14% in OSCs and PSCs, respectively; better charge separation/transfer and reduced charge recombination rate	242
AuNSt	N/A	between HTL and active layer	OSCs	synergistic plasmon-optical and plasmon-electrical effects resulted in a PCE of up to 10.5% for OSCs with AuNSts and ZnO as ETL	243
AuNSt	TiO_2	photoelectrode	PSCs	achieved a PCE of 17.72% due to enhanced light-harvesting efficiency	244
AuNSt and others	PEDOT−PSS	buffer layer	OSCs	PCE increased the most with AuNSt at 29% compared to 14% of AuNR or 11% of AuNP	245
AuNSt	TiO_2	photoanode	DSSCs	PCE increased up to 30%; IPCE was improved over the wavelength of 380−1000 nm	246
AuNSt	PbS/CdS QD	light absorption	heterojunction SCs	PCE of 4.16%; increased J_{SC} and photoresponse over a broad spectral range	247

[a]Abbreviations: HEPES: 4-(2-hydroxylethyl)-1-piperazineethanesulfonic acid, PSCs: perovskite solar cells, ETL: electron-transporting layer, PCE: power conversion efficiency, PEDOT−PSS: poly(3,4-ethylenedioxythiophene)−poly(styrenesulfonate), J_{SC}: short-circuit current density, mPEG: methoxypoly(ethylene glycol), OSCs: organic solar cells, N/A: not applicable, HTL: hole transport layer, DSSCs: dye-sensitized solar cells, QD: quantum dot, SCs: solar cells, and IPCE: incident photon-to-current conversion efficiency.

batteries more significantly than other nanoparticle counterparts.[251,252]

3.6. Other Applications of Plasmonic Nanostars. Plasmonic nanostars have enabled a wide range of enhanced technologies for advanced applications that benefit from the high specific areas, large numbers of hotspots, and intensified field characteristics of this unique nanostructure class. In addition to the five "large" fields of applications mentioned above, the versatility of plasmonic nanostars also makes them useful in various other "niche" applications, from fundamental research to technological development, as listed in Table 12.

In a recent report,[254] Rettori et al. demonstrated maskless lithography techniques (MLTs) based on the photothermal properties of AuNSts and the thermoplastic characteristics of poly(lactic acid) (PLA) biopolymers. The pattering process involved the deposition of poly(sodium 4-styrenesulfonate) (PSS)-stabilized AuNSts on a PLA film, which was incorporated with Er^{3+}-doped upconversion nanoparticles (UCNPs) for the

https://doi.org/10.1021/acsanm.2c02533
ACS Appl. Nano Mater. 2022, 5, 14051−14091

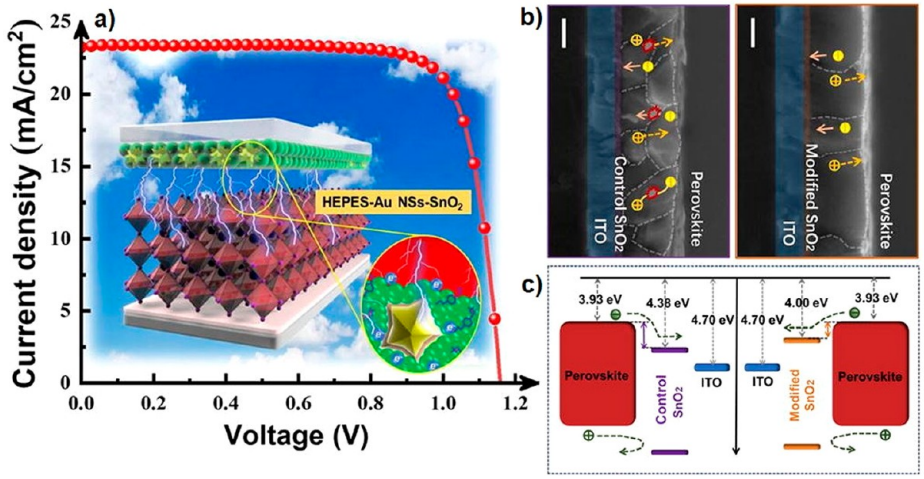

Figure 39. (a) Schematic and (b) cross-section illustration of the incorporation of HEPES-AuNSts into the electron-transporting layers of PSCs. (c) Energy diagram of the PCS device with and without AuNSts. ITO: indium tin oxide electrode. Adapted with permission from ref 240. Copyright 2022 Elsevier.

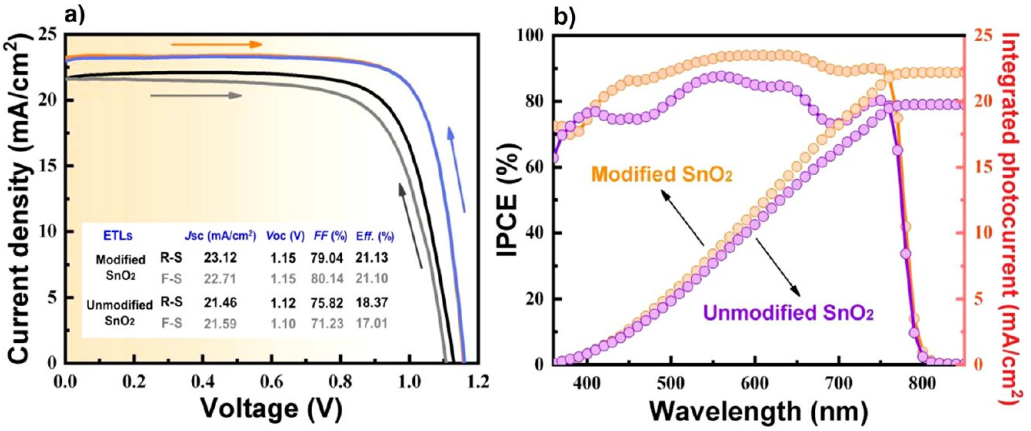

Figure 40. (a) $J-V$ curves and (b) corresponding incident photon-to-current efficiency (IPCE) spectra under forward and reverse scans of the best-performing planar PSCs fabricated with ETLs modified and unmodified with HEPES-AuNSts. Adapted with permission from ref 240. Copyright 2022 Elsevier.

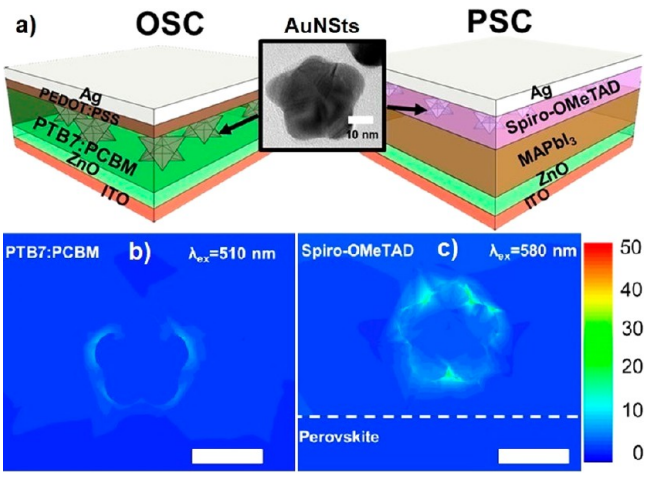

Figure 41. (a) Device configurations showing the positions of gold nanostars (Au NSs) in inverted OSCs and planar-based PSCs. Simulated local electric field distribution around a gold nanostar with respect to the incident light field in (b) PTB7:PCBM and (c) spiro-OMeTAD. ITO: indium tin oxide electrode. Adapted with permission from ref 242. Copyright 2017 American Chemical Society.

visualization of the NIR laser spot and simultaneous probe of the local temperature. A computer numerical control (CNC) system was developed to drive the laser-writing beam following a designed pattern on the AuNSt/PLA-UCNPs nanocomposite (Figure 43a). The irradiated area demonstrated that the PLA polymer was photothermally heated to a temperature higher than its glass transition point and solidified. The irradiated film was then washed to remove the nonirradiated part, revealing the designed patterns without the need for a photomask as in traditional lithography. The author could also adjust the synthesis of AuNSts to achieve an absorption peak matching the wavelength of the NIR laser used at ~976 nm, as shown in Figure 43b. By analyzing the emission spectra in the regions covered and not covered by AuNSts, the study showed a linear relationship between the laser power density and the local temperature on the irradiated AuNSts/PLA-UCNPs film, as displayed in Figure 43c. The temperature range generated by the photothermal heating of AuNSts in this work was much higher than the glass temperature of the PLA polymer at ~60 °C, allowing enough thermal energy for the thermoplastic conversion of PLA for MLTs.

The thermoplastic maskless lithography (TML) technique developed in the report was demonstrated to successfully

https://doi.org/10.1021/acsanm.2c02533
ACS Appl. Nano Mater. 2022, 5, 14051−14091

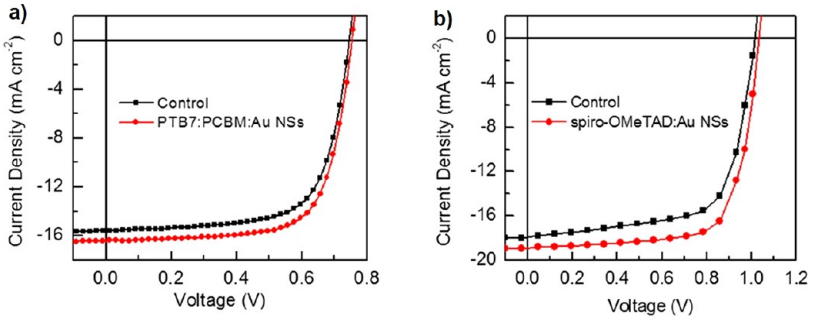

Figure 42. $J-V$ characteristics of (a) OSCs and (b) PSCs under 100 mW/cm^2 AM 1.5G illumination, with and without (control) the incorporation of AuNSts. Adapted with permission from ref 242. Copyright 2017 American Chemical Society.

Table 12. Other Applications of Plasmonic Nanostars[a]

core NP	combinatory components	role/position	application	key results	ref
AuNSt	CB[7]	photothermal activation	cargo delivery	precisely controlled absorption for tunable release of high-loading cargo for biomedicine	253
AuNSt	PLA	photothermal heating	maskless lithography	successfully transferred designed patterns on rigid and flexible substrates with local temperature increased to more than 100 °C	254
AuAgNSt	SiO_2	luminescence enhancement	OLED	increased current densities as well as photo- and electroluminescence up to 50% in OLED	255
AuNSt	N/A	local field intensity enhancement	field electron source	nonlinear photoemission from individual AuNSt with >10^9-fold enhancement of three-photon electron yield	24
AuNSt	N/A	photocathode	optically controlled directional currents	displayed all-optical control over driving, switching, and steering of photocurrents in nanoelectronic devices	25
AuNSt@Ag	SiO_2	gain media enhancement	coherent random laser	substantially reduced pumping threshold in different gain media; coherent random lasing intensity and pumping threshold not influenced by SiO_2 coating	256
AuNSt	N/A	broadband scatterer	random laser	random lasing in an immense spectral coverage of over 410 nm throughout the visible up to the infrared range with efficient feedback mechanism	257
AuNSt	amine-terminated PEG	photothermal neuromodulation	neural activity control	inhibited neural activity of neurons by NIR laser in both chip-attached and cell-attached mode; confirmed single-neuron signal suppression by DMD	258

[a]Abbreviations: CB[7]: cucurbit[7]uril, PLA: poly(lactic acid), OLED: organic light-emitting diode, N/A: not applicable, NIR: near-infrared, DMD: digital micromirror device, and PEG: poly(ethylene glycol).

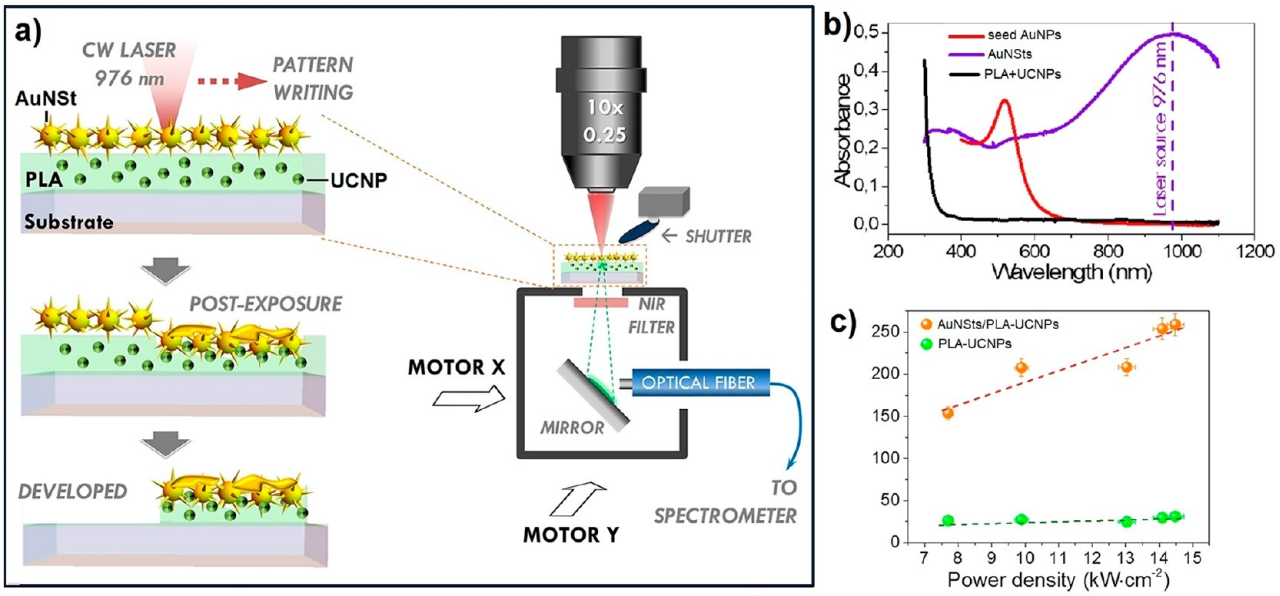

Figure 43. (a) Experimental setup and multilayer samples formed by a substrate, the PLA-UCNPs nanocomposite, and AuNSts. (b) UV−visible spectrophotometry of seed AuNPs and AuNSts in water colloid and nanocomposite PLA-UCNP film compared to the laser source at 976 nm. (c) Calculated local temperature under different laser power densities in the regions covered or uncovered by AuNSts. Adapted with permission from ref 254. Copyright 2019 American Chemical Society.

transfer predesigned patterns onto both rigid glass surface (Figure 44a) and flexible polyimide tape (Figure 44b) substrates.[254] The incorporation of UCNPs into the PLA polymer film provided additional luminescence properties that

https://doi.org/10.1021/acsanm.2c02533
ACS Appl. Nano Mater. 2022, 5, 14051−14091

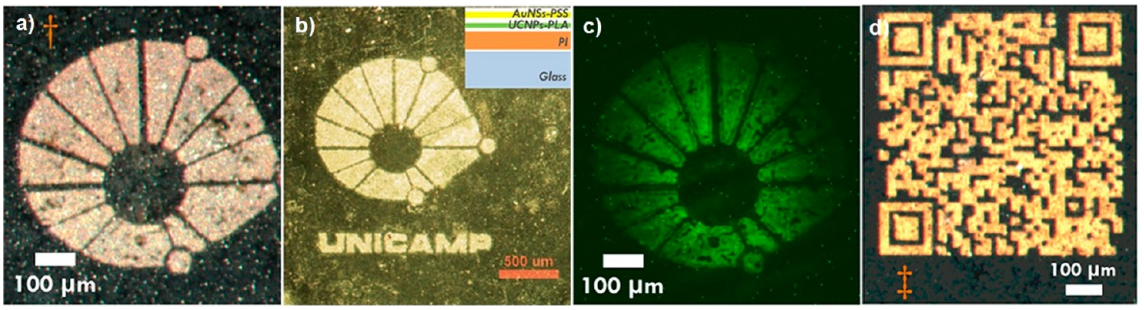

Figure 44. Dark-field microscopy images of the predesigned patterns on (a) glass and (b) flexible polyimide tape deposited with AuNSts and developed by TML. (c) Photon upconverting luminescence image under NIR (976 nm) excitation of the TML pattern. (d) A sample of QR code on a glass substrate. Adapted with permission from ref 254. Copyright 2019 American Chemical Society.

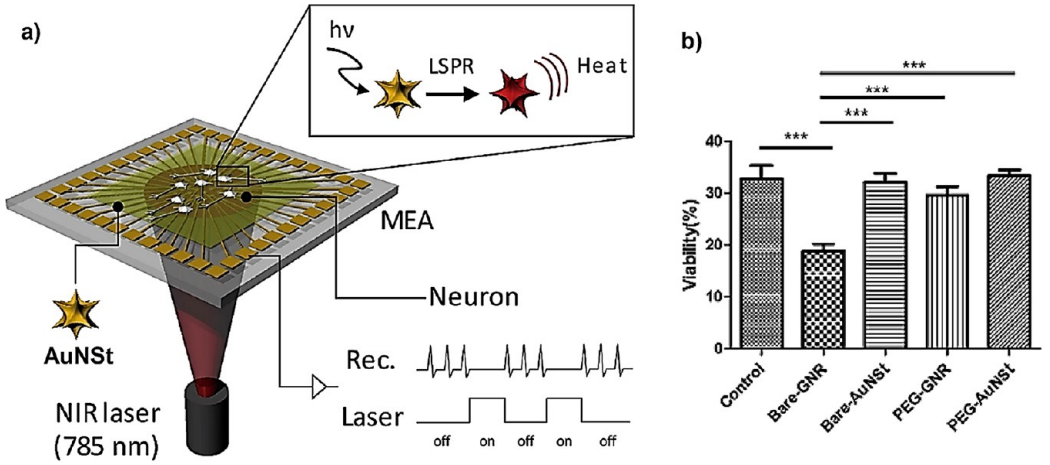

Figure 45. (a) Schematic of the gold nanostar (AuNSts)-mediated NIR light-based neuronal cell stimulation system. (b) Viability tests of neuronal cells in the presence of plasmonic nanostructures under various conditions. *** ($p < 0.0001$). PEG: poly(ethylene glycol), GNR: gold nanorod. Adapted with permission from ref 258. Copyright 2018 Elsevier.

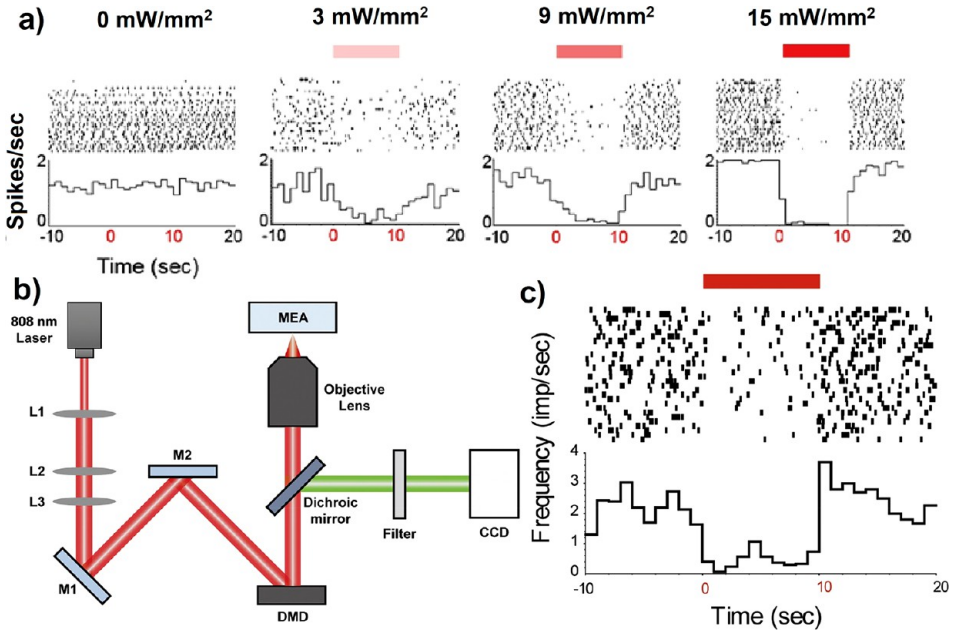

Figure 46. Photothermal inhibition of the spontaneous activity of cultured neuronal networks: (a) peri-stimulus time histogram and raster plots for AuNSt-coated MEA chips with varying laser power. (b) Schematic setup of the DMA-based optical illuminating system with AuNSt-coated MEA for single-neuron signal reading and (c) photothermal inhibition of the spontaneous activity of a single neuron. Adapted with permission from ref 258. Copyright 2018 Elsevier.

https://doi.org/10.1021/acsanm.2c02533
ACS Appl. Nano Mater. 2022, 5, 14051−14091

enabled the formation of luminescent patterns (Figure 44c), which can be used in displays, optical sensors, and anticounterfeiting technologies. The authors also produced a quick response (QR) code (Figure 44d) by this TML technique, which further demonstrates the potential use of TML as an encryption tool.

Another interesting application of plasmonic nanostars for the modulation of neuronal signals via photothermal stimulation was reported by Nam and co-workers.[258] The authors used AuNSt-modified multielectrode array (MEA) chips to manipulate neural signals in hippocampal neurons. The work involved the deposition of AuNSts and hippocampal neurons on MEA chips, which were then illuminated by near-infrared lasers (785 and 808 nm), as illustrated in Figure 45a. Moreover, cell viability tests for the neurons in the presence of the plasmonic nanostructures were performed, and the results (Figure 45b) showed no significant difference in viability between the control sample and the AuNSt samples even though there was a significant viability decrease in the gold nanorod samples, indicating the higher biocompatibility of AuNSts.

This work then demonstrated the capability of the NIR-sensitive AuNSt-coated MEA chips to inhibit the neural activity of hippocampal neurons, as shown in Figure 46.[258] The authors first tested the controlled neural inhibition on a neural network deposited onto the AuNSt-coated MEA chips. With increasing power densities of laser irradiation, the neural signal started to be dampened at 3 mW/mm^2 and became virtually completely suppressed at 15 mW/mm^2 (Figure 46a). The study was further extended to neural inhibition on a single neuron located in the vicinity of the recording electrode. To achieve single-neuron signal reading, a digital micromirror device (DMD)-based illuminating system was used to generate a localized light pattern as small as the single-cell size (Figure 46b). Under irradiation with an NIR laser at a power intensity of 116.24 W/mm^2, the neural signal spike rate was significantly decreased during light stimulation, as displayed in Figure 46c. Similar experiments were also carried out for eight different single neurons located at other electrodes, and similar results were obtained in most of the cases. This work successfully showed that plasmonic nanostars can be used to modulate neuronal activity based on the plasmon-initiated photothermal effect. This modulating capability can be beneficial in studies of neurological disorders (e.g., epilepsy) and for the development of optogenetic technologies.

In addition to the works highlighted in detail above, many other nonconventional studies have also been reported on the applications of plasmonic nanostars as field electron sources[24] and gain media for coherent lasers[256] or light-based current control,[25] as summarized in Table 12. The wide range of application possibilities for plasmonic nanostars in many niche areas further indicates the great potential and versatility of this class of nanostructures. The limited number of reported works, however, calls for more research and development focused on better understanding the complex behaviors of plasmonic nanostars in these systems and further realizing their application potential.

4. CONCLUSIONS AND OUTLOOK

Plasmonic nanostars, as one of the newest types of plasmonic nanostructures, have exhibited many superior advantages over their other more conventional counterparts. These strengths mainly originate from their inherently large specific surface areas and immensely intensified electric fields with arguably the largest numbers of plasmonic hotspots in all of the plasmonic nanostructures that have been fabricated up until now. Over the past decade, by exploitation of their unique advantages, plasmonic nanostars have been increasingly used to advance the state-of-the-art in many technologies, which are crucial for human health, safety, and the resolution of environmental challenges. These contributions span a wide range of fields, such as ultrahigh-sensitivity biomedical diagnostics for early disease screening, targeted triggerable drug deliveries with minimal or no side effects for anticancer or antiviral therapies, activatable and nontoxic photothermal therapies for antibacterial treatments, highly selective bio- and toxin sensors with ultralow detection limits, multimodal imaging for the real-time monitoring of medical procedures, greatly enhanced catalysts for fuel generation and chemical reactions, improved efficiency and stability for photovoltaics, and even neural activity modulations for neurological disease diagnostics and therapies. It is noteworthy that within one plasmonic nanostar template, different capabilities can be integrated for multimodal, multiplexed, multifunctional, and/or synergistic purposes, which opens new avenues for establishing one-stop, real-time, modular platforms for universal applications, especially in medical technologies.

Despite the vast range of applications and impressive performances, plasmonic nanostars are still in their nascent stage and require deeper fundamental scientific understanding, as well as technical insights to introduce plasmonic nanostar-enabled methodologies into mainstream technologies and utilizations. It is obvious through this Review that gold nanostars have been dominant among the different types of plasmonic nanostars partly due to their status as arguably the first metal nanostar reported, in addition to their high biocompatibility and LSPR frequency in the first and second biological optical windows, making them very attractive for biomedical-related technologies. However, gold nanostars still have potential for improvement, especially with regard to their stability when unfunctionalized.[13,28] Furthermore, reliable control of the optical properties of nanostars and the capacity for scaled-up synthesis currently limit their use in real-life applications. These challenges motivate the discovery and development of other types of plasmonic nanostars such as silver, copper, alloy, and hollow nanostars, which can be optically active in UV−visible region of the electromagnetic spectrum complementary to the NIR-region of gold counterparts.[13] The combination of two or more metals also presents a potential but underexplored approach to solve many challenges discussed above as well as open new properties and applications that are not afforded by single-metal plasmonic nanostars.

In conclusion, this Review has summarized the most recent developments in plasmonic nanostar-enabled technologies and their state-of-the-art applications in various areas with great significance for health care, safety, energy supply, environmental remediation, and fundamental studies. This Review also discussed the shortcomings of plasmonic nanostars that need further investigation and the vast potential of this relatively new class of nanomaterials for future exploration and development.

AUTHOR INFORMATION

Corresponding Author

T. Randall Lee − *Department of Chemistry and the Texas Center for Superconductivity, University of Houston, Houston, Texas 77204-5003, United States;* orcid.org/0000-0001-9584-8861; Email: trlee@uh.edu

https://doi.org/10.1021/acsanm.2c02533
ACS Appl. Nano Mater. 2022, 5, 14051−14091

Authors

Nhat M. Ngo − *Department of Chemistry and the Texas Center for Superconductivity, University of Houston, Houston, Texas 77204-5003, United States*

Hung-Vu Tran − *Department of Chemistry and the Texas Center for Superconductivity, University of Houston, Houston, Texas 77204-5003, United States;* orcid.org/0000-0001-8536-2737

Complete contact information is available at: https://pubs.acs.org/10.1021/acsanm.2c02533

Notes

The authors declare no competing financial interest.

■ ACKNOWLEDGMENTS

We thank the Air Force Office of Scientific Research (AFOSR FA9550-20-1-0349; 20RT0302), the Robert A. Welch Foundation (Grant No. E-1320), and the Texas Center for Superconductivity at the University of Houston for generously supporting this research.

■ REFERENCES

(1) Chen, Y.; Fan, Z.; Zhang, Z.; Niu, W.; Li, C.; Yang, N.; Chen, B.; Zhang, H. Two-Dimensional Metal Nanomaterials: Synthesis, Properties, and Applications. *Chem. Rev.* **2018**, *118*, 6409−6455.

(2) Jauffred, L.; Samadi, A.; Klingberg, H.; Bendix, P. M.; Oddershede, L. B. Plasmonic Heating of Nanostructures. *Chem. Rev.* **2019**, *119*, 8087−8130.

(3) Fang, Z.; Zhu, X. Plasmonics in Nanostructures. *Adv. Mater.* **2013**, *25*, 3840−3856.

(4) Jørgensen, J. T.; Norregaard, K.; Tian, P.; Bendix, P. M.; Kjaer, A.; Oddershede, L. B. Single Particle and PET-Based Platform for Identifying Optimal Plasmonic Nano-Heaters for Photothermal Cancer Therapy. *Sci. Rep.* **2016**, *6*, 30076.

(5) Kyriazi, M.-E.; Giust, D.; El-Sagheer, A. H.; Lackie, P. M.; Muskens, O. L.; Brown, T.; Kanaras, A. G. Multiplexed MRNA Sensing and Combinatorial-Targeted Drug Delivery Using DNA-Gold Nanoparticle Dimers. *ACS Nano* **2018**, *12*, 3333−3340.

(6) Li, Z.; Wang, Z.; Khan, J.; LaGasse, M. K.; Suslick, K. S. Ultrasensitive Monitoring of Museum Airborne Pollutants Using a Silver Nanoparticle Sensor Array. *ACS Sens.* **2020**, *5*, 2783−2791.

(7) Mantri, Y.; Jokerst, J. V. Engineering Plasmonic Nanoparticles for Enhanced Photoacoustic Imaging. *ACS Nano* **2020**, *14*, 9408−9422.

(8) Gellé, A.; Price, G. D.; Voisard, F.; Brodusch, N.; Gauvin, R.; Amara, Z.; Moores, A. Enhancing Singlet Oxygen Photocatalysis with Plasmonic Nanoparticles. *ACS Appl. Mater. Interfaces* **2021**, *13*, 35606−35616.

(9) Wang, S.; Jiao, L.; Qian, Y.; Hu, W.; Xu, G.; Wang, C.; Jiang, H. Boosting Electrocatalytic Hydrogen Evolution over Metal−Organic Frameworks by Plasmon-Induced Hot-Electron Injection. *Angew. Chem., Int. Ed.* **2019**, *58*, 10713−10717.

(10) Brady, B.; Steenhof, V.; Nickel, B.; Blackburn, A. M.; Vehse, M.; Brolo, A. G. Plasmonic Light-Trapping Concept for Nanoabsorber Photovoltaics. *ACS Appl. Energy Mater.* **2019**, *2*, 2255−2262.

(11) Chen, H.; Kou, X.; Yang, Z.; Ni, W.; Wang, J. Shape- and Size-Dependent Refractive Index Sensitivity of Gold Nanoparticles. *Langmuir* **2008**, *24*, 5233−5237.

(12) Wang, C.; Zhao, X.-P.; Xu, Q.-Y.; Nie, X.-G.; Younis, M. R.; Liu, W.-Y.; Xia, X.-H. Importance of Hot Spots in Gold Nanostructures on Direct Plasmon-Enhanced Electrochemistry. *ACS Appl. Nano Mater.* **2018**, *1*, 5805−5811.

(13) Ngo, N. M.; Omidiyan, M.; Tran, H.-V.; Lee, T. R. Stable Semi-Hollow Gold-Silver Nanostars with Tunable Plasmonic Resonances Ranging from UV-Visible to Near-Infrared Wavelengths: Implications for Photocatalysis, Biosensing, and Theranostics. *ACS Appl. Nano Mater.* **2022**, *5*, 11391−11399.

(14) Arroyo-Currás, N.; Scida, K.; Ploense, K. L.; Kippin, T. E.; Plaxco, K. W. High Surface Area Electrodes Generated via Electrochemical Roughening Improve the Signaling of Electrochemical Aptamer-Based Biosensors. *Anal. Chem.* **2017**, *89*, 12185−12191.

(15) Auyeung, E.; Morris, W.; Mondloch, J. E.; Hupp, J. T.; Farha, O. K.; Mirkin, C. A. Controlling Structure and Porosity in Catalytic Nanoparticle Superlattices with DNA. *J. Am. Chem. Soc.* **2015**, *137*, 1658−1662.

(16) Zhuang, C.; Xu, Y.; Xu, N.; Wen, J.; Chen, H.; Deng, S. Plasmonic Sensing Characteristics of Gold Nanorods with Large Aspect Ratios. *Sensors* **2018**, *18*, 3458.

(17) Nagy, B. J.; Pápa, Z.; Péter, L.; Prietl, C.; Krenn, J. R.; Dombi, P. Near-Field-Induced Femtosecond Breakdown of Plasmonic Nanoparticles. *Plasmonics* **2020**, *15*, 335−340.

(18) Gutiérrez, Y.; de la Osa, R. A.; Ortiz, D.; Saiz, J.; González, F.; Moreno, F. Plasmonics in the Ultraviolet with Aluminum, Gallium, Magnesium and Rhodium. *Appl. Sci.* **2018**, *8*, 64.

(19) Kaminska, I.; Maurer, T.; Nicolas, R.; Renault, M.; Lerond, T.; Salas-Montiel, R.; Herro, Z.; Kazan, M.; Niedziolka-Jönsson, J.; Plain, J.; Adam, P.-M.; Boukherroub, R.; Szunerits, S. Near-Field and Far-Field Sensitivities of LSPR Sensors. *J. Phys. Chem. C* **2015**, *119*, 9470−9476.

(20) Marinica, D. C.; Kazansky, A. K.; Nordlander, P.; Aizpurua, J.; Borisov, A. G. Quantum Plasmonics: Nonlinear Effects in the Field Enhancement of a Plasmonic Nanoparticle Dimer. *Nano Lett.* **2012**, *12*, 1333−1339.

(21) Wan, W.; Yin, J.; Wu, Y.; Zheng, X.; Yang, W.; Wang, H.; Zhou, J.; Chen, J.; Wu, Z.; Li, X.; Kang, J. Polarization-Controllable Plasmonic Enhancement on the Optical Response of Two-Dimensional GaSe Layers. *ACS Appl. Mater. Interfaces* **2019**, *11*, 19631−19637.

(22) Minamimoto, H.; Zhou, R.; Fukushima, T.; Murakoshi, K. Unique Electronic Excitations at Highly Localized Plasmonic Field. *Acc. Chem. Res.* **2022**, *55*, 809−818.

(23) Yamazaki, Y.; Kuwahara, Y.; Mori, K.; Kamegawa, T.; Yamashita, H. Enhanced Catalysis of Plasmonic Silver Nanoparticles by a Combination of Macro-/Mesoporous Nanostructured Silica Support. *J. Phys. Chem. C* **2021**, *125*, 9150−9157.

(24) Sivis, M.; Pazos-Perez, N.; Yu, R.; Alvarez-Puebla, R.; García de Abajo, F. J.; Ropers, C. Continuous-Wave Multiphoton Photoemission from Plasmonic Nanostars. *Commun. Phys.* **2018**, *1*, 13.

(25) Pettine, J.; Choo, P.; Medeghini, F.; Odom, T. W.; Nesbitt, D. J. Plasmonic Nanostar Photocathodes for Optically-Controlled Directional Currents. *Nat. Commun.* **2020**, *11*, 1367.

(26) Ning, S.; Zhang, N.; Dong, H.; Hou, X.; Zhang, F.; Wu, Z. Enhanced Lasing from Organic Gain Medium by Au Nanocube@SiO_2 Core-Shell Nanoparticles with Optimal Size. *Opt. Mater. Express* **2018**, *8*, 3014.

(27) Gao, Y.; Wang, J.; Wang, W.; Zhao, T.; Cui, Y.; Liu, P.; Xu, S.; Luo, X. More Symmetrical "Hot Spots" Ensure Stronger Plasmon-Enhanced Fluorescence: From Au Nanorods to Nanostars. *Anal. Chem.* **2021**, *93*, 2480−2489.

(28) Xi, W.; Phan, H. T.; Haes, A. J. How to Accurately Predict Solution-Phase Gold Nanostar Stability. *Anal. Bioanal. Chem.* **2018**, *410*, 6113−6123.

(29) Chandra, K.; Culver, K. S. B.; Werner, S. E.; Lee, R. C.; Odom, T. W. Manipulating the Anisotropic Structure of Gold Nanostars Using Good's Buffers. *Chem. Mater.* **2016**, *28*, 6763−6769.

(30) Khoury, C. G.; Vo-Dinh, T. Gold Nanostars For Surface-Enhanced Raman Scattering: Synthesis, Characterization and Optimization. *J. Phys. Chem. C* **2008**, *112*, 18849−18859.

(31) Atta, S.; Beetz, M.; Fabris, L. Understanding the Role of $AgNO_3$ Concentration and Seed Morphology in the Achievement of Tunable Shape Control in Gold Nanostars. *Nanoscale* **2019**, *11*, 2946−2958.

(32) Chatterjee, H.; Rahman, D. S.; Sengupta, M.; Ghosh, S. K. Gold Nanostars in Plasmonic Photothermal Therapy: The Role of Tip Heads in the Thermoplasmonic Landscape. *J. Phys. Chem. C* **2018**, *122*, 13082−13094.

(33) Umadevi, S.; Lee, H. C.; Ganesh, V.; Feng, X.; Hegmann, T. A Versatile, One-Pot Synthesis of Gold Nanostars with Long, Well-

Defined Thorns Using a Lyotropic Liquid Crystal Template. *Liq. Cryst.* **2014**, *41*, 265−276.
(34) Liebig, F.; Henning, R.; Sarhan, R. M.; Prietzel, C.; Schmitt, C. N. Z.; Bargheer, M.; Koetz, J. A Simple One-Step Procedure to Synthesise Gold Nanostars in Concentrated Aqueous Surfactant Solutions. *RSC Adv.* **2019**, *9*, 23633−23641.
(35) Chatterjee, S.; Ringane, A. B.; Arya, A.; Das, G. M.; Dantham, V. R.; Laha, R.; Hussian, S. A High-Yield, One-Step Synthesis of Surfactant-Free Gold Nanostars and Numerical Study for Single-Molecule SERS Application. *J. Nanopart. Res.* **2016**, *18*, 242.
(36) Garcia-Leis, A.; Rivera-Arreba, I.; Sanchez-Cortes, S. Morphological Tuning of Plasmonic Silver Nanostars by Controlling the Nanoparticle Growth Mechanism: Application in the SERS Detection of the Amyloid Marker Congo Red. *Colloids Surf., A* **2017**, *535*, 49−60.
(37) Zeng, L.; Pan, Y.; Wang, S.; Wang, X.; Zhao, X.; Ren, W.; Lu, G.; Wu, A. Raman Reporter-Coupled Ag_{core}@Au_{shell} Nanostars for *in Vivo* Improved Surface Enhanced Raman Scattering Imaging and Near-Infrared-Triggered Photothermal Therapy in Breast Cancers. *ACS Appl. Mater. Interfaces* **2015**, *7*, 16781−16791.
(38) Fales, A. M.; Yuan, H.; Vo-Dinh, T. Development of Hybrid Silver-Coated Gold Nanostars for Nonaggregated Surface-Enhanced Raman Scattering. *J. Phys. Chem. C* **2014**, *118*, 3708−3715.
(39) He, R.; Wang, Y.-C.; Wang, X.; Wang, Z.; Liu, G.; Zhou, W.; Wen, L.; Li, Q.; Wang, X.; Chen, X.; Zeng, J.; Hou, J. G. Facile Synthesis of Pentacle Gold−Copper Alloy Nanocrystals and Their Plasmonic and Catalytic Properties. *Nat. Commun.* **2014**, *5*, 4327.
(40) Bazán-Díaz, L.; Mendoza-Cruz, R.; Velázquez-Salazar, J. J.; Plascencia-Villa, G.; Romeu, D.; Reyes-Gasga, J.; Herrera-Becerra, R.; José-Yacamán, M.; Guisbiers, G. Gold−Copper Nanostars as Photo-Thermal Agents: Synthesis and Advanced Electron Microscopy Characterization. *Nanoscale* **2015**, *7*, 20734−20742.
(41) Ma, X.; Sim, S. J. Single Plasmonic Nanostructures for Biomedical Diagnosis. *J. Mater. Chem. B* **2020**, *8*, 6197−6216.
(42) Zhou, W.; Gao, X.; Liu, D.; Chen, X. Gold Nanoparticles for In Vitro Diagnostics. *Chem. Rev.* **2015**, *115*, 10575−10636.
(43) Theodorou, I. G.; Jawad, Z. A. R.; Jiang, Q.; Aboagye, E. O.; Porter, A. E.; Ryan, M. P.; Xie, F. Gold Nanostar Substrates for Metal-Enhanced Fluorescence through the First and Second Near-Infrared Windows. *Chem. Mater.* **2017**, *29*, 6916−6926.
(44) Yuan, H.; Liu, Y.; Fales, A. M.; Li, Y. L.; Liu, J.; Vo-Dinh, T. Quantitative Surface-Enhanced Resonant Raman Scattering Multiplexing of Biocompatible Gold Nanostars for in Vitro and Ex Vivo Detection. *Anal. Chem.* **2013**, *85*, 208−212.
(45) Su, Y.; Xu, S.; Zhang, J.; Chen, X.; Jiang, L.-P.; Zheng, T.; Zhu, J.-J. Plasmon Near-Field Coupling of Bimetallic Nanostars and a Hierarchical Bimetallic SERS "Hot Field": Toward Ultrasensitive Simultaneous Detection of Multiple Cardiorenal Syndrome Biomarkers. *Anal. Chem.* **2019**, *91*, 864−872.
(46) Jimenez de Aberasturi, D.; Serrano-Montes, A. B.; Langer, J.; Henriksen-Lacey, M.; Parak, W. J.; Liz-Marzán, L. M. Surface Enhanced Raman Scattering Encoded Gold Nanostars for Multiplexed Cell Discrimination. *Chem. Mater.* **2016**, *28*, 6779−6790.
(47) Pramanik, A.; Mayer, J.; Patibandla, S.; Gates, K.; Gao, Y.; Davis, D.; Seshadri, R.; Ray, P. C. Mixed-Dimensional Heterostructure Material-Based SERS for Trace Level Identification of Breast Cancer-Derived Exosomes. *ACS Omega* **2020**, *5*, 16602−16611.
(48) Bhamidipati, M.; Lee, G.; Kim, I.; Fabris, L. SERS-Based Quantification of PSMA in Tissue Microarrays Allows Effective Stratification of Patients with Prostate Cancer. *ACS Omega* **2018**, *3*, 16784−16794.
(49) Wang, S.-S.; Zhao, X.-P.; Liu, F.-F.; Younis, M. R.; Xia, X.-H.; Wang, C. Direct Plasmon-Enhanced Electrochemistry for Enabling Ultrasensitive and Label-Free Detection of Circulating Tumor Cells in Blood. *Anal. Chem.* **2019**, *91*, 4413−4420.
(50) Oseledchyk, A.; Andreou, C.; Wall, M. A.; Kircher, M. F. Folate-Targeted Surface-Enhanced Resonance Raman Scattering Nanoprobe Ratiometry for Detection of Microscopic Ovarian Cancer. *ACS Nano* **2017**, *11*, 1488−1497.
(51) Darienzo, R. E.; Wang, J.; Chen, O.; Sullivan, M.; Mironava, T.; Kim, H.; Tannenbaum, R. Surface-Enhanced Raman Spectroscopy Characterization of Breast Cell Phenotypes: Effect of Nanoparticle Geometry. *ACS Appl. Nano Mater.* **2019**, *2*, 6960−6970.
(52) Bagheri Hashkavayi, A.; Cha, B. S.; Hwang, S. H.; Kim, J.; Park, K. S. Highly Sensitive Electrochemical Detection of Circulating EpCAM-Positive Tumor Cells Using a Dual Signal Amplification Strategy. *Sens. Actuators, B* **2021**, *343*, 130087.
(53) Sohrabi Kashani, A.; Badilescu, S.; Piekny, A.; Packirisamy, M. Differing Affinities of Gold Nanostars and Nanospheres toward HeLa and HepG2 Cells: Implications for Cancer Therapy. *ACS Appl. Nano Mater.* **2020**, *3*, 4114−4126.
(54) Xiang, S.; Lu, L.; Zhong, H.; Lu, M.; Mao, H. SERS Diagnosis of Liver Fibrosis in the Early Stage Based on Gold Nanostar Liver Targeting Tags. *Biomater. Sci.* **2021**, *9*, 5035−5044.
(55) Zhao, J.; Wu, C.; Zhai, L.; Shi, X.; Li, X.; Weng, G.; Zhu, J.; Li, J.; Zhao, J.-W. A SERS-Based Immunoassay for the Detection of α-Fetoprotein Using AuNS@Ag@SiO_2 Core−Shell Nanostars. *J. Mater. Chem. C* **2019**, *7*, 8432−8441.
(56) Li, L.; Liao, M.; Chen, Y.; Shan, B.; Li, M. Surface-Enhanced Raman Spectroscopy (SERS) Nanoprobes for Ratiometric Detection of Cancer Cells. *J. Mater. Chem. B* **2019**, *7*, 815−822.
(57) Han, X.; Shokri Kojori, H.; Leblanc, R. M.; Kim, S. J. Ultrasensitive Plasmonic Biosensors for Real-Time Parallel Detection of Alpha-L-Fucosidase and Cardiac-Troponin-I in Whole Human Blood. *Anal. Chem.* **2018**, *90*, 7795−7799.
(58) Wang, Y.; Yang, Y.; Chen, C.; Wang, S.; Wang, H.; Jing, W.; Tao, N. One-Step Digital Immunoassay for Rapid and Sensitive Detection of Cardiac Troponin I. *ACS Sens.* **2020**, *5*, 1126−1131.
(59) Wilkins, M. D.; Turner, B. L.; Rivera, K. R.; Menegatti, S.; Daniele, M. Quantum Dot Enabled Lateral Flow Immunoassay for Detection of Cardiac Biomarker NT-ProBNP. *Sens. Bio-Sens. Res.* **2018**, *21*, 46−53.
(60) Jiang, M.; Xie, H.; Zhu, J.; Ma, H.; Zheng, N.; Li, S.; Xiao, J.; Wang, Y.; Cai, L.; Han, X. Molecular Form-Specific Immunoassays for Neutrophil Gelatinase-Associated Lipocalin by Surface-Enhanced Raman Spectroscopy. *Sens. Actuators, B* **2019**, *297*, 126742.
(61) Kannan, P.; Tiong, H. Y.; Kim, D.-H. Highly Sensitive Electrochemical Determination of Neutrophil Gelatinase-Associated Lipocalin for Acute Kidney Injury. *Biosens. Bioelectron.* **2012**, *31*, 32−36.
(62) Mieszawska, A. J.; Mulder, W. J. M.; Fayad, Z. A.; Cormode, D. P. Multifunctional Gold Nanoparticles for Diagnosis and Therapy of Disease. *Mol. Pharmaceutics* **2013**, *10*, 831−847.
(63) Zhang, L.; Chen, Q.; Ma, Y.; Sun, J. Microfluidic Methods for Fabrication and Engineering of Nanoparticle Drug Delivery Systems. *ACS Appl. Bio Mater.* **2020**, *3*, 107−120.
(64) Kumar, U. S.; Afjei, R.; Ferrara, K.; Massoud, T. F.; Paulmurugan, R. Gold-Nanostar-Chitosan-Mediated Delivery of SARS-CoV-2 DNA Vaccine for Respiratory Mucosal Immunization: Development and Proof-of-Principle. *ACS Nano* **2021**, *15*, 17582−17601.
(65) Cai, Z.; Zhang, Y.; He, Z.; Jiang, L.-P.; Zhu, J.-J. NIR-Triggered Chemo-Photothermal Therapy by Thermosensitive Gold Nanostar@Mesoporous Silica@Liposome-Composited Drug Delivery Systems. *ACS Appl. Bio Mater.* **2020**, *3*, 5322−5330.
(66) Miao, D.; Yu, Y.; Chen, Y.; Liu, Y.; Su, G. Facile Construction of i-Motif DNA-Conjugated Gold Nanostars as Near-Infrared and pH Dual-Responsive Targeted Drug Delivery Systems for Combined Cancer Therapy. *Mol. Pharmaceutics* **2020**, *17*, 1127−1138.
(67) Wu, R.; Min, Q.; Guo, J.; Zheng, T.; Jiang, L.; Zhu, J.-J. Sequential Delivery and Cascade Targeting of Peptide Therapeutics for Triplexed Synergistic Therapy with Real-Time Monitoring Shuttled by Magnetic Gold Nanostars. *Anal. Chem.* **2019**, *91*, 4608−4617.
(68) Xu, P.; Feng, Q.; Yang, X.; Liu, S.; Xu, C.; Huang, L.; Chen, M.; Liang, F.; Cheng, Y. Near Infrared Light Triggered Cucurbit[7]Uril-Stabilized Gold Nanostars as a Supramolecular Nanoplatform for Combination Treatment of Cancer. *Bioconjugate Chem.* **2018**, *29*, 2855−2866.

https://doi.org/10.1021/acsanm.2c02533
ACS Appl. Nano Mater. 2022, 5, 14051−14091

(69) Lee, H.; Dam, D. H. M.; Ha, J. W.; Yue, J.; Odom, T. W. Enhanced Human Epidermal Growth Factor Receptor 2 Degradation in Breast Cancer Cells by Lysosome-Targeting Gold Nanoconstructs. *ACS Nano* **2015**, *9*, 9859−9867.
(70) Zhu, J.; Sevencan, C.; Zhang, M.; McCoy, R. S. A.; Ding, X.; Ye, J.; Xie, J.; Ariga, K.; Feng, J.; Bay, B. H.; Leong, D. T. Increasing the Potential Interacting Area of Nanomedicine Enhances Its Homotypic Cancer Targeting Efficacy. *ACS Nano* **2020**, *14*, 3259−3271.
(71) Hasanzadeh Kafshgari, M.; Agiotis, L.; Largillière, I.; Patskovsky, S.; Meunier, M. Antibody-Functionalized Gold Nanostar-Mediated On-Resonance Picosecond Laser Optoporation for Targeted Delivery of RNA Therapeutics. *Small* **2021**, *17*, 2007577.
(72) Carrillo-Carrión, C.; Martínez, R.; Navarro Poupard, M. F.; Pelaz, B.; Polo, E.; Arenas-Vivo, A.; Olgiati, A.; Taboada, P.; Soliman, M. G.; Catalán, Ú.; Fernández-Castillejo, S.; Solà, R.; Parak, W. J.; Horcajada, P.; Alvarez-Puebla, R. A.; del Pino, P. Aqueous Stable Gold Nanostar/ZIF-8 Nanocomposites for Light-Triggered Release of Active Cargo Inside Living Cells. *Angew. Chem., Int. Ed.* **2019**, *58*, 7078−7082.
(73) Hu, Y.; Liu, Y.; Xie, X.; Bao, W.; Hao, J. Surfactant-Regulated Fabrication of Gold Nanostars in Magnetic Core/Shell Hybrid Nanoparticles for Controlled Release of Drug. *J. Colloid Interface Sci.* **2018**, *529*, 547−555.
(74) Montoto, A. H.; Montes, R.; Samadi, A.; Gorbe, M.; Terrés, J. M.; Cao-Milán, R.; Aznar, E.; Ibañez, J.; Masot, R.; Marcos, M. D.; Orzáez, M.; Sancenón, F.; Oddershede, L. B.; Martínez-Máñez, R. Gold Nanostars Coated with Mesoporous Silica Are Effective and Nontoxic Photothermal Agents Capable of Gate Keeping and Laser-Induced Drug Release. *ACS Appl. Mater. Interfaces* **2018**, *10*, 27644−27656.
(75) Wu, D.; Zhao, P.; Wu, L.; Lin, L.; Yu, G.; Xu, L.; Yue, J. Aptamer-Functionalized Gold Nanostars for on-Demand Delivery of Anticancer Therapeutics. *ACS Appl. Bio Mater.* **2020**, *3*, 4590−4599.
(76) Yin, T.; Xie, W.; Sun, J.; Yang, L.; Liu, J. Penetratin Peptide-Functionalized Gold Nanostars: Enhanced BBB Permeability and NIR Photothermal Treatment of Alzheimer's Disease Using Ultralow Irradiance. *ACS Appl. Mater. Interfaces* **2016**, *8*, 19291−19302.
(77) Medhi, R.; Srinoi, P.; Ngo, N.; Tran, H.-V.; Lee, T. R. Nanoparticle-Based Strategies to Combat COVID-19. *ACS Appl. Nano Mater.* **2020**, *3*, 8557−8580.
(78) Chen, Z.; Wan, L.; Yuan, Y.; Kuang, Y.; Xu, X.; Liao, T.; Liu, J.; Xu, Z.-Q.; Jiang, B.; Li, C. pH/GSH-Dual-Sensitive Hollow Mesoporous Silica Nanoparticle-Based Drug Delivery System for Targeted Cancer Therapy. *ACS Biomater. Sci. Eng.* **2020**, *6*, 3375−3387.
(79) Yang, J.; Shen, D.; Zhou, L.; Li, W.; Li, X.; Yao, C.; Wang, R.; El-Toni, A. M.; Zhang, F.; Zhao, D. Spatially Confined Fabrication of Core−Shell Gold Nanocages@Mesoporous Silica for Near-Infrared Controlled Photothermal Drug Release. *Chem. Mater.* **2013**, *25*, 3030−3037.
(80) Liu, J.; Detrembleur, C.; De Pauw-Gillet, M.-C.; Mornet, S.; Jérôme, C.; Duguet, E. Gold Nanorods Coated with Mesoporous Silica Shell as Drug Delivery System for Remote Near Infrared Light-Activated Release and Potential Phototherapy. *Small* **2015**, *11*, 2323−2332.
(81) Lucky, S. S.; Soo, K. C.; Zhang, Y. Nanoparticles in Photodynamic Therapy. *Chem. Rev.* **2015**, *115*, 1990−2042.
(82) Liu, Y.; Maccarini, P.; Palmer, G. M.; Etienne, W.; Zhao, Y.; Lee, C.-T.; Ma, X.; Inman, B. A.; Vo-Dinh, T. Synergistic Immuno Photothermal Nanotherapy (SYMPHONY) for the Treatment of Unresectable and Metastatic Cancers. *Sci. Rep.* **2017**, *7*, 8606.
(83) Carrillo-Carrión, C.; Martínez, R.; Polo, E.; Tomás-Gamasa, M.; Destito, P.; Ceballos, M.; Pelaz, B.; López, F.; Mascareñas, J. L.; Pino, P. d. Plasmonic-Assisted Thermocyclizations in Living Cells Using Metal−Organic Framework Based Nanoreactors. *ACS Nano* **2021**, *15*, 16924−16933.
(84) Wang, S.; Tian, Y.; Tian, W.; Sun, J.; Zhao, S.; Liu, Y.; Wang, C.; Tang, Y.; Ma, X.; Teng, Z.; Lu, G. Selectively Sensitizing Malignant Cells to Photothermal Therapy Using a CD44-Targeting Heat Shock Protein 72 Depletion Nanosystem. *ACS Nano* **2016**, *10*, 8578−8590.
(85) Zheng, Y.; Zhang, Y.; Zhang, T.; Cai, H.; Xie, X.; Yang, Y.; Quan, J.; Wu, H. AuNSs@Glycopolymer-ConA Hybrid Nanoplatform for Photothermal Therapy of Hepatoma Cells. *Chem. Eng. J.* **2020**, *389*, 124460.
(86) Nergiz, S. Z.; Gandra, N.; Tadepalli, S.; Singamaneni, S. Multifunctional Hybrid Nanopatches of Graphene Oxide and Gold Nanostars for Ultraefficient Photothermal Cancer Therapy. *ACS Appl. Mater. Interfaces* **2014**, *6*, 16395−16402.
(87) Chen, S.; Fan, J.; Qiu, W.; Liu, F.; Yan, G.; Zeng, X.; Zhang, X. A Cellular/Intranuclear Dual-Targeting Nanoplatform Based on Gold Nanostar for Accurate Tumor Photothermal Therapy. *J. Mater. Chem. B* **2018**, *6*, 1543−1551.
(88) Zhu, D.; Liu, Y.; Liu, M.; Liu, X.; Prasad, P. N.; Swihart, M. T. Galvanic Replacement Synthesis of Multi-Branched Gold Nanocrystals for Photothermal Cancer Therapy. *J. Mater. Chem. B* **2020**, *8*, 5491−5499.
(89) Du, B.; Zhang, W.; Tung, C.-H. Layer-by-Layer Construction of an Oxygen-Generating Photo-Responsive Nanomedicine for Enhanced Photothermal and Photodynamic Combination Therapy. *Chem. Commun.* **2019**, *55*, 5926−5929.
(90) Pan, Y.; Ma, X.; Liu, C.; Xing, J.; Zhou, S.; Parshad, B.; Schwerdtle, T.; Li, W.; Wu, A.; Haag, R. Retinoic Acid-Loaded Dendritic Polyglycerol-Conjugated Gold Nanostars for Targeted Photothermal Therapy in Breast Cancer Stem Cells. *ACS Nano* **2021**, *15*, 15069−15084.
(91) Valle, A. C.; Yeh, C.; Huang, Y. Near Infrared-Activatable Platinum-Decorated Gold Nanostars for Synergistic Photothermal/Ferroptotic Therapy in Combating Cancer Drug Resistance. *Adv. Healthcare Mater.* **2020**, *9*, 2000864.
(92) Kwon, H. J.; Byeon, Y.; Jeon, H. N.; Cho, S. H.; Han, H. D.; Shin, B. C. Gold Cluster-Labeled Thermosensitive Liposmes Enhance Triggered Drug Release in the Tumor Microenvironment by a Photothermal Effect. *J. Controlled Release* **2015**, *216*, 132−139.
(93) Panda, R.; Ranjan Dash, S.; Sagar Satapathy, S.; Nath Kundu, C.; Tripathy, J. Surface Functionalized Gold Nanorods for Plasmonic Photothermal Therapy. *Mater. Today: Proc.* **2021**, *47*, 1193−1196.
(94) Manivasagan, P.; Hoang, G.; Santha Moorthy, M.; Mondal, S.; Doan, V. H. M.; Kim, H.; Phan, T. T. V.; Nguyen, T. P.; Oh, J. Chitosan/Fucoidan Multilayer Coating of Gold Nanorods as Highly Efficient Near-Infrared Photothermal Agents for Cancer Therapy. *Carbohydr. Polym.* **2019**, *211*, 360−369.
(95) Zeng, F.; Peng, K.; Han, L.; Yang, J. Photothermal and Photodynamic Therapies via NIR-Activated Nanoagents in Combating Alzheimer's Disease. *ACS Biomater. Sci. Eng.* **2021**, *7*, 3573−3585.
(96) Zhao, J.; Huang, S.; Ravisankar, P.; Zhu, H. Two-Dimensional Nanomaterials for Photoinduced Antibacterial Applications. *ACS Appl. Bio Mater.* **2020**, *3*, 8188−8210.
(97) Feng, Y.; Chen, Q.; Yin, Q.; Pan, G.; Tu, Z.; Liu, L. Reduced Graphene Oxide Functionalized with Gold Nanostar Nanocomposites for Synergistically Killing Bacteria through Intrinsic Antimicrobial Activity and Photothermal Ablation. *ACS Appl. Bio Mater.* **2019**, *2*, 747−756.
(98) Zhang, R.; Yu, J.; Ma, K.; Ma, Y.; Wang, Z. Synergistic Chemo-Photothermal Antibacterial Effects of Polyelectrolyte-Functionalized Gold Nanomaterials. *ACS Appl. Bio Mater.* **2020**, *3*, 7168−7177.
(99) Rossi, F.; Khoo, E. H.; Su, X.; Thanh, N. T. K. Study of the Effect of Anisotropic Gold Nanoparticles on Plasmonic Coupling with a Photosensitizer for Antimicrobial Film. *ACS Appl. Bio Mater.* **2020**, *3*, 315−326.
(100) Bessa, L. J.; Peixoto de Almeida, M.; Eaton, P.; Pereira, E.; Gameiro, P. Silver Nanostars-Coated Surfaces with Potent Biocidal Properties. *Int. J. Environ. Res. Public Health* **2020**, *17*, 7891.
(101) Huynh, P. T.; Nguyen, G. D.; Tran, K. T. L.; Ho, T. M.; Duong, B. T.; Lam, V. Q.; Ngo, T. V. K. One-Pot, Surfactant-Free Synthesis of Gold Nanostars and Evaluation of Their Antibacterial Effects against Propionibacterium Acnes. *J. Nanomater.* **2021**, *2021*, 6650661.
(102) Wang, H.; Song, Z.; Li, S.; Wu, Y.; Han, H. One Stone with Two Birds: Functional Gold Nanostar for Targeted Combination Therapy of

Drug-Resistant *Staphylococcus Aureus* Infection. *ACS Appl. Mater. Interfaces* **2019**, *11*, 32659−32669.
(103) Rovati, D.; Albini, B.; Galinetto, P.; Grisoli, P.; Bassi, B.; Pallavicini, P.; Dacarro, G.; Taglietti, A. High Stability Thiol-Coated Gold Nanostars Monolayers with Photo-Thermal Antibacterial Activity and Wettability Control. *Nanomaterials* **2019**, *9*, 1288.
(104) Grisoli, P.; De Vita, L.; Milanese, C.; Taglietti, A.; Diaz Fernandez, Y.; Bouzin, M.; D'Alfonso, L.; Sironi, L.; Rossi, S.; Vigani, B.; Sperandeo, P.; Polissi, A.; Pallavicini, P. PVA Films with Mixed Silver Nanoparticles and Gold Nanostars for Intrinsic and Photothermal Antibacterial Action. *Nanomaterials* **2021**, *11*, 1387.
(105) Borzenkov, M.; Moros, M.; Tortiglione, C.; Bertoldi, S.; Contessi, N.; Faré, S.; Taglietti, A.; D'Agostino, A.; Pallavicini, P.; Collini, M.; Chirico, G. Fabrication of Photothermally Active Poly(Vinyl Alcohol) Films with Gold Nanostars for Antibacterial Applications. *Beilstein J. Nanotechnol.* **2018**, *9*, 2040−2048.
(106) Pallavicini, P.; Donà, A.; Taglietti, A.; Minzioni, P.; Patrini, M.; Dacarro, G.; Chirico, G.; Sironi, L.; Bloise, N.; Visai, L.; Scarabelli, L. Self-Assembled Monolayers of Gold Nanostars: A Convenient Tool for near-IR Photothermal Biofilm Eradication. *Chem. Commun.* **2014**, *50*, 1969−1971.
(107) Penders, J.; Stolzoff, M.; Hickey, D. J.; Andersson, M.; Webster, T. J. Shape-Dependent Antibacterial Effects of Non-Cytotoxic Gold Nanoparticles. *Int. J. Nanomedicine* **2017**, *12*, 2457−2468.
(108) Cao, M.; Chang, Z.; Tan, J.; Wang, X.; Zhang, P.; Lin, S.; Liu, J.; Li, A. Superoxide Radical-Mediated Self-Synthesized Au/MoO_{3-x} Hybrids with Enhanced Peroxidase-like Activity and Photothermal Effect for Anti-MRSA Therapy. *ACS Appl. Mater. Interfaces* **2022**, *14*, 13025−13037.
(109) Wijesiri, N.; Ozkaya-Ahmadov, T.; Wang, P.; Zhang, J.; Tang, H.; Yu, X.; Ayres, N.; Zhang, P. Photodynamic Inactivation of Multidrug-Resistant *Staphylococcus Aureus* Using Hybrid Photosensitizers Based on Amphiphilic Block Copolymer-Functionalized Gold Nanoparticles. *ACS Omega* **2017**, *2*, 5364−5369.
(110) Tran, H.-V.; Ngo, N. M.; Medhi, R.; Srinoi, P.; Liu, T.; Rittikulsittichai, S.; Lee, T. R. Multifunctional Iron Oxide Magnetic Nanoparticles for Biomedical Applications: A Review. *Materials* **2022**, *15*, 503.
(111) van de Looij, S. M.; Hebels, E. R.; Viola, M.; Hembury, M.; Oliveira, S.; Vermonden, T. Gold Nanoclusters: Imaging, Therapy, and Theranostic Roles in Biomedical Applications. *Bioconjugate Chem.* **2022**, *33*, 4−23.
(112) Jia, X.; Xu, W.; Ye, Z.; Wang, Y.; Dong, Q.; Wang, E.; Li, D.; Wang, J. Functionalized Graphene@Gold Nanostar/Lipid for Pancreatic Cancer Gene and Photothermal Synergistic Therapy under Photoacoustic/Photothermal Imaging Dual-Modal Guidance. *Small* **2020**, *16*, 2003707.
(113) Yan, R.; Chen, J.; Wang, J.; Rao, J.; Du, X.; Liu, Y.; Zhang, L.; Qiu, L.; Liu, B.; Zhao, Y.; Jiang, P.; Chen, C.; Li, Y. A NanoFlare-Based Strategy for In Situ Tumor Margin Demarcation and Neoadjuvant Gene/Photothermal Therapy. *Small* **2018**, *14*, 1802745.
(114) Zhang, L.; Liu, C.; Gao, Y.; Li, Z.; Xing, J.; Ren, W.; Zhang, L.; Li, A.; Lu, G.; Wu, A.; Zeng, L. ZD2-Engineered Gold Nanostar@Metal-Organic Framework Nanoprobes for T_1 -Weighted Magnetic Resonance Imaging and Photothermal Therapy Specifically Toward Triple-Negative Breast Cancer. *Adv. Healthcare Mater.* **2018**, *7*, 1801144.
(115) Wu, C.; Li, D.; Wang, L.; Guan, X.; Tian, Y.; Yang, H.; Li, S.; Liu, Y. Single Wavelength Light-Mediated, Synergistic Bimodal Cancer Photoablation and Amplified Photothermal Performance by Graphene/Gold Nanostar/Photosensitizer Theranostics. *Acta Biomaterialia* **2017**, *53*, 631−642.
(116) Tomitaka, A.; Arami, H.; Ahmadivand, A.; Pala, N.; McGoron, A. J.; Takemura, Y.; Febo, M.; Nair, M. Magneto-Plasmonic Nanostars for Image-Guided and NIR-Triggered Drug Delivery. *Sci. Rep.* **2020**, *10*, 10115.
(117) Wang, J.; Zhou, Z.; Zhang, F.; Xu, H.; Chen, W.; Jiang, T. A Novel Nanocomposite Based on Fluorescent Turn-on Gold Nanostars for near-Infrared Photothermal Therapy and Self-Theranostic Caspase-3 Imaging of Glioblastoma Tumor Cell. *Colloids Surf., B* **2018**, *170*, 303−311.
(118) An, J.; Yang, X.-Q.; Cheng, K.; Song, X.-L.; Zhang, L.; Li, C.; Zhang, X.-S.; Xuan, Y.; Song, Y.-Y.; Fang, B.-Y.; Hou, X.-L.; Zhao, Y.-D.; Liu, B. In Vivo Computed Tomography/Photoacoustic Imaging and NIR-Triggered Chemo−Photothermal Combined Therapy Based on a Gold Nanostar-, Mesoporous Silica-, and Thermosensitive Liposome-Composited Nanoprobe. *ACS Appl. Mater. Interfaces* **2017**, *9*, 41748−41759.
(119) Tan, H.; Hou, N.; Liu, Y.; Liu, B.; Cao, W.; Zheng, D.; Li, W.; Liu, Y.; Xu, B.; Wang, Z.; Cui, D. CD133 Antibody Targeted Delivery of Gold Nanostars Loading IR820 and Docetaxel for Multimodal Imaging and Near-Infrared Photodynamic/Photothermal/Chemotherapy against Castration Resistant Prostate Cancer. *Nanomedicine* **2020**, *27*, 102192.
(120) Fales, A. M.; Crawford, B. M.; Vo-Dinh, T. Folate Receptor-Targeted Theranostic Nanoconstruct for Surface-Enhanced Raman Scattering Imaging and Photodynamic Therapy. *ACS Omega* **2016**, *1*, 730−735.
(121) Barbosa, S.; Topete, A.; Alatorre-Meda, M.; Villar-Alvarez, E. M.; Pardo, A.; Alvarez-Lorenzo, C.; Concheiro, A.; Taboada, P.; Mosquera, V. Targeted Combinatorial Therapy Using Gold Nanostars as Theranostic Platforms. *J. Phys. Chem. C* **2014**, *118*, 26313−26323.
(122) Li, S.; Jiang, Q.; Liu, Y.; Wang, W.; Yu, W.; Wang, F.; Liu, X. Precision Spherical Nucleic Acids Enable Sensitive FEN1 Imaging and Controllable Drug Delivery for Cancer-Specific Therapy. *Anal. Chem.* **2021**, *93*, 11275−11283.
(123) Li, B.; Zhou, Q.; Wang, H.; Zha, Y.; Zheng, P.; Yang, T.; Ma, D.; Qiu, L.; Xu, X.; Hu, Y.; Roig, A.; Yu, S.; Xue, W. Mitochondria-Targeted Magnetic Gold Nanoheterostructure for Multi-Modal Imaging Guided Photothermal and Photodynamic Therapy of Triple-Negative Breast Cancer. *Chem. Eng. J.* **2021**, *403*, 126364.
(124) Pramanik, A.; Gao, Y.; Patibandla, S.; Mitra, D.; McCandless, M. G.; Fassero, L. A.; Gates, K.; Tandon, R.; Ray, P. C. Aptamer Conjugated Gold Nanostar-Based Distance-Dependent Nanoparticle Surface Energy Transfer Spectroscopy for Ultrasensitive Detection and Inactivation of Corona Virus. *J. Phys. Chem. Lett.* **2021**, *12*, 2166−2171.
(125) Xu, P.; Ning, P.; Wang, J.; Qin, Y.; Liang, F.; Cheng, Y. Precise Control of Apoptosis *via* Gold Nanostars for Dose Dependent Photothermal Therapy of Melanoma. *J. Mater. Chem. B* **2019**, *7*, 6934−6944.
(126) Tian, Y.; Zhang, Y.; Teng, Z.; Tian, W.; Luo, S.; Kong, X.; Su, X.; Tang, Y.; Wang, S.; Lu, G. PH-Dependent Transmembrane Activity of Peptide-Functionalized Gold Nanostars for Computed Tomography/Photoacoustic Imaging and Photothermal Therapy. *ACS Appl. Mater. Interfaces* **2017**, *9*, 2114−2122.
(127) Li, Z.; Yang, F.; Wu, D.; Liu, Y.; Gao, Y.; Lian, H.; Zhang, H.; Yin, Z.; Wu, A.; Zeng, L. Ce6-Conjugated and Polydopamine-Coated Gold Nanostars with Enhanced Photoacoustic Imaging and Photothermal/Photodynamic Therapy to Inhibit Lung Metastasis of Breast Cancer. *Nanoscale* **2020**, *12*, 22173−22184.
(128) Du, X.; Wang, W.; Wu, C.; Jia, B.; Li, W.; Qiu, L.; Jiang, P.; Wang, J.; Li, Y.-Q. Enzyme-Responsive Turn-on Nanoprobes for *in Situ* Fluorescence Imaging and Localized Photothermal Treatment of Multidrug-Resistant Bacterial Infections. *J. Mater. Chem. B* **2020**, *8*, 7403−7412.
(129) Han, X.; Xu, Y.; Li, Y.; Zhao, X.; Zhang, Y.; Min, H.; Qi, Y.; Anderson, G. J.; You, L.; Zhao, Y.; Nie, G. An Extendable Star-Like Nanoplatform for Functional and Anatomical Imaging-Guided Photothermal Oncotherapy. *ACS Nano* **2019**, *13*, 4379−4391.
(130) Deng, X.; Liang, S.; Cai, X.; Huang, S.; Cheng, Z.; Shi, Y.; Pang, M.; Ma, P.; Lin, J. Yolk−Shell Structured Au Nanostar@Metal−Organic Framework for Synergistic Chemo-Photothermal Therapy in the Second Near-Infrared Window. *Nano Lett.* **2019**, *19*, 6772−6780.
(131) Hu, P.; Hou, X.; Yu, X.; Wei, X.; Li, Y.; Yang, D.; Jiang, X. Folic Acid-Conjugated Gold Nanostars for Computed Tomography Imaging and Photothermal/Radiation Combined Therapy. *ACS Appl. Bio Mater.* **2021**, *4*, 4862−4871.

https://doi.org/10.1021/acsanm.2c02533
ACS Appl. Nano Mater. 2022, 5, 14051−14091

(132) Li, B.; Niu, X.; Xie, M.; Luo, F.; Huang, X.; You, Z. Tumor-Targeting Multifunctional Nanoprobe for Enhanced Photothermal/Photodynamic Therapy of Liver Cancer. *Langmuir* **2021**, *37*, 8064−8072.
(133) Espinosa, A.; Reguera, J.; Curcio, A.; Muñoz-Noval, Á.; Kuttner, C.; Van de Walle, A.; Liz-Marzán, L. M.; Wilhelm, C. Janus Magnetic-Plasmonic Nanoparticles for Magnetically Guided and Thermally Activated Cancer Therapy. *Small* **2020**, *16*, 1904960.
(134) del Valle, A. C.; Su, C.-K.; Sun, Y.-C.; Huang, Y.-F. NIR-Cleavable Drug Adducts of Gold Nanostars for Overcoming Multidrug-Resistant Tumors. *Biomater. Sci.* **2020**, *8*, 1934−1950.
(135) Sasidharan, S.; Bahadur, D.; Srivastava, R. Rapid, One-Pot, Protein-Mediated Green Synthesis of Gold Nanostars for Computed Tomographic Imaging and Photothermal Therapy of Cancer. *ACS Sustainable Chem. Eng.* **2017**, *5*, 10163−10175.
(136) Zhi, X.; Liu, Y.; Lin, L.; Yang, M.; Zhang, L.; Zhang, L.; Liu, Y.; Alfranca, G.; Ma, L.; Zhang, Q.; Fu, H.; Conde, J.; Ding, X.; Chen, D.; Ni, J.; Song, J.; Cui, D. Oral pH Sensitive GNS@ab Nanoprobes for Targeted Therapy of Helicobacter Pylori without Disturbance Gut Microbiome. *Nanomed. Nanotechnol. Biol. Med.* **2019**, *20*, 102019.
(137) Wang, W.; Hao, C.; Sun, M.; Xu, L.; Xu, C.; Kuang, H. Spiky Fe_3O_4@Au Supraparticles for Multimodal In Vivo Imaging. *Adv. Funct. Mater.* **2018**, *28*, 1800310.
(138) Nguyen, M. D.; Tran, H.-V.; Xu, S.; Lee, T. R. Fe_3O_4 Nanoparticles: Structures, Synthesis, Magnetic Properties, Surface Functionalization, and Emerging Applications. *Appl. Sci.* **2021**, *11*, 11301.
(139) Lee, C.; Lawrie, B.; Pooser, R.; Lee, K.-G.; Rockstuhl, C.; Tame, M. Quantum Plasmonic Sensors. *Chem. Rev.* **2021**, *121*, 4743−4804.
(140) Tang, L.; Li, J. Plasmon-Based Colorimetric Nanosensors for Ultrasensitive Molecular Diagnostics. *ACS Sens.* **2017**, *2*, 857−875.
(141) Song, L.; Chen, J.; Xu, B. B.; Huang, Y. Flexible Plasmonic Biosensors for Healthcare Monitoring: Progress and Prospects. *ACS Nano* **2021**, *15*, 18822−18847.
(142) Tokel, O.; Inci, F.; Demirci, U. Advances in Plasmonic Technologies for Point of Care Applications. *Chem. Rev.* **2014**, *114*, 5728−5752.
(143) Kim, S.; Lee, H. J. Gold Nanostar Enhanced Surface Plasmon Resonance Detection of an Antibiotic at Attomolar Concentrations via an Aptamer-Antibody Sandwich Assay. *Anal. Chem.* **2017**, *89*, 6624−6630.
(144) Jana, D.; Matti, C.; He, J.; Sagle, L. Capping Agent-Free Gold Nanostars Show Greatly Increased Versatility and Sensitivity for Biosensing. *Anal. Chem.* **2015**, *87*, 3964−3972.
(145) Bhamidipati, M.; Cho, H.-Y.; Lee, K.-B.; Fabris, L. SERS-Based Quantification of Biomarker Expression at the Single Cell Level Enabled by Gold Nanostars and Truncated Aptamers. *Bioconjugate Chem.* **2018**, *29*, 2970−2981.
(146) Wong, Y. L.; Kang, W. C. M.; Reyes, M.; Teo, J. W. P.; Kah, J. C. Y. Rapid Detection of Carbapenemase-Producing Enterobacteriacae Based on Surface-Enhanced Raman Spectroscopy with Gold Nanostars. *ACS Infect. Dis.* **2020**, *6*, 947−953.
(147) Reyes, M.; Piotrowski, M.; Ang, S. K.; Chan, J.; He, S.; Chu, J. J. H.; Kah, J. C. Y. Exploiting the Anti-Aggregation of Gold Nanostars for Rapid Detection of Hand, Foot, and Mouth Disease Causing Enterovirus 71 Using Surface-Enhanced Raman Spectroscopy. *Anal. Chem.* **2017**, *89*, 5373−5381.
(148) Liu, Y.; Pan, M.; Wang, W.; Jiang, Q.; Wang, F.; Pang, D.-W.; Liu, X. Plasmonic and Photothermal Immunoassay via Enzyme-Triggered Crystal Growth on Gold Nanostars. *Anal. Chem.* **2019**, *91*, 2086−2092.
(149) He, S.; Kyaw, Y. M. E.; Tan, E. K. M.; Bekale, L.; Kang, M. W. C.; Kim, S. S.-Y.; Tan, I.; Lam, K.-P.; Kah, J. C. Y. Quantitative and Label-Free Detection of Protein Kinase A Activity Based on Surface-Enhanced Raman Spectroscopy with Gold Nanostars. *Anal. Chem.* **2018**, *90*, 6071−6080.
(150) Liu, Y.; Lyu, N.; Rajendran, V. K.; Piper, J.; Rodger, A.; Wang, Y. Sensitive and Direct DNA Mutation Detection by Surface-Enhanced Raman Spectroscopy Using Rational Designed and Tunable Plasmonic Nanostructures. *Anal. Chem.* **2020**, *92*, 5708−5716.
(151) Sánchez-Purrà, M.; Carré-Camps, M.; de Puig, H.; Bosch, I.; Gehrke, L.; Hamad-Schifferli, K. Surface-Enhanced Raman Spectroscopy-Based Sandwich Immunoassays for Multiplexed Detection of Zika and Dengue Viral Biomarkers. *ACS Infect. Dis.* **2017**, *3*, 767−776.
(152) Su, Y.; Wu, D.; Chen, J.; Chen, G.; Hu, N.; Wang, H.; Wang, P.; Han, H.; Li, G.; Wu, Y. Ratiometric Surface Enhanced Raman Scattering Immunosorbent Assay of Allergenic Proteins via Covalent Organic Framework Composite Material Based Nanozyme Tag Triggered Raman Signal "Turn-on" and Amplification. *Anal. Chem.* **2019**, *91*, 11687−11695.
(153) Gao, X.; Boryczka, J.; Kasani, S.; Wu, N. Enabling Direct Protein Detection in a Drop of Whole Blood with an "On-Strip" Plasma Separation Unit in a Paper-Based Lateral Flow Strip. *Anal. Chem.* **2021**, *93*, 1326−1332.
(154) Wang, H.-N.; Crawford, B. M.; Fales, A. M.; Bowie, M. L.; Seewaldt, V. L.; Vo-Dinh, T. Multiplexed Detection of MicroRNA Biomarkers Using SERS-Based Inverse Molecular Sentinel (IMS) Nanoprobes. *J. Phys. Chem. C* **2016**, *120*, 21047−21055.
(155) Strobbia, P.; Ran, Y.; Crawford, B. M.; Cupil-Garcia, V.; Zentella, R.; Wang, H.-N.; Sun, T.-P.; Vo-Dinh, T. Inverse Molecular Sentinel-Integrated Fiberoptic Sensor for Direct and *in Situ* Detection of MiRNA Targets. *Anal. Chem.* **2019**, *91*, 6345−6352.
(156) Srivastav, S.; Dankov, A.; Adanalic, M.; Grzeschik, R.; Tran, V.; Pagel-Wieder, S.; Gessler, F.; Spreitzer, I.; Scholz, T.; Schnierle, B.; Anastasiou, O. E.; Dittmer, U.; Schlücker, S. Rapid and Sensitive SERS-Based Lateral Flow Test for SARS-CoV2-Specific IgM/IgG Antibodies. *Anal. Chem.* **2021**, *93*, 12391−12399.
(157) Carrasco, S.; Benito-Peña, E.; Navarro-Villoslada, F.; Langer, J.; Sanz-Ortiz, M. N.; Reguera, J.; Liz-Marzán, L. M.; Moreno-Bondi, M. C. Multibranched Gold−Mesoporous Silica Nanoparticles Coated with a Molecularly Imprinted Polymer for Label-Free Antibiotic Surface-Enhanced Raman Scattering Analysis. *Chem. Mater.* **2016**, *28*, 7947−7954.
(158) Pan, X.; Li, L.; Lin, H.; Tan, J.; Wang, H.; Liao, M.; Chen, C.; Shan, B.; Chen, Y.; Li, M. A Graphene Oxide-Gold Nanostar Hybrid Based-Paper Biosensor for Label-Free SERS Detection of Serum Bilirubin for Diagnosis of Jaundice. *Biosens. Bioelectron.* **2019**, *145*, 111713.
(159) Wen, S.; Su, Y.; Wu, R.; Zhou, S.; Min, Q.; Fan, G.-C.; Jiang, L.-P.; Song, R.-B.; Zhu, J.-J. Plasmonic Au Nanostar Raman Probes Coupling with Highly Ordered TiO2/Au Nanotube Arrays as the Reliable SERS Sensing Platform for Chronic Myeloid Leukemia Drug Evaluation. *Biosens. Bioelectron.* **2018**, *117*, 260−266.
(160) Villa, J. E. L.; Garcia, I.; Jimenez de Aberasturi, D.; Pavlov, V.; Sotomayor, M. D. P. T.; Liz-Marzán, L. M. SERS-Based Immunoassay for Monitoring Cortisol-Related Disorders. *Biosens. Bioelectron.* **2020**, *165*, 112418.
(161) Hashemi, S. A.; Golab Behbahan, N. G.; Bahrani, S.; Mousavi, S. M.; Gholami, A.; Ramakrishna, S.; Firoozsani, M.; Moghadami, M.; Lankarani, K. B.; Omidifar, N. Ultra-Sensitive Viral Glycoprotein Detection NanoSystem toward Accurate Tracing SARS-CoV-2 in Biological/Non-Biological Media. *Biosens. Bioelectron.* **2021**, *171*, 112731.
(162) Sanchez, J. E.; Jaramillo, S. A.; Settles, E.; Velazquez Salazar, J. J.; Lehr, A.; Gonzalez, J.; Rodríguez Aranda, C.; Navarro-Contreras, H. R.; Raniere, M. O.; Harvey, M.; Wagner, D. M.; Koppisch, A.; Kellar, R.; Keim, P.; Jose Yacaman, M. Detection of SARS-CoV-2 and Its S and N Proteins Using Surface Enhanced Raman Spectroscopy. *RSC Adv.* **2021**, *11*, 25788−25794.
(163) Alireza Hashemi, S.; Bahrani, S.; Mojtaba Mousavi, S.; Omidifar, N.; Ghaleh Golab Behbahan, N.; Arjmand, M.; Ramakrishna, S.; Bagheri Lankarani, K.; Moghadami, M.; Shokripour, M.; Firoozsani, M.; Chiang, W.-H. Ultra-Precise Label-Free Nanosensor Based on Integrated Graphene with Au Nanostars toward Direct Detection of IgG Antibodies of SARS-CoV-2 in Blood. *J. Electroanal. Chem.* **2021**, *894*, 115341.

https://doi.org/10.1021/acsanm.2c02533
ACS Appl. Nano Mater. 2022, 5, 14051−14091

(164) Maltez-da Costa, M.; de la Escosura-Muñiz, A.; Nogués, C.; Barrios, L.; Ibáñez, E.; Merkoçi, A. Detection of Circulating Cancer Cells Using Electrocatalytic Gold Nanoparticles. *Small* **2012**, *8*, 3605−3612.
(165) Wang, J.; Xie, H.; Ding, C. Designed Co-DNA-Locker and Ratiometric SERS Sensing for Accurate Detection of Exosomes Based on Gold Nanorod Arrays. *ACS Appl. Mater. Interfaces* **2021**, *13*, 32837−32844.
(166) Tittl, A.; Giessen, H.; Liu, N. Plasmonic Gas and Chemical Sensing. *Nanophotonics* **2014**, *3*, 157−180.
(167) Kumar, V.; Patil, V.; Apte, A.; Harale, N.; Patil, P.; Kulkarni, S. Ultrasensitive Gold Nanostar−Polyaniline Composite for Ammonia Gas Sensing. *Langmuir* **2015**, *31*, 13247−13256.
(168) Mueller, M.; Tebbe, M.; Andreeva, D. V.; Karg, M.; Alvarez Puebla, R. A.; Pazos Perez, N.; Fery, A. Large-Area Organization of PNIPAM-Coated Nanostars as SERS Platforms for Polycyclic Aromatic Hydrocarbons Sensing in Gas Phase. *Langmuir* **2012**, *28*, 9168−9173.
(169) Li, M.; Lin, H.; Paidi, S. K.; Mesyngier, N.; Preheim, S.; Barman, I. A Fluorescence and Surface-Enhanced Raman Spectroscopic Dual-Modal Aptasensor for Sensitive Detection of Cyanotoxins. *ACS Sens.* **2020**, *5*, 1419−1426.
(170) Zhao, X.; Campbell, S.; Wallace, G. Q.; Claing, A.; Bazuin, C. G.; Masson, J.-F. Branched Au Nanoparticles on Nanofibers for Surface-Enhanced Raman Scattering Sensing of Intracellular pH and Extracellular pH Gradients. *ACS Sens.* **2020**, *5*, 2155−2167.
(171) Li, M.; Paidi, S. K.; Sakowski, E.; Preheim, S.; Barman, I. Ultrasensitive Detection of Hepatotoxic Microcystin Production from Cyanobacteria Using Surface-Enhanced Raman Scattering Immunosensor. *ACS Sens.* **2019**, *4*, 1203−1210.
(172) Guo, J.; Liu, Y.; Yang, Y.; Li, Y.; Wang, R.; Ju, H. A Filter Supported Surface-Enhanced Raman Scattering "Nose" for Point-of-Care Monitoring of Gaseous Metabolites of Bacteria. *Anal. Chem.* **2020**, *92*, 5055−5063.
(173) Amjadi, M.; Abolghasemi-Fakhri, Z. Gold Nanostar-Enhanced Chemiluminescence Probe for Highly Sensitive Detection of Cu(II) Ions. *Sens. Actuators, B* **2018**, *257*, 629−634.
(174) Hongxia, C.; Ji, H.; Zaijun, L.; Ruiyi, L.; Yongqiang, Y.; Xiulan, S. Electrochemical Aptasensor for Detection of Acetamiprid in Vegetables with Graphene Aerogel-Glutamic Acid Functionalized Graphene Quantum Dot/Gold Nanostars as Redox Probe with Catalyst. *Sens. Actuators, B* **2019**, *298*, 126866.
(175) Dutta, S.; Strack, G.; Kurup, P. Gold Nanostar Electrodes for Heavy Metal Detection. *Sens. Actuators, B* **2019**, *281*, 383−391.
(176) Lin, L.-K.; Stanciu, L. A. Bisphenol A Detection Using Gold Nanostars in a SERS Improved Lateral Flow Immunochromatographic Assay. *Sens. Actuators, B* **2018**, *276*, 222−229.
(177) Zhao, Y.; Li, X.; Liu, Y.; Zhang, L.; Wang, F.; Lu, Y. High Performance Surface-Enhanced Raman Scattering Sensing Based on Au Nanoparticle-Monolayer Graphene-Ag Nanostar Array Hybrid System. *Sens. Actuators, B* **2017**, *247*, 850−857.
(178) Cheng, N.; Song, Y.; Fu, Q.; Du, D.; Luo, Y.; Wang, Y.; Xu, W.; Lin, Y. Aptasensor Based on Fluorophore-Quencher Nano-Pair and Smartphone Spectrum Reader for on-Site Quantification of Multi-Pesticides. *Biosens. Bioelectron.* **2018**, *117*, 75−83.
(179) Wang, S.; Huang, X.; An, Q.; Zhou, R.; Xu, W.; Xu, D.; Lin, Q.; Cao, X. Gold Nanostar as an Ultrasensitive Colorimetric Probe for Picomolar Detection of Lead Ion. *Anal. Chim. Acta* **2021**, *1160*, 338380.
(180) Logan, N.; Lou-Franco, J.; Elliott, C.; Cao, C. Catalytic Gold Nanostars for SERS-Based Detection of Mercury Ions (Hg^{2+}) with Inverse Sensitivity. *Environ. Sci.: Nano* **2021**, *8*, 2718−2730.
(181) Oliveira, M. J.; Quaresma, P.; Peixoto de Almeida, M.; Araújo, A.; Pereira, E.; Fortunato, E.; Martins, R.; Franco, R.; Águas, H. Office Paper Decorated with Silver Nanostars - an Alternative Cost Effective Platform for Trace Analyte Detection by SERS. *Sci. Rep.* **2017**, *7*, 2480.
(182) Lu, G.; Johns, A. J.; Neupane, B.; Phan, H. T.; Cwiertny, D. M.; Forbes, T. Z.; Haes, A. J. Matrix-Independent Surface-Enhanced Raman Scattering Detection of Uranyl Using Electrospun Amidoximated Polyacrylonitrile Mats and Gold Nanostars. *Anal. Chem.* **2018**, *90*, 6766−6772.
(183) Meng, X.; Dyer, J.; Huo, Y.; Jiang, C. Greater SERS Activity of Ligand-Stabilized Gold Nanostars with Sharp Branches. *Langmuir* **2020**, *36*, 3558−3564.
(184) Ndokoye, P.; Ke, J.; Liu, J.; Zhao, Q.; Li, X. L-Cysteine-Modified Gold Nanostars for SERS-Based Copper Ions Detection in Aqueous Media. *Langmuir* **2014**, *30*, 13491−13497.
(185) Gopalakrishnan, A.; Chirumamilla, M.; De Angelis, F.; Toma, A.; Zaccaria, R. P.; Krahne, R. Bimetallic 3D Nanostar Dimers in Ring Cavities: Recyclable and Robust Surface-Enhanced Raman Scattering Substrates for Signal Detection from Few Molecules. *ACS Nano* **2014**, *8*, 7986−7994.
(186) Park, S.; Lee, J.; Ko, H. Transparent and Flexible Surface-Enhanced Raman Scattering (SERS) Sensors Based on Gold Nanostar Arrays Embedded in Silicon Rubber Film. *ACS Appl. Mater. Interfaces* **2017**, *9*, 44088−44095.
(187) Phan, H. T.; Vinson, C.; Haes, A. J. Gold Nanostar Spatial Distribution Impacts the Surface-Enhanced Raman Scattering Detection of Uranyl on Amidoximated Polymers. *Langmuir* **2021**, *37*, 4891−4899.
(188) Tanwar, S.; Haldar, K. K.; Sen, T. DNA Origami Directed Au Nanostar Dimers for Single-Molecule Surface-Enhanced Raman Scattering. *J. Am. Chem. Soc.* **2017**, *139*, 17639−17648.
(189) Su, L.; Hu, H.; Tian, Y.; Jia, C.; Wang, L.; Zhang, H.; Wang, J.; Zhang, D. Highly Sensitive Colorimetric/Surface-Enhanced Raman Spectroscopy Immunoassay Relying on a Metallic Core−Shell Au/Au Nanostar with Clenbuterol as a Target Analyte. *Anal. Chem.* **2021**, *93*, 8362−8369.
(190) Yang, A.-M.; Lo, K.; Zheng, T.-Z.; Yang, J.-L.; Bai, Y.-N.; Feng, Y.-Q.; Cheng, N.; Liu, S.-M. Environmental Heavy Metals and Cardiovascular Diseases: Status and Future Direction. *Chronic Dis. Transl. Med.* **2020**, *6*, 251−259.
(191) Ijomone, O. M.; Ifenatuoha, C. W.; Aluko, O. M.; Ijomone, O. K.; Aschner, M. The Aging Brain: Impact of Heavy Metal Neurotoxicity. *Crit. Rev. Toxicol.* **2020**, *50*, 801−814.
(192) Domínguez-González, R.; González Varela, L.; Bermejo-Barrera, P. Functionalized Gold Nanoparticles for the Detection of Arsenic in Water. *Talanta* **2014**, *118*, 262−269.
(193) Kongor, A.; Panchal, M.; Athar, M.; Vora, M.; Verma, N.; Pandya, A.; Jha, P. C.; Bhadresha, K.; Rawal, R.; Jain, V. Colorimetric and Electrochemical Sensing of As(III) Using Calix[4]Pyrrole Capped Gold Nanoparticles and Evaluation of Its Cytotoxic Activity. *J. Incl. Phenom. Macrocycl. Chem.* **2020**, *98*, 29−41.
(194) Chemnasiri, W.; Hernandez, F. E. Gold Nanorod-Based Mercury Sensor Using Functionalized Glass Substrates. *Sens. Actuators, B* **2012**, *173*, 322−328.
(195) Huang, D.; Hu, T.; Chen, N.; Zhang, W.; Di, J. Development of Silver/Gold Nanocages onto Indium Tin Oxide Glass as a Reagentless Plasmonic Mercury Sensor. *Anal. Chim. Acta* **2014**, *825*, 51−56.
(196) Priyadarshini, E.; Pradhan, N. Metal-Induced Aggregation of Valine Capped Gold Nanoparticles: An Efficient and Rapid Approach for Colorimetric Detection of Pb^{2+} Ions. *Sci. Rep.* **2017**, *7*, 9278.
(197) Xu, Q.; Guo, X.; Xu, L.; Ying, Y.; Wu, Y.; Wen, Y.; Yang, H. Template-Free Synthesis of SERS-Active Gold Nanopopcorn for Rapid Detection of Chlorpyrifos Residues. *Sens. Actuators, B* **2017**, *241*, 1008−1013.
(198) Chadha, R.; Das, A.; Lobo, J.; Meenu, V. O.; Paul, A.; Ballal, A.; Maiti, N. γ-Cyclodextrin Capped Silver and Gold Nanoparticles as Colorimetric and Raman Sensor for Detecting Traces of Pesticide "Chlorpyrifos" in Fruits and Vegetables. *Colloids Surf., A* **2022**, *641*, 128558.
(199) Arvand, M.; Dehsaraei, M. Amperometric Determination of Diazinon by Gold Nanorods/ds-DNA/Graphene Oxide Sandwich-Modified Electrode. *Ionics* **2018**, *24*, 2445−2454.
(200) Liu, J.; Ye, L. Y.; Zhang, Y.; Yang, H.; Zhou, L.; Luo, E.; Lei, J. Nonenzymatic Target-Driven DNA Nanomachine for Monitoring Malathion Contamination in Living Cells and Bioaccumulation in Foods. *Anal. Chem.* **2022**, *94* (14), 5667−5673.
(201) Li, D.; Wang, S.; Wang, L.; Zhang, H.; Hu, J. A Simple Colorimetric Probe Based on Anti-Aggregation of AuNPs for Rapid and

https://doi.org/10.1021/acsanm.2c02533
ACS Appl. Nano Mater. 2022, 5, 14051−14091

Sensitive Detection of Malathion in Environmental Samples. *Anal Bioanal Chem.* **2019**, *411*, 2645−2652.
(202) Willets, K. A.; Wilson, A. J.; Sundaresan, V.; Joshi, P. B. Super-Resolution Imaging and Plasmonics. *Chem. Rev.* **2017**, *117*, 7538−7582.
(203) Osinkina, L.; Lohmüller, T.; Jäckel, F.; Feldmann, J. Synthesis of Gold Nanostar Arrays as Reliable, Large-Scale, Homogeneous Substrates for Surface-Enhanced Raman Scattering Imaging and Spectroscopy. *J. Phys. Chem. C* **2013**, *117*, 22198−22202.
(204) Serrano-Montes, A. B.; Langer, J.; Henriksen-Lacey, M.; Jimenez de Aberasturi, D.; Solís, D. M.; Taboada, J. M.; Obelleiro, F.; Sentosun, K.; Bals, S.; Bekdemir, A.; Stellacci, F.; Liz-Marzán, L. M. Gold Nanostar-Coated Polystyrene Beads as Multifunctional Nanoprobes for SERS Bioimaging. *J. Phys. Chem. C* **2016**, *120*, 20860−20868.
(205) Geers, C.; Rodríguez-Lorenzo, L.; Placencia Peña, M. I.; Brodard, P.; Volkmer, T.; Rothen-Rutishauser, B.; Petri-Fink, A. Distribution of Silica-Coated Silver/Gold Nanostars in Soft- and Hardwood Applying SERS-Based Imaging. *Langmuir* **2016**, *32*, 274−283.
(206) Nguyen, V.-P.; Li, Y.; Henry, J.; Zhang, W.; Aaberg, M.; Jones, S.; Qian, T.; Wang, X.; Paulus, Y. M. Plasmonic Gold Nanostar-Enhanced Multimodal Photoacoustic Microscopy and Optical Coherence Tomography Molecular Imaging To Evaluate Choroidal Neovascularization. *ACS Sens.* **2020**, *5*, 3070−3081.
(207) Ou, Y.-C.; Wen, X.; Johnson, C. A.; Shae, D.; Ayala, O. D.; Webb, J. A.; Lin, E. C.; DeLapp, R. C.; Boyd, K. L.; Richmond, A.; Mahadevan-Jansen, A.; Rafat, M.; Wilson, J. T.; Balko, J. M.; Tantawy, M. N.; Vilgelm, A. E.; Bardhan, R. Multimodal Multiplexed Immunoimaging with Nanostars to Detect Multiple Immunomarkers and Monitor Response to Immunotherapies. *ACS Nano* **2020**, *14*, 651−663.
(208) de Albuquerque, C. D. L.; Schultz, Z. D. Super-Resolution Surface-Enhanced Raman Scattering Imaging of Single Particles in Cells. *Anal. Chem.* **2020**, *92*, 9389−9398.
(209) Li, C.; Chen, P.; Wang, Z.; Ma, X. A DNAzyme-Gold Nanostar Probe for SERS-Fluorescence Dual-Mode Detection and Imaging of Calcium Ions in Living Cells. *Sens. Actuators, B* **2021**, *347*, 130596.
(210) Harmsen, S.; Huang, R.; Wall, M. A.; Karabeber, H.; Samii, J. M.; Spaliviero, M.; White, J. R.; Monette, S.; O'Connor, R.; Pitter, K. L.; Sastra, S. A.; Saborowski, M.; Holland, E. C.; Singer, S.; Olive, K. P.; Lowe, S. W.; Blasberg, R. G.; Kircher, M. F. Surface-Enhanced Resonance Raman Scattering Nanostars for High-Precision Cancer Imaging. *Sci. Transl. Med.* **2015**, *7*, 271ra7.
(211) Reguera, J.; Jiménez de Aberasturi, D.; Henriksen-Lacey, M.; Langer, J.; Espinosa, A.; Szczupak, B.; Wilhelm, C.; Liz-Marzán, L. M. Janus Plasmonic−Magnetic Gold−Iron Oxide Nanoparticles as Contrast Agents for Multimodal Imaging. *Nanoscale* **2017**, *9*, 9467−9480.
(212) Wiercigroch, E.; Stepula, E.; Mateuszuk, L.; Zhang, Y.; Baranska, M.; Chlopicki, S.; Schlücker, S.; Malek, K. ImmunoSERS Microscopy for the Detection of Smooth Muscle Cells in Atherosclerotic Plaques. *Biosens. Bioelectron.* **2019**, *133*, 79−85.
(213) Theodorou, I. G.; Ruenraroengsak, P.; Gonzalez-Carter, D. A.; Jiang, Q.; Yagüe, E.; Aboagye, E. O.; Coombes, R. C.; Porter, A. E.; Ryan, M. P.; Xie, F. Towards Multiplexed Near-Infrared Cellular Imaging Using Gold Nanostar Arrays with Tunable Fluorescence Enhancement. *Nanoscale* **2019**, *11*, 2079−2088.
(214) Li, S.-S.; Zhang, M.; Wang, J.-H.; Yang, F.; Kang, B.; Xu, J.-J.; Chen, H.-Y. Monitoring the Changes of pH in Lysosomes during Autophagy and Apoptosis by Plasmon Enhanced Raman Imaging. *Anal. Chem.* **2019**, *91*, 8398−8405.
(215) Zhang, Y.; Jimenez de Aberasturi, D.; Henriksen-Lacey, M.; Langer, J.; Liz-Marzán, L. M. Live-Cell Surface-Enhanced Raman Spectroscopy Imaging of Intracellular pH: From Two Dimensions to Three Dimensions. *ACS Sens.* **2020**, *5*, 3194−3206.
(216) Karunakaran, V.; Saritha, V. N.; Ramya, A. N.; Murali, V. P.; Raghu, K. G.; Sujathan, K.; Maiti, K. K. Elucidating Raman Image-Guided Differential Recognition of Clinically Confirmed Grades of Cervical Exfoliated Cells by Dual Biomarker-Appended SERS-Tag. *Anal. Chem.* **2021**, *93*, 11140−11150.
(217) Neuschmelting, V.; Harmsen, S.; Beziere, N.; Lockau, H.; Hsu, H.-T.; Huang, R.; Razansky, D.; Ntziachristos, V.; Kircher, M. F. Dual-Modality Surface-Enhanced Resonance Raman Scattering and Multispectral Optoacoustic Tomography Nanoparticle Approach for Brain Tumor Delineation. *Small* **2018**, *14*, 1800740.
(218) da Silva, A. G. M.; Rodrigues, T. S.; Wang, J.; Camargo, P. H. C. Plasmonic Catalysis with Designer Nanoparticles. *Chem. Commun.* **2022**, *58*, 2055−2074.
(219) Ha, M.; Kim, J.-H.; You, M.; Li, Q.; Fan, C.; Nam, J.-M. Multicomponent Plasmonic Nanoparticles: From Heterostructured Nanoparticles to Colloidal Composite Nanostructures. *Chem. Rev.* **2019**, *119*, 12208−12278.
(220) Sousa-Castillo, A.; Comesaña-Hermo, M.; Rodríguez-González, B.; Pérez-Lorenzo, M.; Wang, Z.; Kong, X.-T.; Govorov, A. O.; Correa-Duarte, M. A. Boosting Hot Electron-Driven Photocatalysis through Anisotropic Plasmonic Nanoparticles with Hot Spots in Au−TiO_2 Nanoarchitectures. *J. Phys. Chem. C* **2016**, *120*, 11690−11699.
(221) Liu, B.; Jiang, Y.; Wang, Y.; Shang, S.; Ni, Y.; Zhang, N.; Cao, M.; Hu, C. Influence of Dimensionality and Crystallization on Visible-Light Hydrogen Production of Au@TiO_2 Core−Shell Photocatalysts Based on Localized Surface Plasmon Resonance. *Catal. Sci. Technol.* **2018**, *8*, 1094−1103.
(222) Kaur, G.; Tanwar, S.; Kaur, V.; Biswas, R.; Saini, S.; Haldar, K. K.; Sen, T. Interfacial Design of Gold/Silver Core−Shell Nanostars for Plasmon-Enhanced Photocatalytic Coupling of 4-Aminothiophenol. *J. Mater. Chem. C* **2021**, *9*, 15284−15294.
(223) Li, Y.; Geng, X.; Leng, W.; Vikesland, P. J.; Grove, T. Z. Gold Nanospheres and Gold Nanostars Immobilized onto Thiolated Eggshell Membranes as Highly Robust and Recyclable Catalysts. *New J. Chem.* **2017**, *41*, 9406−9413.
(224) Li, A.; Chen, Y.; Duan, W.; Wang, C.; Zhuo, K. Shape-Controlled Electrochemical Synthesis of Au Nanocrystals in Reline: Control Conditions and Electrocatalytic Oxidation of Ethylene Glycol. *RSC Adv.* **2017**, *7*, 19694−19700.
(225) Wang, L.; Wang, Y.; Schmuki, P.; Kment, S.; Zboril, R. Nanostar Morphology of Plasmonic Particles Strongly Enhances Photoelectrochemical Water Splitting of TiO2 Nanorods with Superior Incident Photon-to-Current Conversion Efficiency in Visible/near-Infrared Region. *Electrochim. Acta* **2018**, *260*, 212−220.
(226) Wang, S.-S.; Hu, W.-C.; Liu, F.-F.; Xu, Q.-Y.; Wang, C. Insights into Direct Plasmon-Activated Eletrocatalysis on Gold Nanostar via Efficient Photothermal Effect and Reduced Activation Energy. *Electrochim. Acta* **2019**, *301*, 359−365.
(227) Kumar, A.; Choudhary, P.; Kumar, K.; Kumar, A.; Krishnan, V. Plasmon Induced Hot Electron Generation in Two Dimensional Carbonaceous Nanosheets Decorated with Au Nanostars: Enhanced Photocatalytic Activity under Visible Light. *Mater. Chem. Front.* **2021**, *5*, 1448−1467.
(228) Wei, Y.; Zhang, X.; Liu, Z.; Chen, H.-S.; Yang, P. Site-Selective Modification of AgPt on Multibranched Au Nanostars for Plasmon-Enhanced Hydrogen Evolution and Methanol Oxidation Reaction in Visible to near-Infrared Region. *J. Power Sources* **2019**, *425*, 17−26.
(229) Liu, Q.-Y.; Zhong, Y.; Jiang, Z.-Z.; Chen, K.; Ma, S.; Wang, P.-F.; Wang, W.; Zhou, L.; Luoshan, M.-D.; Wang, Q.-Q. A Controlled Growth of Triangular AuCu Alloy Nanostars and High Photocatalytic Activities of AuCu@CdS Heterostars. *J. Mater. Chem. C* **2020**, *8*, 4869−4875.
(230) Zhang, Y.; Zhao, C.; Wang, X.; Sun, S.; Zhang, D.; Zhang, L.; Fang, Y.; Wang, P. Plasmon-Driven Photocatalytic Properties Based on the Surface of Gold Nanostar Particles. *Spectrochim. Acta, Part A* **2022**, *264*, 120240.
(231) de Barros, H. R.; García, I.; Kuttner, C.; Zeballos, N.; Camargo, P. H. C.; de Torresi, S. I. C.; López-Gallego, F.; Liz-Marzán, L. M. Mechanistic Insights into the Light-Driven Catalysis of an Immobilized Lipase on Plasmonic Nanomaterials. *ACS Catal.* **2021**, *11*, 414−423.

https://doi.org/10.1021/acsanm.2c02533
ACS Appl. Nano Mater. 2022, 5, 14051−14091

(232) Cui, Q.; Xia, B.; Mitzscherling, S.; Masic, A.; Li, L.; Bargheer, M.; Möhwald, H. Preparation of Gold Nanostars and Their Study in Selective Catalytic Reactions. *Colloids Surf., A* **2015**, *465*, 20−25.
(233) Zhang, H.; Li, X.; Chooi, K. S.; Jaenicke, S.; Chuah, G.-K. TiO_2 Encapsulated Au Nanostars as Catalysts for Aerobic Photo-Oxidation of Benzyl Alcohol under Visible Light. *Catal. Today* **2021**, *375*, 558−564.
(234) Ndokoye, P.; Zhao, Q.; Li, X.; Li, T.; Tade, M. O.; Wang, S. Branch Number Matters: Promoting Catalytic Reduction of 4-Nitrophenol over Gold Nanostars by Raising the Number of Branches and Coating with Mesoporous SiO_2. *J. Colloid Interface Sci.* **2016**, *477*, 1−7.
(235) Ma, T.; Liang, F. Au−Pd Nanostars with Low Pd Content: Controllable Preparation and Remarkable Performance in Catalysis. *J. Phys. Chem. C* **2020**, *124*, 7812−7822.
(236) Sánchez-Iglesias, A.; Barroso, J.; Solís, D. M.; Taboada, J. M.; Obelleiro, F.; Pavlov, V.; Chuvilin, A.; Grzelczak, M. Plasmonic Substrates Comprising Gold Nanostars Efficiently Regenerate Cofactor Molecules. *J. Mater. Chem. A* **2016**, *4*, 7045−7052.
(237) Guerrero-Lemus, R.; Vega, R.; Kim, T.; Kimm, A.; Shephard, L. E. Bifacial Solar Photovoltaics − A Technology Review. *Renewable Sustainable Energy Rev.* **2016**, *60*, 1533−1549.
(238) Green, M. A.; Ho-Baillie, A. Perovskite Solar Cells: The Birth of a New Era in Photovoltaics. *ACS Energy Lett.* **2017**, *2*, 822−830.
(239) Jang, Y. H.; Jang, Y. J.; Kim, S.; Quan, L. N.; Chung, K.; Kim, D. H. Plasmonic Solar Cells: From Rational Design to Mechanism Overview. *Chem. Rev.* **2016**, *116*, 14982−15034.
(240) Fan, L.; Wang, P.; Wang, M.; Lü, W.; Wang, F.; Liu, H.; Yang, J.; Yang, L. Exploring Low-Temperature Processed Multifunctional HEPES-Au NSs-Modified SnO_2 for Efficient Planar Perovskite Solar Cells. *Chem. Eng. J.* **2022**, *427*, 131832.
(241) Zhu, S.-Q.; Bian, B.; Zhu, Y.-F.; Yang, J.; Zhang, D.; Feng, L. Enhancement in Power Conversion Efficiency of GaAs Solar Cells by Utilizing Gold Nanostar Film for Light-Trapping. *Front. Chem.* **2019**, *7*, 137.
(242) Ginting, R. T.; Kaur, S.; Lim, D.-K.; Kim, J.-M.; Lee, J. H.; Lee, S. H.; Kang, J.-W. Plasmonic Effect of Gold Nanostars in Highly Efficient Organic and Perovskite Solar Cells. *ACS Appl. Mater. Interfaces* **2017**, *9*, 36111−36118.
(243) Ren, X.; Cheng, J.; Zhang, S.; Li, X.; Rao, T.; Huo, L.; Hou, J.; Choy, W. C. H. High Efficiency Organic Solar Cells Achieved by the Simultaneous Plasmon-Optical and Plasmon-Electrical Effects from Plasmonic Asymmetric Modes of Gold Nanostars. *Small* **2016**, *12*, 5200−5207.
(244) Batmunkh, M.; Macdonald, T. J.; Peveler, W. J.; Bati, A. S. R.; Carmalt, C. J.; Parkin, I. P.; Shapter, J. G. Plasmonic Gold Nanostars Incorporated into High-Efficiency Perovskite Solar Cells. *ChemSusChem* **2017**, *10*, 3750−3753.
(245) Kozanoglu, D.; Apaydin, D. H.; Cirpan, A.; Esenturk, E. N. Power Conversion Efficiency Enhancement of Organic Solar Cells by Addition of Gold Nanostars, Nanorods, and Nanospheres. *Org. Electron.* **2013**, *14*, 1720−1727.
(246) Elbohy, H.; Kim, M. R.; Dubey, A.; Reza, K. M.; Ma, D.; Zai, J.; Qian, X.; Qiao, Q. Incorporation of Plasmonic Au Nanostars into Photoanodes for High Efficiency Dye-Sensitized Solar Cells. *J. Mater. Chem. A* **2016**, *4*, 545−551.
(247) Gonfa, B. A.; Kim, M. R.; Zheng, P.; Cushing, S.; Qiao, Q.; Wu, N.; El Khakani, M. A.; Ma, D. Investigation of the Plasmonic Effect in Air-Processed PbS/CdS Core−Shell Quantum Dot Based Solar Cells. *J. Mater. Chem. A* **2016**, *4*, 13071−13080.
(248) Notarianni, M.; Vernon, K.; Chou, A.; Aljada, M.; Liu, J.; Motta, N. Plasmonic Effect of Gold Nanoparticles in Organic Solar Cells. *Sol. Energy* **2014**, *106*, 23−37.
(249) Wang, J.; Lee, Y.-J.; Chadha, A. S.; Yi, J.; Jespersen, M. L.; Kelley, J. J.; Nguyen, H. M.; Nimmo, M.; Malko, A. V.; Vaia, R. A.; Zhou, W.; Hsu, J. W. P. Effect of Plasmonic Au Nanoparticles on Inverted Organic Solar Cell Performance. *J. Phys. Chem. C* **2013**, *117*, 85−91.
(250) Lee, D. S.; Kim, W.; Cha, B. G.; Kwon, J.; Kim, S. J.; Kim, M.; Kim, J.; Wang, D. H.; Park, J. H. Self-Position of Au NPs in Perovskite Solar Cells: Optical and Electrical Contribution. *ACS Appl. Mater. Interfaces* **2016**, *8*, 449−454.
(251) Miroshnikov, Y.; Yang, J.; Shokhen, V.; Alesker, M.; Gershinsky, G.; Kraytsberg, A.; Ein-Eli, Y.; Zitoun, D. Operando Micro-Raman Study Revealing Enhanced Connectivity of Plasmonic Metals Decorated Silicon Anodes for Lithium-Ion Batteries. *ACS Appl. Energy Mater.* **2018**, *1*, 1096−1105.
(252) Liu, T.; Zhang, Y.; Li, C.-H.; Marquez, M. D.; Tran, H.-V.; Robles Hernández, F. C.; Yao, Y.; Lee, T. R. Semihollow Core−Shell Nanoparticles with Porous SiO_2 Shells Encapsulating Elemental Sulfur for Lithium−Sulfur Batteries. *ACS Appl. Mater. Interfaces* **2020**, *12*, 47368−47376.
(253) Han, Y.; Yang, X.; Liu, Y.; Ai, Q.; Liu, S.; Sun, C.; Liang, F. Supramolecular Controlled Cargo Release via Near Infrared Tunable Cucurbit[7]Uril-Gold Nanostars. *Sci. Rep.* **2016**, *6*, 22239.
(254) Martínez, E. D.; Urbano, R. R.; Rettori, C. Thermoplasmonic Maskless Lithography on Upconverting Nanocomposites Assisted by Gold Nanostars. *ACS Appl. Nano Mater.* **2019**, *2*, 6889−6897.
(255) Munkhbat, B.; Pöhl, H.; Denk, P.; Klar, T. A.; Scharber, M. C.; Hrelescu, C. Performance Boost of Organic Light-Emitting Diodes with Plasmonic Nanostars. *Adv. Optical Mater.* **2016**, *4*, 772−781.
(256) Munkhbat, B.; Ziegler, J.; Pöhl, H.; Wörister, C.; Sivun, D.; Scharber, M. C.; Klar, T. A.; Hrelescu, C. Hybrid Multilayered Plasmonic Nanostars for Coherent Random Lasing. *J. Phys. Chem. C* **2016**, *120*, 23707−23715.
(257) Jahn, M.; Patze, S.; Hidi, I. J.; Knipper, R.; Radu, A. I.; Mühlig, A.; Yüksel, S.; Peksa, V.; Weber, K.; Mayerhöfer, T.; Cialla-May, D.; Popp, J. Plasmonic Nanostructures for Surface Enhanced Spectroscopic Methods. *Analyst* **2016**, *141*, 756−793.
(258) Lee, J. W.; Jung, H.; Cho, H. H.; Lee, J. H.; Nam, Y. Gold Nanostar-Mediated Neural Activity Control Using Plasmonic Photothermal Effects. *Biomaterials* **2018**, *153*, 59−69.

Recommended by ACS

Molecular Plasmonics with Metamaterials
Pan Wang, Anatoly V. Zayats, *et al.*
OCTOBER 04, 2022
CHEMICAL REVIEWS
READ

Do We Really Need Quantum Mechanics to Describe Plasmonic Properties of Metal Nanostructures?
Tommaso Giovannini, Chiara Cappelli, *et al.*
SEPTEMBER 01, 2022
ACS PHOTONICS
READ

Plasmonic Core–Shell Materials: Synthesis, Spectroscopic Characterization, and Photocatalytic Applications
Hong-Jia Wang, Jian-Feng Li, *et al.*
JANUARY 20, 2022
ACCOUNTS OF MATERIALS RESEARCH
READ

Intermolecular Forces Dictate Vibrational Energy Transfer in Plasmonic–Molecule Systems
Ziwei Yu and Renee R. Frontiera
DECEMBER 22, 2021
ACS NANO
READ

Get More Suggestions >